Research Square

Preprints are preliminary reports that have not undergone peer review.
They should not be considered conclusive, used to inform clinical practice,
or referenced by the media as validated information.

The autophagic/lysosomal enhancer GHF201 ameliorates pathological features in patient-derived fibroblasts and a mouse model of Pompe disease

Uri Sprecher
Tel Aviv University
Manjeet Gupta
Hebrew University of Jerusalem
Shireen Sarji
Tel Aviv University
Noam Muchtar
Tel Aviv University
Kumudesh Mishra
Hadassah Medical Center
Pradeep Kumar
Hebrew University of Jerusalem
Sahar Sweetat
Hebrew University of Jerusalem
Dunya Edilbi
Tel Aviv University
Or Shefer
Tel Aviv University
Ori Shalev
Hebrew University of Jerusalem
Alexandra Eliassaf
Hebrew University of Jerusalem
Anna Morshina
Hebrew University of Jerusalem
Sharon Garti
Lyotropic Delivery Systems
Nissim Garti
Lyotropic Delivery Systems
Galia Blum
Hebrew University of Jerusalem
Hannah Mandel

Rambam Health Care Campus
Galit Tal
Rambam Health Care Campus
Hanna Rosenmann
Hadassah Medical Center
Miguel Weil
Tel Aviv University
Or Kakhlon
ork@hadassah.org.il

Hadassah Medical Center

Research Article

Keywords: Pompe Disease, GHF201, lysosomes, autophagy, mitochondria, metabolomics

Posted Date: November 24th, 2026

DOI: https://doi.org/10.21203/rs.3.rs-11732166/v1

License: This work is licensed under a Creative Commons Attribution 4.0 International License.
Read Full License

Additional Declarations: Competing interest reported. OK and MW also serve as consultants to GHF, Golden Heart Flower Ltd. All IP rights in the invention of GHF-201 described in this manuscript were licensed to GHF. OK and MW are also the holders of patent US11891381B2 “Compounds for the treatment of glycogen storage disorders” which includes GHF-201.

The autophagic/lysosomal enhancer GHF201 ameliorates pathological features in patient-derived fibroblasts and a mouse model of Pompe disease

Uri Sprecher[1 *], Manjeet Gupta[2,3 *§], Shireen Sarji[1], Noam Muchtar[1], Kumudesh Mishra[2,3], Pradeep Kumar[2,3], Sahar Sweetat[2,3], Dunya Edilbi[1‡], Or Shefer[1], Ori Shalev[4], Alexandra Eliassaf[4], Anna Morshina[4], Sharon Garti[5], Nissim Garti[5], Galia Blum[6], Hanna Mandel[7,8], Galit Tal[8,9], Hanna Rosenmann[2,3], Miguel Weil[1,9 §], Or Kakhlon[2,3 §]

[1]The Shmunis School of Biomedicine and Cancer Research, The George S. Wise Faculty for Life Sciences, Tel Aviv University, 6997801 Tel Aviv, Israel

[2]Department of Neurology, The Agnes Ginges Center for Human Neurogenetics, Hadassah Hebrew University Medical Center, Jerusalem 9112001, Israel

[3]Faculty of Medicine, Hebrew University of Jerusalem, Ein Kerem, Jerusalem 9112102, Israel

[4]The Metabolic Profiling Unit, Core Research Facility, Faculty of Medicine, The Hebrew University of Jerusalem, Jerusalem 9112102, Israel

[5]Lyotropic Delivery Systems Ltd., Hi-Tech Park, Row 5(1), Edmond J. Safra Campus, Jerusalem 9139002, Israel

[6]School of Pharmacy, Faculty of Medicine, The Hebrew University of Jerusalem, Jerusalem 9112102, Israel

[7]Metabolic Unit, Ruth Rappaport Children's Hospital, Rambam Health Care Campus, PO Box 9602, Haifa, 3109601, Israel

[8]Rappaport Faculty of Medicine, Technion-Israel Institute of Technology, Haifa, 3109601, Israel

[9]Sagol School of Neurosciences, Tel Aviv University, 6997801 Tel Aviv, Israel

*Equal contribution

[§]Corresponding author

[‡]Current address: Department of Molecular Genetics, Weizmann Institute of Science, Rehovot 7610001, Israel

Abstract

Pompe Disease (PD) is a neuromuscular lysosomal storage disorder (LSD) caused by deficiency of lysosomal acid α-glucosidase (GAA), which hydrolyzes glycogen to glucose in the lysosome. PD pathology is caused by lysosomal dysfunction leading to autophagic and mitochondrial defects and apoptosis. Here we tested in the *Gaa*$^{-/-}$ PD mouse model whether the lysosomal activator GHF201 and its delivery by an innovative and well-established nanodroplet formulation can ameliorate PD pathology. In PD human fibroblasts, GHF201 restricted glycogen accumulation and ameliorated lysosomal, autophagic, and mitochondrial dysfunction. All these ill-phenotypes were partially normalized by GHF201. Counter-intuitively, infantile-onset PD fibroblasts manifested decreased reactive oxygen species production, possibly attributed to the increase in mitochondrial mass and consequent dilution of fuel acceptors observed in these fibroblasts. GHF-201 was demonstrated to be safe in PD mouse models and its pharmacokinetic profile reveals biodistribution to brain and muscle. In addition, we show that GHF-201 improved the deficient motor phenotype of the *Gaa*$^{-/-}$ PD mouse model. The bioenergetic function and autophagic activity of muscle fibers, myotubes and pancreatic islets isolated from Gaa$^{-/-}$ mice were also improved by GHF201, which also attenuated ROS production in these myofibers and myotubes. Interestingly, GHF-201 treatment improved basal insulin secretion from Gaa$^{-/-}$ pancreatic islands, while the GYS inhibitor guaiacol improved only glucose-stimulated insulin secretion, aligning with respiratory (OxPhos-dependent) *vs* glycolytic metabolic activation by GHF-201 and guaiacol, respectively. Taken together, our work strongly suggests that GHF-201 has a potential value as a PD therapeutic.

Key Words

Pompe Disease, GHF201, lysosomes, autophagy, mitochondria, metabolomics

Introduction

Storage diseases are a group of more than 70 rare genetic disorders caused by overaccumulation of substances inside biological tissues. The body's failure to degrade or exploit these substances for energy production often leads to the accumulation of toxic, commonly insoluble, aggregates. Thus, the etiopathology of storage disorders is twofold: limited capacity to turn over the aggregates into fuel, and their toxicity, especially enhanced when they form insoluble inclusion bodies, sometimes also referred to as "wasteosomes", which are pathogenic when not adequately cleared[1-5]. Lysosomal storage disorders (LSDs) are typical storage disorders. An eminent LSD is the neuromuscular disorder Pompe Disease (PD), or glycogen storage disease type II (GSDII, prevalence of 1 in 18,711 live births)[6], which is both a GSD and an LSD. PD is caused by deficiency in GAA, a lysosomal enzyme which hydrolyzes glycogen to glucose in the lysosome. This lysosomal glycogen surcharge leads to distended and dysfunctional lysosomes. PD pathology is thus caused by lysosomal dysfunction leading to autophagic and mitochondrial defects and apoptosis[7, 8]. PD manifestation ranges from rapidly fatal infantile-onset myopathy and hypertrophic cardiomyopathy (IOPD) to a less severe late onset skeletal muscle myopathy in children and adults (LOPD). Current treatments for PD are based on enzyme replacement therapy (ERT), substrate reduction therapy (SRT) and adeno-associated viral (AAV) gene therapy (GT). First ERT (Aglucosidase alpha, Sanofi Genzyme) based on IV administration of recombinant human GAA (rhGAA) was approved in 2006. Next generation ERTs mainly include: 1. Neo-GAA (Avaglucosidase-alpha, Sanofi Genzyme) and the AT-GAA rhGAA/small molecule chaperone combination (Amicus), both with higher cation independent Mannose-6-phosphate receptor (CI-MPR) affinity; 2. VAL-1221, a fusion of rhGAA with the 3E10 antibody (Fab) allowing rhGAA internalization by the ENT2 transporter. While next generation ERT do have promise, for instance leading to muscular and pulmonary improvements (NCT03911505), some of the clinical trials using next generation ERTs were discontinued (e.g., NCT02898753). In addition, an important concern is cross-reactivity to immunologic material (CRIM), especially in naïve IOPD patients. This complication can be partially resolved by immune tolerance induction (ITI) using the immunosuppressors rituximab, IVIG and methotrexate. However, the risk for infection and cancer in the immunosuppressant-sensitive CRIM-

negative patients is a major concern for ITI co-therapy in PD (e.g., [9]). Another disadvantage of ERT in PD is that rhGAA cannot cross the BBB and target motor neurons which contribute to the pathology[10]. Moreover, lysosomal delivery of the enzyme in ERT is disrupted due to the autophagic buildup[11, 12]. GT in PD was mainly developed to overcome these obstacles, providing a constant supply of GAA. Most GT approaches are based on supplementation of GAA in AAVs of different serotypes. While encouraging results led to several ongoing clinical trials in LOPD patients, there are still some unresolved pitfalls: 1. Muscle transduction of AAV-GAA. While myocytes as quiescent cells are best suited for long-term AAV transgene expression, the muscle fiber degeneration and remodeling characteristic of PD mean that fibers initially transduced with AAV-GAA could waste away. Moreover, a significant part of GAA is uptaken by muscle via CI-MPR-mediated endocytosis. Type II glycolytic muscle fibers have a meager expression of CI-MPR, which poses a serious barrier for the introduction of GAA into muscle. This challenge has been addressed by co-administration of CI-MPR activating β2-agonists, however, only heart glycogen was reduced by this co-therapy[13]. 2. A major obstacle in PD is the multi-organ nature of the disease, requiring GAA delivery to several organs (*e.g.*, diaphragm, heart). This challenge was addressed by using the liver as a depot for systemically-delivered AAV-GAA GT[14]. However, if AAV-GAA is administered to the liver at infancy, to treat IOPD, episomal AAV-GAA vector genomes are diluted due to the fast rate of liver cell division typical of infants[15]. This GAA dilution significantly reduces the efficacy of liver-depot GT in IOPD and requires AAV re-dosing with ensuing complications, as in ERT, related to immune response against the AAV capsid. Even if AAV-GAA is integrated to the hepatocytes (or other cells) genomes, which happens in less than 10% of transduction events, this integration bears the risk of insertional mutagenesis and tumor formation[16]. The possible solution of integration into human genomic safe harbor sites is still being developed[17, 18]. Lastly, SRT based on small molecule inhibitors of glycogen synthase[19-21], such as Maze Therapeutics' MZE001, has passed first-in-human safety tests[22], while confirmation of clinical efficacy in phase 2 trials is still imminent.

Given the insufficiency of all the existing treatment paradigms, in this study we opted for testing a novel approach. GHF201 is our newly-discovered lysosomal activator[23]. The molecular target of GHF201 is

LAMP-1[23] and its mechanism of action is activation of autolysosomal degradation of glycogen and other substrates. Several lines of evidence and supporting observations underpin the role of GHF201 as an autolysosomal activator mediating its effect through interaction with LAMP-1. GHF-201 binds to the N-terminal domain of LAMP-1 and thus interferes with LAMP-1/LAMP-1 and LAMP-1/LAMP-2 interaction[23]. This effect is equivalent to LAMP-1 knockdown in the sense that it dilutes LAMP-1 on the lysosomal membrane. Dilution or knockdown of LAMP-1 has been demonstrated to enhance lysosomal function and autophagic flux in several works highlighting different aspects of this effect: LAMP-1 knockdown increased lysosomal protein degradation[24], reversed accumulation of the unesterified cholesterol stain filipin, which is cleared by autophagy[25], and led to lysosomal acidification in *D. melanogaster* fat body[26], as it did in our hands in fibroblasts[23]. Several mechanisms associate LAMP-1 inhibition with autophagy enhancement: LAMP-1 inhibits the lysosomal proton exporter TMEM175 and therefore LAMP-1 inhibition leads to lysosomal acidification[27]. Moreover, LAMP-1 also interacts with v-ATPase[28] and LAMP-1 inhibition acidifies lysosomes also on a TMEM175-deficient background[26], suggesting that LAMP-1 can also influence lysosomal pH through direct v-ATPase modulation. Lastly, LAMP-1 inhibition can enhance lysosomal activity by the documented compensatory increase in LAMP-2 in the lysosomal membrane (*e.g.*, [25]). The increased LAMP2 can enhances fusion between lysosomes and autophagosomes (generating autolysosomes) by interacting with GORASP2 on the cytoplasmic aspect of the autophagosome outer membrane[29] thus enhancing autophagic flux. The lysosomal (LAMP-1) targeting of GHF201 predicts that it should be beneficial for treating the LSD PD. Moreover, GHF201 has a proven efficacy in glycogen storage diseases types IV (adult form, Adult Polyglucosan Body Disease)[23], III[30] and Ia[31]. In terms of clinical relevance, GHF-201 was approved for an urgent compassionate use program in 4 APBD patients totaling over 11 patient's years. GHF partnered with Lyotropic Delivery System (LDS) to formulate GHF-201 in a highly-bioavailable non-aqueous oral solution, administered twice daily. The program, led by Prof. Alexander Lossos and his team at Hadassah University Hospital–Ein Kerem, Jerusalem, has shown promising clinical improvement for GHF-201 with no observed negative safety signals (https://www.accessdata.fda.gov/scripts/opdlisting/oopd/detailedIndex.cfm?cfgridkey=953523;

https://ec.europa.eu/health/documents/community-register/html/o3023.htm). In addition, a clinical trial (2024-519813-74-00) and a Phase 2/3 Adaptive Design Study have been initiated[32]. We show here that GHF201 partially restored the aberrant cellular phenotype in both IOPD and LOPD patient-derived skin fibroblasts. A tailored safe nanoformulation of GHF201, widely distributed in various mouse tissues, was capable of constraining glycogen overburden in skeletal muscle of the PD modeling, GAA-knocked out *Gaa*$^{-/-}$ mouse strain. Moreover, our ex vivo analysis showed that GHF201 corrected the compromised bioenergetic and autophagic capacities and the increased oxidative stress in *Gaa*$^{-/-}$-derived myotubes. In *Gaa*$^{-/-}$ pancreatic islets, on the other hand, GHF201 corrected the bioenergetic profile and also stimulated basal insulin secretion. In addition, GHF201 expedited the impeded muscle differentiation in *Gaa*$^{-/-}$ mice, countering muscle atrophy. In summary, we present here comprehensive preclinical evidence supporting the application of GHF201 as a novel therapeutic modality for PD.

Results

PD fibroblast present a cellular disease phenotype correlated with GAA activity levels

To phenotype PD patients primary skin fibroblasts, we applied image-based high-content analysis (HCA) in several independent experiments: Fibroblasts from 9 PD (6 infantile onset PD (IOPD) and 3 late onset PD (LOPD)) patients and healthy control (HC, age and gender matched) individuals were incubated for 24 h and 48 h in cell culture media under serum and glucose starvation, or under 48 h starvation followed by full medium (including serum and glucose) restoration for the last 24 h of incubation (72 h). These different culture conditions were applied to induce metabolic stress in the cells by sugar deprivation (24 and 48 h) and by glycogen burden, which was induced by compensatory up-modulation of glucose uptake following the 48h starvation (72 h) as shown in similar HCA phenotyping experiments in APBD[23] and GSD1a patients' fibroblasts[33]. At each experimental time point, the cells were simultaneously co-stained with fluorescent probes for nuclei (Hoechst 33442), cytoplasm (Calcein-AM-green), lysosomes (Lysotracker-deep red) and active mitochondria (TMRE-red). Live images were then taken using the Operetta G1 microscopy system and quantitatively analyzed using the Harmony image analysis software to generate features representing wells of imaged samples. Downstream processing was performed in Python (see Methods),

the output from this analysis resulted in three types of features for each labeled organelle; area features representing organelle morphology, intensity features representing signal strength and texture features which combine the intensity and area of the signal from each organelle. The biological relevance of these features is dependent on each organelle dye properties and can be further investigated with other biological assays. As PD is a lysosomal storage disorder with known metabolic aberrations, we hypothesized TMRE and Lysotracker features would stand out in wells with PD cells as compared to wells with HC cells.

Representative images from each labeled organelle and for each tested group are shown in Fig 1A. To test if the data can discriminate between wellsof PD and HC samples in different tested time conditions, principal component analysis (PCA) was applied on grouped data for each group in each tested time condition (Fig. 1B). The results indicate a clear separation between HC and PD groups (PC1) and between the different tested culture conditions (PC2). Feature importance bar plots are shown in Fig. S1A and show that PC1 group separation is attributed to lysosomal and mitochondrial features, while PC2 separation was based on all organelles. Next, we used a heatmap visualization (Fig. 1C) to deduce the most prominent culture condition for HC and PD separation. Our conclusion is that the 24h starvation condition was the most effective in generating group separation between HC and PD cells. Remarkably, compared to LOPD, IOPD showed distinctively larger feature differences from HC, across all features. In addition, we noticed that the viability of PD cells is compromised following 48 h and 72 h starvation conditions (Fig. S1B) which further supported the choice of the 24 h starvation condition in the following experiments. All the features from the 24h condition are shown in Fig S1C and highlight the robust cellular phenotype found in wells of IOPD and LOPD cells under this culture condition. The reproducibility and validity of these and other HCA results were tested by a statistical bootstrap mediated method to compute a 95% effect size bootstrap confidence interval(BCI) for each group (see Methods), which is represented in the lower panel of the plots. The BCI plots demonstrate the precision of the mean difference measured between each group and HC, manifested by the gap between BCI boundary values of each group. To define the HCA phenotype at the patient level we also grouped all wells for each patient and plotted all features. These results supported

the trends shown at the well level (Fig S2A). Next, to discover the main features of all labeled organelles that contribute to the phenotypic group separation, we performed linear discriminant analysis (LDA) on each of the sample wells used in the experiment in all three culture conditions (Fig. 1D). The LDA algorithm shows a clear separation between wells of HC and PD samples along LD1 and, within the PD group, between wells of IOPD and LOPD patient fibroblasts along both LD1 and LD2. Fig. 1E presents bar plots indicating the features most contributing for group separation between HC, IOPD and LOPD using LDA on LD1 and LD2. As expected, mitochondrial and lysosomal features dominate this analysis, highlighting these organelles' role in the diseased phenotype identified in both IOPD and LOPD cells. Following these broad phenotypic analyses, we decided to test and establish the correlation of image-based HCA phenotypic differences between IOPD and LOPD and their respective GAA enzymatic activities, along with their clinical diagnostics. To that end, we tested GAA activity levels in 6 IOPD and 3 LOPD patients using a GAA enzymatic activity kit. As shown in Fig. 1F, the differences in GAA activity match the differences in cellular phenotypes observed between the IOPD, LOPD and HC samples. This finding is further supported by a patient-based correlation analysis performed on HCA and GAA activity data from each patient sample, as shown in a correlation plot in Fig S2B. These results clearly demonstrate how the image-based severity phenotype in PD cells matches their GAA activity levels and clinical description, supporting the relevance of the phenotype differences we discovered between the PD subgroups.

PD fibroblasts manifest lysosomal pathology partially reversible by GHF201 with respect to PD sample severity

Next, we performed additional experiments to expand the focus on lysosomal-specific disease mechanisms for PD fibroblasts. As PD is a lysosomal disorder, we performed experiments to better describe the lysosomal phenotype in PD patient-derived fibroblasts by using GHF-201, our glycogen reducing and LAMP1 targeting compound which enhances autophagic flux and lysosomal function[23]. First, we confirmed that GHF201 indeed reduced glycogen levels in wells of PD fibroblasts as shown by the periodic acid Schiff's reagent (PAS) assay (Fig. 2A). Furthermore, we assessed the effect of GHF201 on autophagic flux by quantifying the susceptibility of lipidation of the autophagy marker LC3 to vinblastine, a known

autophagosome/lysosome fusion inhibitor.

We compared the effect of GHF201 on autophagic flux by western blot (WB) analysis. We found that PD cells treated with GHF201 show higher vinblastine-dependent increase in the LC3ii/LC3i ratio (*i.e.*, autophagic halt) indicating higher autophagic flux (Fig. 2B). Notably, under basal conditions (in the absence of vinblastine), GHF201 decreased the steady-state levels of both LC3-I and LC3-II. This concurrent reduction is consistent with accelerated baseline autophagic turnover, where rapid conversion of LC3-I and subsequent lysosomal clearance of LC3-II deplete the steady-state pools. Interestingly, this baseline depletion was more pronounced in PD fibroblasts than in HC fibroblasts, reflecting the successful clearance of the characteristic autophagic bottleneck associated with GAA deficiency. A similar GHF201-mediated increase in autophagic flux was also observed in GSDIV[23] and GSDIa[31] fibroblasts. Next, we implemented a lysosomal activity pipeline using robust imaging techniques. For this purpose, skin fibroblasts from six different IOPD, three different LOPD and five different HC subjects were grown to full confluency and then seeded in 96 well plates in parallel for the different experiments, following 24 h starvation as described above. Wells with cells from each group were either untreated, or treated with GHF201. We first decided to confirm that lysosomal activity is compromised in wells of PD fibroblasts, as compared to HC, and corrected by GHF201. To that end we first measured lysosome area, whose increase is known as a prominent feature in PD, using lysotracker deep red at a 40x magnification which offers higher resolution for organelle area measurements (Fig. 2C). The lysosomal membrane disrupting agent L-leucyl-L-leucine methyl ester (LLOME[34]), known to compromise lysosomal function and promote lysosomal rupture, served as a negative control in these experiments and indeed resulted in lysosomal rapture in all tested groups. As expected, both wells of IOPD and LOPD cells presented with a higher lysosomal area than wells of HC cells, suggesting lysosomal distension. This phenotype was significantly reversed by GHF201, indicating that it interacts with lysosomes and enhances lysosomal catabolism in these cells. Next, we assessed lysosomal function using the lysosomal ratiometric pH sensor acridine orange (AO) which changes fluorescence from green to red as organellar pH declines[35], again we used LLOME as a negative control. Our AO results (Fig. 3A) show that, expectedly, lysosomes were more

alkaline in wells of IOPD cells and LOPD cells as compared to wells of HC cells. Interestingly, GHF201 treatment acidified lysosomes in wells of IOPD and to a lesser extent in wells of LOPD, as expected LLOME resulted in higher green to red ratio in wells of all tested groups. To directly assess lysosomal function, we measured the levels of endogenous active lysosomal cathepsin using the activity-based probe GB123[36], which labels active cathepsins in lysosomes and therefore reports lysosomal activity (Fig. 3B). Our GB123 results demonstrated reduced lysosomal activity in wells of PD cells as compared to those of HC cells and partial normalization of lysosomal cathepsin activity by GHF201. Our GB123 results align with the AO results, demonstrating reduced lysosomal activity in wells of PD as compared to those of HC cells and partial normalization of lysosomal activity by GHF201. To investigate the effect of GHF201 on the lysosomal function in PD cells in a more detailed manner, we measured autophagy in wells of PD cells and HC cells by immunofluorescence analysis of p62 levels. The results show that wells of HC cells have lower levels of p62 than those of IOPD and LOPD cells, while GHF201 treatment reduced the levels of this marker indicating increased autophagic activity (Fig. 3C and representative images in Fig. S3). Together with this, we performed immunofluorescence analysis of Pink1, a mitophagic turnover marker of dysfunctional mitochondria[37], TFEB, a master transcriptional regulator of autophagy and lysosomal biogenesis[38] and the lysosomal marker LAMP1 to investigate further the autophagic block in wells of PD fibroblasts in the presence or absence of GHF201. Fig. 3C and representative images in Fig. S3 show Pink1, TFEB and LAMP1 results from these immunofluorescence experiments. The lower Pink1 levels observed in wells of IOPD and LOPD patients' cells suggest a defective mitophagic turnover of dysfunctional mitochondria, which in turn can be alleviated by GHF201 treatment. Interestingly, low levels of TFEB in wells of PD fibroblasts also support the existence of autophagic stress in these cells. Moreover, LAMP1 whose abnormal accumulation in the lysosome suggests lysosomal distention and is considered a biomarker of PD[39], is shown to be significantly increased in wells of IOPD patients' fibroblasts as compared to those of HC and LOPD cells. This effect is considerably reduced by GHF 201 treatment. Interestingly the autophagic and lysosomal dysfunction found in wells of PD fibroblasts is correlative to the disease severity in IOPD and LOPD patients, being higher in IOPD as compared to LOPD cells. Moreover, a proportional corrective effect of GHF201

according to the PD type is observed, with IOPD wells being more responsive to GHF-201 than LOPD wells.

PD fibroblasts manifest mitochondrial defective features that are partially reversible by GHF201 with respect to PD severity

To investigate the mitochondrial phenotype in PD cells we applied a mitochondrial activity pipeline developed in our laboratory. These experiments included the Seahorse XF assay, Tetramethylrhodamine Ethyl Ester (TMRE) imaging, mitochondrial reactive oxygen species (ROS) production using MitoSox red, mitochondrial DNA quantification and parallel WB analysis of mitochondrial markers for electron transport chain (ETC) complexes. For this purpose, we cultured all six IOPD, three LOPD and five HC fibroblasts samples to full confluency and seeded all of them in parallel in their respective culture plates for the multiple analyses of this pipeline with or without GHF-201 treatment. In addition, positive control (PC, mTOR over-activated AV-9915 fibroblasts(GFER), with enhanced OxPhos activity[40, 41] & HC sample supplemented with galactose enriched media) and negative control (NC, OxPhos depleted MNGIE fibroblasts[42, 43] and HC sample supplemented with mitoQ)) for the mitochondrial Seahorse XF activity assay were used as comparators (see Methods). Results from these experiments are shown in Fig. 4 and Fig. 5.

First, cells were seeded in Seahorse XF plates following 24 h starvation conditions as described above. The Seahorse XF assay revealed significant differences in oxygen consumption rate (OCR) profile and derived parameters between wells of IOPD, LOPD and HC samples. As expected, wells of MNGIE fibroblasts showed lower levels in all OCR derived parameters while wells of GFER cells showed a modest increase in most parameters comparted to wells of HC cells. Basal and maximal OCR were significantly reduced in wells of IOPD and LOPD, compared to those of HC cells. These effects were more pronounced in wells of IOPD cells. This decrease in basal OCR, which was more pronounced than the decrease in proton leak, explains the decrease in mitochondrial ATP production (basal OCR – OCR after oligomycin) in wells of IOPD and LOPD cells. Interestingly, GHF201 partially restored the PD-compromised OxPhos capacity, increasing basal OCR and consequently proton leak in wells of IOPD and LOPD, the effect being more pronounced in IOPD. Modular kinetics[44, 45] causally correlates respiration with mitochondrial membrane potential. To further

explore the mitochondrial phenotype in wells of PD cells by modular kinetics, we supplemented our bioenergetics results with TMRE-based mitochondrial membrane potential (MMP) quantification using 40x magnification for higher resolution (Fig. 5A). wells of HC supplemented with galactose enriched media showed similar TMRE levels to untreated HC while MitoQ strongly reduced TMRE staining compared to HC. As expected, MNGIE fibroblasts showed lower levels in all OCR derived parameters while wells of GFER cells showed a modest increase in most parameters comparted to those of HC cells.

TMRE staining in wells of IOPD and in LOPD was lower as compared to those of HC cells indicating that wells of PD cells share a distinctive mitochondrial depolarization phenotype. Moreover, GHF201 partially normalized MMP in wells of both IOPD and LOPD, probably due to increased mitochondrial fueling via autophagic catabolism improved by mitophagic clearance of dysfunctional mitochondria and concomitantly enrichment for functional mitochondria.

According to modular kinetics, a parallel decrease in OCR and MMP means that electron transport as an OCR driver is blunted, while if OCR increases as MMP is depolarized, this is usually attributed to MMP dissipation by an uncoupler enabling faster OCR due to the decreased proton gradient. Since both OCR and MMP were decreased by the PD phenotype, the latter blunted electron transport through the ETC (as opposed to an uncoupler which dissipates MMP allowing faster OCR). This impeded electron transport is expected to increase mitochondrial ROS production because stalled electrons can react with oxygen, generating superoxide radicals. Therefore, we determined mitochondrial ROS production in wells of HC and PD cells using MitoSox, a fluorescent probe that detects superoxide radical produced by mitochondrial respiration. Surprisingly, the results from this experiment showed that mitochondrial ROS production in wells of PD cells, regardless of treatment, was actually *lower* than in those of HC cells, against the modular kinetic expectation from an ETC inhibitor (Fig. 5B).

To better understand this observation, we decided to integrate our OCR, MMP and mitochondrial ROS production results with a mitochondrial mass analysis based on quantification of mitochondrial DNA (mtDNA) by real time PCR (RT-PCR), which is an inclusive proxy for mitochondrial mass, and corroborated by WB analysis. Using RT-PCR, we compared nuclear DNA normalized mtDNA content among the different

groups (Fig. 5C and Fig. S4A). These results showed an increase in mitochondrial content in IOPD and LOPD cells as compared to HC, also observed in both negative control (from MNGIE fibroblasts) and positive control (from AV-9915 fibroblasts (GFER)) mitochondria. The mtDNA results were corroborated by WB analysis of protein expression of the core subunits of each ETC complex (except c. IV), as shown in Fig. S4B. The results show that the levels of core subunits of ETC complexes II (*SDHB*), III (*UQCRC2*), and V (*ATP5A1*) were increased in PD cells (core subunit of complex IV (*MTCO1*) was not different), regardless of the treatment, as compared to HC cells. This effect is also more pronounced in IOPD, as compared to LOPD cells. Interestingly, GHF201 treatment increased mitochondrial content in accordance with its mediated enhancement of mitophagy[31] (as shown for PINK1 in Fig. 3C), which enriches for functional and intact mitochondria. We conclude that the integrity of untreated PD mitochondria, especially in IOPD, is compromised causing a compensatory increase in mitochondrial mass due to turnover imbalance between mitogenesis and mitophagy. This increase might mitigate ROS production via fuel feeding into more mitochondria[46, 47]. However, the increase in mitochondrial mass produced by GHF201 is apparently not large enough to significantly mitigate mitochondrial ROS production.

The pharmacokinetic profile of GHF201 is improved by a novel tailored nanodroplet formulation

The pharmacokinetic (PK) profile of a new nanodroplet (ND) formulation of GHF201, ND-GHF201, developed by Lyotropic Delivery Systems (LDS) Ltd. for *per os* (*p.o.*) administration, was determined in several tissues and in serum derived from *Gaa*$^{-/-}$ mice using liquid chromatography tandem mass spectrometry (LC-MS/MS) as described previously by us[23]. Our results (Fig. 6A) show that following oral administration of ND-GHF201, tmax in the muscle is similar to that observed following intramuscular (IM) injection of GHF201 and is 30 min. We have to denote that the estimation of this tmax is based on the temporal resolution we routinely use in PK experiments, where the first time point is 30 min. The real tmax might have been shorter. Cmax in muscle is slightly higher using ND-GHF201 compared to intramuscular injection of non-formulated GHF201 and clearance rate from skeletal muscle (AUC = 97,467 (mg/g wet tissue)xmin, Fig. 6A, left panel) is also slower for ND-GHF201 as compared to unformulated GHF201 (AUC = 80,579 (mg/g wet tissue)xmin, Fig. 6A, right panel). These results justify the future use of

the ND-GHF201 in clinical settings for PD patients, as already done in APBD patients in a current compassionate use. Based on light transmission tests (Figs. 6Ba & 6Bb), ND-GHF201 was found to be physically and chemically stable for the clinically acceptable period of at least 3 years. The size distribution of ND-GHF201 (Fig. 6Bc) shows that ~100% of ND-GHF-201 had the expected size of the nano-droplets and the number of impurities was negligible.

GHF201 is safe and reduces glycogen surcharge in Gaa$^{-/-}$ skeletal muscle

Given the encouraging in vitro results of GHF201 and the efficacy of its tailored nanodroplet excipient we decided to further test its efficacy in vivo. As a pre-test we confirmed its in vivo safety. According to our results, change in animal weight over time was not significantly different between GHF201-treated and control groups (Fig. 6C left panel). Therefore, we conclude that GHF201 is safe in the *Gaa*$^{-/-}$ mouse strain regardless of its delivery mode (as tailored ND-formulations, or directly injected intramuscularly). Following our promising results in PD fibroblasts, showing GHF201-mediated reduction of glycogen in PD fibroblast (Fig. 2A), we also investigated the effect of GHF201 *ex vivo* in *Gaa*$^{-/-}$ mice muscle, which manifest glycogen accumulation in lysosomal puncta[48]. We determined glycogen levels in *gastrocnemius* muscle fibers collected from *Gaa*$^{-/-}$ mice (Fig. 6C middle panel (PAS), right panel (biochemical determination) & representative images in Fig. S5). Our results show that GHF-201 significantly reduced muscle glycogen levels rendering them indistinguishable from the levels in wild type littermate mice.

GHF201 can alleviate bioenergetic deficiencies ex vivo in Gaa$^{-/-}$ mice

We determined the bioenergetic profile in myoblast-differentiated myotubes. As in PD fibroblasts, basal and overall OCR profile in PD myotubes was reduced, rather than compensatory increased, suggesting lack of capacity to cope with the increased ATP demand imposed by the diseased state. With respect to the GHF201 effect, our data (Fig. 7A) show that in myotubes derived from *Gaa*$^{-/-}$ mice, GHF201 treatment increased the bioenergetic capacity, as compared to that of vehicle treated *Gaa*$^{-/-}$ mice, bringing it closer to that of wild type *Gaa*$^{+/+}$ littermates. This improvement in bioenergetic capacity is manifested as increases in the basal and maximal OCR and coupling efficacy (basal OCR-normalized drop in OCR from basal

levels following oligomycin treatment). Interestingly, in PD fibroblasts GHF201 did not increase coupling efficacy, possibly due to the relatively large drop in basal OCR to which the coupling efficacy is normalized. These results suggest that GHF-201 treatment can improve OxPhos ATP production as anticipated from a mitochondrial activator, probably through enhancement of mitophagy[31] and enrichment of functional mitochondria. IM injected GHF201 (IM-GHF201) was more efficient in increasing bioenergetic capacity than oral ND-GHF201, suggesting that for mitochondrial activation IM-GHF201 might be a better strategy for overcoming the relatively poor muscle perfusion.

Pancreatic islets play a key role in many metabolic disorders, are liable to glycogen burden related toxicity and glucotoxicity, and express all enzymes of glycogen metabolism[49]. We therefore decided to investigate whether GHF201 can also exert a therapeutic effect on pancreatic islets (Fig. 7B). As a first step, we showed that ND-GHF201 can significantly improve the overall bioenergetic profile of *Gaa*$^{-/-}$ pancreatic islets (basal and maximal OCR). Notably, in islets, ND-GHF201 manifested a better effect than IM-GHF201, possibly due to limited islet penetration of this intramuscularly injected compound. Interestingly, similar to PD fibroblasts (Fig. 4), spare respiratory capacity (difference between post-uncoupler (FCCP) and basal OCR levels, expressed as a percentage) was neither significantly reduced, nor significantly influenced by GHF-201 in both myotubes and islet cells. These results suggest compromised mitochondrial efficiency: Cells are making more mitochondria, but each individual mitochondrion is bioenergetically deficient.

GHF201 can alleviate autophagic deficiency ex vivo in Gaa$^{-/-}$ *mice*

Autophagic blockade is a known pathogenic factor in PD. Therefore, we tested the effect of GHF201 on autophagy in post-treatment PD myofibers, since PD myotubes do not show autophagic buildup[50]. We have established in PD myofibers that GHF201 can enhance autophagic activity, determined by reduction in the levels of the autophagic substrate LC3 (Fig. 8A left panel & Fig. S5B) and reductions in LC3-II and p62 (Fig. S5). These ameliorating effects of GHF201 were not observed in myofibers derived from wild type littermates, which served as a reference due to their typically low levels of autophagic debris accumulation. We also tested whether GHF201 can modulate autophagic homeostasis in PD muscles extracted post-treatment not only by enhancing lysosomal degradation, but also by activating mTORC1. mTORC1 is an

anabolic master switch which can suppress autophagosome formation. While mTORC1 activation typically inhibits autophagy under healthy, physiological conditions, restricting upstream autophagosome initiation in the context of PD is a highly effective strategy to resolve the characteristic autophagic block. In PD muscle, lysosomal dysfunction suppresses the Rag-mTORC1 axis, driving hyperactive, futile autophagosome formation that severely congests the cell[51]. Consequently, genetic suppression of autophagosome formation (e.g., via Atg7 knockout[52]) or direct genetic reactivation of mTORC1 (via TSC knockdown[53]) has been shown to strikingly clear the pathological autophagic buildup in Pompe mice. Thus, lysosomal activation by GHF201 is anticipated to reactivate mTORC1 via the Rag GTPase axis, thereby pacing down the continuous generation of new autophagosomes. Our results (Fig. 8A, right panel) indeed show that GHF201, known to act via lysosomal activation[54], increased the phospho-S6/S6 ratio as a biomarker for active mTORC1 signaling. By restricting the initiation of new autophagosomes, GHF201-mediated mTORC1 activation likely relieves the severe intracellular bottleneck. This upstream attenuation of autophagosome formation complements GHF201's direct lysosomal activation, allowing the compromised degradative machinery to successfully clear the pre-existing autophagic payload.

GHF201 can alleviate oxidative stress and correct deficient differentiation and atrophy in Gaa$^{-/-}$ mice

Excessive production of noxious radicals is an established pathogenic factor in PD muscle. While in PD fibroblasts we observed attenuation of mitochondrial ROS production (Fig.5B), ROS production is notoriously enhanced in PD muscle possibly due to its relatively high, ROS-generating, mitochondrial activity. In addition, the accumulation of glycogen-filled autophagic vacuoles and even glycogen-filled mitochondria[55] and the cell-disruptive muscle fiber degradation and accumulation of autophagic debris are more extensive in PD muscle cells, as compared to fibroblasts. In addition, as opposed to patient derived fibroblasts, no significant change in mitochondrial content (assessed by subunits of ETC complexes I (NDUFB8), II (*SDHB*), and IV (MTCO1), Fig. S6A) was observed in EDL myofibers. This result suggests that the increase in ROS production observed in *Gaa*$^{-/-}$ muscle tissue could not be buffered by an induced increase in mitochondrial content and are therefore more pronounced than in PD patient-derived fibroblasts. Therefore, we tested the effect of GHF201 on oxidative stress in PD muscle. We show that

GHF201 can lower ROS production, determined by the CellROX reagent (Fig. 8B). These ameliorating effects were observed in myotubes (Fig. 8B left panel & Fig. S6B) as well as in myofibers (Fig. 8B right panel & Fig. S6C) derived from *Gaa*$^{-/-}$ mice, but not in wild type littermates with a relatively low basal autophagic stress which can generate this GHF201-attenuated ROS. We have also tested the effect of GHF-201 on the accumulation of lipofuscin inclusions, accepted as a general biomarker for oxidative and lipid peroxidation pathogenic stress in PD[7]. According to our results (Fig. 8C, Fig. S6D, and Video S1), in vivo treatment with GHF-201 significantly reduced lipofuscin accumulation in single muscle fibers from *Gaa*$^{-/-}$ mice. As myological development is deficient in PD, we decided to also test the effect of GHF201 on muscle differentiation. Our results (Fig. 9) show that the compromised rate of differentiation in *Gaa*$^{-/-}$ mice, as compared to WT, was partially corrected by GHF-201 treatment, as shown by increases in both the levels of MEF2C, a muscle differentiation biomarker (Fig. 9A (immunofluorescence, lower panel) and myotube numbers (Fig. 9A, brightfield images, upper panel). MEF2C quantification is shown in Fig. 9A lower panel. Compromised development in both PD mouse model and patients results in increased muscle atrophy resulting in diminished myofiber size[55]. Based on a recent publication[56] which discovered a direct relation between the number of nuclei per myofiber and the eventual myofiber size, we decided to determine the effect of GHF201 on myofiber nuclear count. Our myofiber nuclear count results (Fig. 9B, H&E staining, upper panel and Fig. 9B, nuclear count, lower panel) indicate that both IM-injected and orally-administered ND-GHF-201 can significantly increase myofiber nuclei count and therefore the compound is potentially beneficial for countering muscle atrophy in the PD mouse model. Please note that nuclei in wild type syncytia can be obscured by the relatively thick myotubes[56] and are therefore used mostly as a qualitative rather than quantitative reference (Fig. 9B, upper panel).

GHF201 enhances basal insulin secretion whereas GYS1 inhibition enhances glucose-stimulated insulin secretion in Gaa$^{-/-}$ *mice*

We opted for testing for the first-time pancreatic islet insulin secretion as a proxy for a systemic metabolic condition in PD and its possible resolution or correction by GHF201. Interestingly, we discovered that GHF-201 exerts a beneficial effect only on basal insulin secretion and not on glucose-stimulated insulin

secretion (GSIS). Conversely, the GYS1 inhibitor and glycogen reducing drug guaiacol[57, 58] exerts a beneficial effect on GSIS and not on basal insulin secretion (Fig. 10A, left panel). To note, guaiacol was not tested here in depth as a PD therapeutic candidate since it did not significantly reduce muscle glycogen (Fig. S7A), which is expected given guaiacol's relatively high IC50 against GYS1 (10 μM[57], as compared to 0.041 μM[20] for the effective, PD ameliorating compound MZ-101). This interesting observation on the effect of GHF201 is supported by our untargeted plasma metabolomic analysis of the same animals (Fig. 10C & S7B&C). Our Partial Least-Squares Discriminant Analysis (PLS-DA, Fig. 10B) shows a clear separation among all groups with guaiacol-treated animals being more remote from untreated animals as compared to GHF-201-treated animals which showed some overlap with the untreated animals. Fig. S7B&C presents heatmaps showing metabolites significantly altered (One-Way ANOVA) in GHF201 and guaiacol treated *Gaa*$^{-/-}$ mice. These heatmaps show that the effect exerted by guaiacol was different from the effect of GHF201 which was more similar to that of non-treatment. The volcano plot in Fig. S7D&E bottom panel shows the metabolites whose plasma levels are significantly different between GHF-201-treated and untreated animals. It is evident that as compared to guaiacol less metabolites were significantly affected by the GHF-201 treatment in agreement with the overall lower metabolomic shift produced by GHF-201)). Notably, both GHF201 and guaiacol did not significantly modify the glycemic status of the treated mice (Fig. S7F). Figs. 10C and 10D (upper panels) show Variables Importance in Projection (VIP) - the metabolites which significantly contribute to the classification of the metabolome as that of treated *vs* untreated animals. Metabolite set enrichment analyses (MSEA, Figs. 10C lower panel (GHF201) and 10D lower panel (guaiacol)), combined with VIP results providing confirmation that the metabolites comprising the modified pathways are important, suggest that GHF-201 support the respiratory, relatively slower ATP turnover sustaining basal insulin secretion[59-61], while guaiacol supports the glycolytic, relatively faster ATP turnover sustaining GSIS[59, 62]. For instance, GHF201 significantly enriched the malate-aspartate shuttle pathway (Fig. 10C lower panel). The malate-aspartate shuttle, allowing cytosolic NADH to reach the mitochondria, positively regulates OxPhos and thus aligns with the activating effect of GHF-201, known to improve mitochondrial function[23, 30, 31], on basal insulin secretion. Fig. 10D lower panel demonstrates the

increases in Asp, Glu, and malate in plasmas of GHF-201 treated mice, which aligns with the positive enrichment of the malate-aspartate pathway. Asp is also a key variation-contributing metabolite as shown in Fig. 10C middle panel. On the other hand, a key pathway positively enriched in guaiacol-treated mice is glycolysis (Fig. 10D lower panel), as determined by the increases in the glycolytic intermediates dihydroacetone phosphate, pyruvate and phosphoenolpyruvate (Fig. 10D middle panel). Glycolysis enables the relatively fast ATP turnover required for GSIS. Interestingly, guaiacol also significantly enhanced the pentose phosphate pathway. A recent publication[63] suggests that activation of the pentose phosphate pathway and, concomitantly, increased conversion of NADP+ to NADPH can activate GSIS through activation of mitochondrial and cytosolic isocitrate dehydrogenase synthases and reverse (reductive) citric acid cycle (CAC) flow, suggesting that GSIS is not only supported by glycolysis, it might even be diminished by oxidative CAC flow, vital for OxPhos, or enhanced by reductive CAC flow.

GHF201 alleviates motor dysfunction and increases survival in $Gaa^{-/-}$ mice

The myopathy characterizing both PD patients and *$Gaa^{-/-}$* mice is manifested in mice as reduced locomotion in an open field and as compromised grip strength[64]. Therefore, we tested whether GHF201 can improve these motor deficiencies. Our results show that GHF201 can significantly increase grip strength in *$Gaa^{-/-}$* mice (Fig. 11A). Moving distance in an open field, which is dependent on muscle strength, but also on other cognitive parameters, can also be significantly improved by GHF201 (Fig. 11B). We have also demonstrated that GHF-201 can increase the survival of $Gaa^{-/-}$ mice (Fig. 11C). In the *$Gaa^{-/-}$* mouse model, mortality is typically a late-stage manifestation, leading to low event density.

Survival analysis (log-rank test) revealed a strong trend toward extended lifespan in GHF-201-treated *$Gaa^{-/-}$* mice ($p < 0.08$). Because mortality events are relatively rare in this specific strain, the statistical power of the curve comparison was inherently constrained. However, the calculated hazard ratio (HR) was 0.13, demonstrating a profound 87% reduction in relative risk, and indicating a robust stabilization of the *$Gaa^{-/-}$* phenotype by GHF201. These findings suggest that GHF201 provides robust protection against lethal disease progression and effectively mitigates the low-frequency but critical mortality events driven by progressive GAA deficiency.

Discussion

PD is caused by GAA deficiency. However, full restoration of GAA levels is not expected to completely cure PD as some irreversible cellular damage, which cannot be corrected by GAA re-introduction, always accrues (even when efficient ERT is initiated at birth[65], or *in utero*[66]), especially in muscle cells. For instance, we[50] demonstrated mitochondrial and oxidative cell damage along the "lysosomal-mitochondrial axis" which is initiated by inefficient lysosomal degradation. Additionally, autophagic debris and release of toxic content of overladen lysosomes due to their rupture causes cell damage in PD muscles to reach a point-of-no-return even before restoration of GAA activity. Rather than GAA replenishment through ERT or GT, another therapeutic approach for PD is enhancement of lysosomal function. This work presents preclinical evidence supporting the use of the novel autolysosomal activator GHF201 for treating PD. The advantage of this approach is that it focuses on the underlying cause of PD as an LSD, *i.e.*, lysosomal dysfunction.

PD pathology includes phenotypes beyond the defective GAA: The accumulation of any lysosomal substrate, not only glycogen, leads to lysosomal swelling and compromises lysosomal activity, leading to collateral damage, which might be as important as the direct GAA deficiency, or restriction of salvage of lysosomal glycogen. Lysosomal dysfunction on its own, caused by the accumulation of poorly digested glycogen in *Gaa*$^{-/-}$ mice can dysregulate mTOR signaling, lead to aberrant mitophagy thus enriching cells with dysfunctional mitochondria, and cause lysosomal rupture leading to spilling of its potentially toxic content into the cytoplasm. Therefore, since GHF201 has indeed improved lysosomal function by enhancement of autophagic and autolysosomal flux (Figs. 2 and 7), it is anticipated to ameliorate PD pathology also in patients because the pathology in PD patients also results from lysosomal dysfunction. Translation of a preclinically discovered disease-modifying therapy such as GHF201 to patients usually involves patient stratification to match therapeutic regimen with patients' disease severity and unique clinical status. Interestingly we found that the autophagic, lysosomal and mitochondrial dysfunction phenotypes described in PD fibroblasts is correlative to the disease severity in IOPD and LOPD patients. Here IOPD as compared to LOPD cells show a deeper organelle dysfunction phenotype correlated with GAA

activity levels and clinical description (Fig. S1C). Moreover, a proportional corrective effect of GHF201 according to the PD type is observed, with IOPD being more responsive to GHF-201 than LOPD. These novel results using PD patients' fibroblasts, grading PD severity in vitro, may serve as a reliable personalized medicine platform for therapeutic testing and evaluation in the future.

Given the dysfunctional lysosomal-mitochondrial axis, we expected to observe an increase in mitochondrial ROS production, associated with increased oxidative damage. However, it came to us as a surprise that PD cells presented with lower, rather than higher, ROS production (Fig. 4C), despite their lower OCR (Fig. 4B) and MMP (Fig. 4C), which align with ROS-generating ETC inhibition according to classical modular kinetics[45]. We propose that this decreased mitochondrial ROS production in PD cells is ascribed to the increased mitochondrial mass causing fuel to be distributed among more mitochondria, thus generating less ROS and attenuated per-mitochondrion electron flux and MMP. With a larger mitochondrial population, the cell can meet its energy needs without maintaining a very high MMP. This lower MMP acts as a "safety valve," preventing the buildup of electrons and their leak to form ROS. This decreased mitochondrial ROS production also aligns with the increased SOD1 expression in murine PD muscle[67]. In addition, the higher levels of ETC core proteins and of mtDNA content likely reflect a compensatory increase in mitochondrial biomass and induction of mitochondrial biogenesis. This phenomenon reflects a cellular endeavor to quantitatively compensate for the presence of inefficient or damaged mitochondria, by generating more of them, since their quality cannot be modified. This is a common response to mitochondrial stress. We also observed that in PD muscle a panel of proteins involved in regulation of mitochondrial function, calcium homeostasis and control of oxidative stress are compensatorily up-modulated[50]. The mitochondrial biogenesis factor Nrf-2 was also activated in PD muscle[67].

Being an acidic organelle, which houses acidic hydrolases (including GAA), the lysosome is very sensitive to pH changes and lysosomal alkalization has been observed in PD models, while lysosomal re-acidification corrected the phenotype[68]. Thus, as GHF-201 can restore lysosomal pH[23], it should be a promising therapy for PD, probably capable of improving the function of residual GAA and other lysosomal hydrolases, which

is optimal at the acidic pH of the lysosome. In GSD4 models, GHF-201 ameliorated the diseased state by enhancing lysosomal glycogen catabolism and autophagy through interaction with LAMP1[23]. Importantly, in these GSD4 skin fibroblasts, which were starved for 48 h followed by the glycogen burden-generating high-glucose medium replenishment, GHF-201 enhanced autophagy[23, 31].

While autophagic suppression by Atg7 knockout actually ameliorated PD in a mouse model[52], it has to be realized that the pathogenic autophagic buildup in PD is a result of both autophagy induction (mediated, among other factors, by Atg7) and inhibition of autophagosome clearance mediated by their fusion with lysosomes. Thus, mTORC1 re-activation by GHF201 (Fig. 7A right panel), blocking autophagosome formation, can be beneficial to PD[53], just as activation of lysosomal and autolysosomal activity[69], as proposed here. In addition, GHF-201 reduced cellular glycogen in vitro and myological glycogen ex vivo (Figs. 2A and 5C right panel) and increased the levels of the transcription factor TFEB (Fig. 3C), already shown to be beneficial for PD fibroblasts as an inducer of autophagy[69, 70]. Importantly, we analyzed the effect of GHF201 on a model of another myopathy – GSD3 (a hepatopathy with a later-stage myopathy)[30]. In that work we also showed that GHF-201 improved motor performance (open field and grip strength) in GSD3 modeling *Agl*$^{-/-}$ mice, especially at a relatively advanced stage of the disease. Common to this work, GHF201 also corrected muscle atrophy in GSD3. However, in contrast to the current study, the effect of GHF201 on myological differentiation was not assessed in *Agl*$^{-/-}$ mice. Nevertheless, muscle differentiation from satellite cells-derived myoblasts to myotubes to myofibers does not only play a role in embryonic development. This differentiation also takes place continuously throughout life, countering normal wear and tear of muscle through muscle remodeling, hence the importance of accurate determination of the effect of GHF201 on muscle differentiation (Fig. 8A) involving its quantification by the muscle differentiation biomarker MEF2C.

Common to all our ex vivo results (Figs. 6-9) is the interesting observation that while GHF201 was applied in vivo, its effect persisted ex vivo even though it wasn't applied ex vivo. These observations suggest that GHF201 induced lasting epigenetic/cellular changes. Ex vivo persistence of in vivo applied drugs through epigenetic remodeling is a known phenomenon. The most well-established examples are DNA-

Methyltransferase-Inhibitors (DNMTi), such as Azacitidine[71], which trap DNA methyltransferases on the DNA preventing DNA methylation during subsequent cell divisions, and histone deacetylase inhibitors (HDACi)[72], which increase histone acetylation leading to a more open chromatin structure with altered gene expression. In the case of GHF201, we can envision several mechanisms of action through which GHF201 in vivo treatment can lead to a perennial effect persisting ex vivo. For example: 1. Enhancement of autophagic/lysosomal degradation of lipids and of glycogen to glucose by GHF201 can increase the levels of acetyl-CoA which is a substrate of histone acetyltransferases (HAT) epigenetic "writers" and histone deacetylases (HDAC) epigenetic "erasers": HATs use acetyl-CoA (a product of glucose and fatty acid metabolism) as a substrate for histone acetylation. HDACs remove acetyl groups. Autophagic/lysosomal breakdown of lipids can thus influence acetyl-CoA levels. 2. GHF201-mediated modulation of DNA methyltransferases (DNMTs) and demethylases (TET (ten-eleven translocation) dioxygenases): DNMTs use S-adenosylmethionine (SAM) as a methyl donor. SAM is generated from single carbon metabolism, which can be influenced by amino acid availability derived from autophagic degradation, enhanced by GHF201. Moreover, α-ketoglutarate, whose main source is healthy mitochondria, which can be increased by GHF201-mediated enhancement of autolysosomal function, is a key co-factor of TET dioxygenases which mediate DNA demethylation and subsequent gene expression.

Another notable innovation of our study is our innovative delivery approach. The unique technology of liquid nano-droplets (ND) is an innovative vehicle fabrication method whose main advantage, compared to other nano-formulated excipients, is the maximization of the surface area onto which the bioactive can be loaded. This results in high loading capacity which advantageously reduces the volume of administration. Moreover, NDs keep the bioactive dissolved in a liquid-state and thus improve its local distribution, as they allow its solubility in the biological medium and prevent its precipitation and local deposition at the membrane target site. At that site the NDs facilitate an intimate contact with the target membrane, according to its chemical composition, *e.g.*, a sarcolemmal membrane, or, as done previously, the enterocyte membrane. Upon contact with the membrane, the NDs modulate the lipid membrane and affect its microviscosity, expediting the passage of the bioactive through it. We have characterized ND-

GHF-201. Based on light transmission (Fig. 5B), ND-GHF-201 was found physically stable for the clinically acceptable period of at least 3 years, and also had <0.6wt% impurities showing acceptable chemical stability.

In summary, our results strongly suggest that GHF-201 can improve lysosomal function and thus is an apt therapeutic candidate for PD, where this function is compromised. Moreover, correction of autophagic/lysosomal dysfunction is a leading strategy in PD and LSD treatment development, as shown, for instance, by the extensive research on the transcription factors TFEB and TFE3, regulating lysosome and autophagosome biogenesis, and on inhibition of the autophagic inhibitor mTOR[73]. The unresolved issues of ERT and GT described above, the complete safety and efficacy of GHF201, demonstrated also in the clinic in APBD, and GHF201's unique delivery by tailored and possibly tropic nanodroplet (ND) formulations posit our new approach as an innovative, safe, and promising alternative or adjunctive therapy to PD.

Materials and Methods

Cells

Patients and cell culture. Primary Skin fibroblasts were isolated from skin biopsies of 6 IOPD, and 3 LOPD PD patients (See Table 1). Informed written consent to participate in the study was obtained from all individuals or their parents in the case of minors. The study was approved by the ethics committee of -the State of Israel Ministry of Health-Rambam Medical Center (IRB 0176-18-RMB).

Age and gender matched healthy controls (HC) were purchased from Coriell Institute (New Jersey, USA) (See Table 1). Primary fibroblasts were then expanded in culture media DMEM supplemented with 1% MEM Sodium Pyruvate, 1% PSA, 10% heat inactivated FBS, and 1% 100x non-essential amino acids solution in polystyrene plastic 75-cm^2 culture flasks at 37°C with 5% CO2. Cell passages and expansion of human skin fibroblasts were performed when cells were at 80-100% confluency. Cell passaging and re-plating was accomplished using 0.25% Trypsin-EDTA for 2 minutes, followed by addition of twice the volume of a complete culture media to neutralize the enzyme. Cells were subsequently centrifuged at 1,200 rpm for 5 min before their pellets were resuspended in 1 ml full medium for cell counting using the TC10 automated

cell counter (BioRad USA) before re-plating. All PD and HC samples (See Table 1) were used for each experiment unless mentioned otherwise. All experiments were performed between passages 8– 16 as this range was determined as an adequate passage range in previous studies[30, 33].

Additional cell controls. GFER and MNGIE skin fibroblast samples (see Table 1) were obtained and used as positive and negative disease controls for this study in the Seahorse XF assay as explained below. Informed written consent to participate in the study was obtained from all individuals or their parents in the case of minors, following the ethics committee of the State of Israel-Sheba Medical Center (5672-28-SMC).

Antibodies

MEF2C (D80C1) XP® Rabbit mAb (cat #5030), LC3B (D11) XP® Rabbit mAb (cat #3868), S6 Ribosomal Protein (5G10) Rabbit mAb (cat #2217), Phospho-S6 Ribosomal Protein (Ser235/236) Antibody (cat #2211), Anti-rabbit IgG (H+L), F(ab')2 Fragment (Alexa Fluor® 594 Conjugate) (cat #8889), Anti-rabbit IgG (H+L), F(ab')2 Fragment (Alexa Fluor® 488 Conjugate) (cat #4412) and Anti-rabbit IgG, HRP-linked Antibody (cat #7074), Rb-TFEB(D207D), and Rb-LC3(2775S) were all from Cell Signaling. p62 (SQSTM1) Rabbit mAb (cat. # AB109012), PINK1 Rabbit mAb (cat. # ab216144), NDUFB8 Mouse mAb (cat. # ab110242), MTCO1 Mouse mAb (cat. # ab14705), SDHB Mouse mAb (cat. # ab14714), ATP5A Rabbit mAb (cat. # ab176569), UQCRC2 Mouse mAb (cat. # ab14745), and PGC1α Goat pAb (cat. # ab106814) were all from AbCam.

Reagents

GHF-201 (previously designated as compound 144DG11; CAS Registry Number: 1257155-76-2) is a small molecule autophagic activator. Its full IUPAC chemical name is: 1,2-dihydro-N-(2-methoxyethyl)-6-methyl-N-[(3-methyl-2-thienyl)methyl]-2-oxo-4-pyridinecarboxamide. Dulbecco's Modified Eagle's Medium(DMEM X1), Fetal Bovine Serum (FBS, Qualified, A5256701), Sodium Pyruvate 100mM (×100, 11360070), Minimum Essential Medium Non-Essential Amino Acids (×100) (MEM NEAA, 11140050), 0.25% Trypsin-EDTA (X1, 25200056), Dulbecco's Phosphate Buffered Saline (DPBS) without Calcium and Magnesium(14190144), Hanks' balanced salt solution(HBSS) with Calcium and Magnesium(24020117)

were from Gibco. Pen-Strep-Ampho.B Solution (×100) (PSA, 12352207) was from Sartorius. Dimethyl sulfoxide (DMSO), ANTIMYCIN A from *Streptomyces sp.* (A8674), Oligomycin A >= 99% (HPLC, 75351), Rotenone (R8875), Carbonyl Cyanide P-Trifluoromethoxy (C2920), D-(+)-Galactose(G5388), Hoechst 33342, RIPA buffer (20-188), BCA protein assay kit (23225) were from Sigma. Seahorse XFe96/XF Pro FluxPak (103793-100), XF DMEM Medium, pH 7.4, 500 mL (103575-100), XF 1.0 M Glucose Solution, 50 mL (103577-100), XF 200 mM Glutamine Solution, 50 mL (103577-100), XF 100 mM pyruvate solution, 50 mL (103578-100) were from Agilent Technologies. CyQUANT™ Cell Proliferation Assay (C7026), Calcein AM (Green, C3099), Calcein AM (Red, C3100), Phenol-red free DMEM (A14430-01), MitoSox red(M36008), Fast SYBR Green Master Mix (4385612), TMRE (T6690) were from Thermo Fisher/Invitrogen. 96 glass-bottom well plates (P96-1.5H-N) were from Cellvis. 10 cm dishes (431110) were from Corning, ECL super signal kit (34579) was from Pierce Biotechnology, MES SDS running buffer (NP0002), SeeBlue® Plus2 Pre-stained protein standard ladder (LC5925), reducing buffers (NP0004) were from Life Technology, DNeasy blood and tissue kit (69506) was from Qiagen. GAA enzyme activity kit (MAK129-1KT) and PAS assay kit (cat.101646) were from Merck. Vinblastine (11762) was from Cayman. MitoQ (845959-50-4) was from Med Chem Express. Histopaque® (cat #11191), Histopaque® (cat #10771) and RIPA buffer (cat #R0278) were from Merck. Protease & Phosphatase Inhibitor Cocktail (cat #78440) and Coomassie Protein Assay Reagent (cat #1856209) were from Thermo Scientific. Chick Embryo Extract, Ultrafiltrate (CEE) (cat #C3999) were from United States Biological. Mouse IFN-gamma Recombinant Protein (Cat #315-05) were from PeproTech®. Matrigel® Basement Membrane Matrix (cat #CLS354234) were from Corning. CellROX™ Deep Red Reagent, for oxidative stress detection (Cat #C10422), was from Invitrogen. Insulin, human recombinant, zinc solution (Cat #12585014) was from Gibco. Mouse Insulin ELISA (Ultra Sensitive) kit (cat #90080) was from Crystal Chem. Collagenase P (cat #11213865001) was from Roche.

Seahorse XF Mito Stress Test in fibroblasts

The experiment's parameters were determined following several calibration experiments to determine appropriate cell numbers, compounds concentrations and optimal cell count methodology. Primary fibroblast cells were seeded at a concentration of 20,000 cells/well in a Seahorse XF96 cell culture

microplate. The seeded cells were kept for 24 h in a standard growth medium (10% FBS and glucose) to allow full adherence to the wells. Medium was subsequently replaced to 24h with no glucose and no FBS starvation media, with 50µM GHF-201 or 50µM DMSO as a control. A day before the assay, each well of the calibration plates was filled with 200 µl calibration solution and placed in a CO2-free incubator at 37°C for at least 12 h before the experiment. On the day of the assay, the cells were washed three times with 200 µl of pre-warmed Seahorse media, prepared according to the manufacturer's instructions, and incubated with 180 µl of that same media for 45 minutes in a CO2-free incubator at 37°C to allow for temperature and pH equilibration. Injection ports of the Seahorse XF assay cartridge were loaded with the assay reagents at 10X of the final concentration in the assay medium. The high concentration of the recommended concentration range by Agilent was used (see Reagents), 20µl of Oligomycin (2.5 µM), 20 µl of FCCP (2 µM), and 20 µl of Antimycin A (0.5 µM) + Rotenone (0.5 µM) were added to ports A, B, and C, respectively. In port D, 20 µl Seahorse media was placed to maintain equilibrium. The calibration plate and cartridge were placed in the Seahorse XF96 analyzer for calibration, using the standard XF calibration protocol. Following calibration, the calibration plate was replaced with the cell plate, and the experiment began. Throughout the experiment, OCR levels were recorded in each well at 3 time points following the injection of each reagent. To normalize the results to cell count, the CyQUANT Proliferation Kit was used following the manufacturer's protocol. In brief, the cells were washed with 200µL PBS per well and frozen in the microplate at -80°C to ensure subsequent cell lysis. The cells were thawed and resuspended vigorously in 200µL of 1x cell-lysis buffer supplemented with 1x CyQUANT GR dye per well. The resuspended cells were incubated in the dark for 5 min at RT, whereupon fluorescence was measured at 3 different wavelengths and later averaged. (Excitation: 465nm, 480nm, and 495nm; Emission: 510nm, 520nm, and 530nm, respectively). DNA content measurements were then averaged and compared to a previously established standardization curve to estimate the cell count, ensuring accurate normalization of the OCR data. Positive and negative cell population controls were added to the experiment to establish proper maximal and minimal OCR values: MNGIE fibroblasts (TYMP mutation) were used as a negative cell disease control as these cells are known to present ETC dysfunction, leading to reduced OCR, through

primary and secondary mitochondrial dysfunction[42, 43]. GFER mutation fibroblasts (referred to as AV) present with a rare mutation in growth factor Erv1-like, also known as ALR, which were used as a cell disease positive control. A decrease in GFER function has been linked to mTORC1 signaling pathway over-activation[40]. This pathway, in turn, can lead to an increase in the expression of genes involved in OxPhos, an increased rate of electron transfer, and consequently, a higher OCR and enhanced mitochondrial metabolism[41].

TMRE and imaging of mitochondrial ROS production in cells

HC and PD cells were seeded at a density of 2,000 cells/well on 96 glass-bottom well plates. The seeded cells were kept for 24 h with standard medium (containing glucose and 10% FBS) to allow attachment, followed by a change in media according to the preferred condition of the experiment: 24h with no glucose, no FBS starvation medium with 50 µM GHF201 or 50 µM DMSO. For TMRE live imaging, 5 µM Hoechst, 0.83 µM calcein AM, and 0.05 µM TMRE were diluted in DMEM phenol-red free, serum-free medium, mixed, and added to each well at a volume of 100 µl for 20 minutes at 37 °C in the dark. The cells were then washed with 100 µl HBSS. For the TMRE experiments conditioned positive and negative controls were included. Positive controls were based on ETC activation using a low-glucose, high-galactose media which forces cells to rely on OxPhos[41]. A representative HC sample was treated with low glucose (0.8 g/L), 10% FBS, 1% PSA, 1% NEAA, 1% SP, and 2.3 g/L galactose for 48 hours before seeding the cells for the assay to force increased mitochondrial respiration[74]. Negative controls were based on ETC inhibition using MitoQ (mitoquinone mesylate), a mitochondrial-targeted antioxidant which is known to inhibit ETC activity at high concentrations due to semiquinone accumulation in the mitochondria[75]. A representative HC sample was treated with regular 10% FBS, 1% PSA,1% NEAA, 1% SP, glucose media that contains 1.125µM MitoQ for 48 hours before seeding for the assay.

For the fluorescent determination of mitochondrial ROS production, 10 µM MitoSox red was diluted into phenol-red free DMEM and incubated for 40 minutes at 37°C in the dark. The cells were then washed with 100 µl HBSS, and 5 µM Hoechst, 0.83 µM calcein AM green were diluted in this phenol-red-free, serum-free DMEM, mixed, and added to each well at a volume of 100 µl for 20 minutes at 37°C in the dark. The

cells were then washed with 100 µl HBSS. For both experiments, the plates were transferred to Operetta CLS (1148, Perkin Elmer) for image acquisition at 40x magnification. All assay parameters (including the acquisition exposure times, objective, and analysis parameters) were kept constant for all experiment plates.

SYBR green qPCR

250,000 HC and PD cells were seeded on 10 cm dishes. The cells were kept for 24h with standard medium (containing glucose and 10% FBS) to allow attachment to the dish's bottom, followed by a change of media according to the preferred condition of the experiment (24h with no glucose, no FBS starvation media supplemented with 50µM GHF-201 or 50µM DMSO). Cells were collected and washed with PBS and centrifuged for 5 minutes at 14,000 RPM. Supernatant was discarded and the remaining pellet was resuspended in 200 µl PBS. Total-genomic and mitochondrial-DNA were extracted using the DNeasy blood and tissue kit as per the manufacturer's instructions. Total DNA yield was quantified by Nanodrop. SYBR green reaction was performed using SYBR green FAST master-mix, as per manufacturer's instructions. Both mitochondrial and genomic DNA were amplified with 25ng of total DNA, using the primers listed in Table 2 and following primer and DNA concentration calibrations. mtDNA content, normalized to nuclear DNA was calculated using the following equation: $2\times2-\Delta Ct$ (ΔCt = mito Ct – nuclear Ct). To finalize the experiment nuclear DNA-normalized mitochondrial DNA fold change compared to HC was computed and plotted, in addition unpaired two tailed t-tests based on CT values were used to generate p values.

Periodic Acid Schiff (PAS) assay in cells

For PAS staining of glycogen, PD skin fibroblasts were seeded at 2,000 cells per well and cultured in microscopy-grade 96-well plates for 24 h in complete medium. 50 µM GHF201 treatment was added to half of the PD wells. Cells were washed with PBS and then fixed in 4% PFA and permeabilized with 0.1% Triton X-100. PAS staining was performed using the Merck PAS assay kit, as previously described by us[23, 30, 57]. The PAS-stained cells were imaged using InCell2200 (GE Healthcare, U.K.) with Texas red channel filters. Image analysis for cellular PAS staining was performed using the In Carta image analysis software. Total

intensity was measured, normalized , and compared between groups. The experiment was repeated independently three times.

Glycogen assay

Tissue glycogen was determined biochemically using the Glycogen-Glo(TM) Assay (Promega) following the manufacturer instructions.

Glycemic status

Plasma glucose was determined at the Hadassah biochemistry laboratories by the Glucose Oxidase assay (Siemens Healthineers)

Immunoblotting

HC and PD cells were cultured, seeded in 6 well culture plates and cultured overnight for attachment. Cells were incubated for 24 h in starvation medium. 50 μM GHF201 was added to half of the PD wells. Cells were then washed in PBS, harvested and lysed in a RIPA buffer containing phosphatase and protease inhibitor cocktails. Protein concentration was determined using a BCA protein assay kit. For immunoblotting in mouse murine muscle tissue, muscle was dissected and lysed in the same RIPA buffer. Muscle lysates were cleared by centrifugation at 12,000 RPM for 20min at 4°C. For both in vitro and murine samples equal amounts of protein lysates were subjected to SDS-PAGE on 4–12% gradient gels and electro transferred to a nitrocellulose membrane (iBlot 2, Invitrogen). Membranes were blocked with 5% non-fat milk, incubated at 4°C overnight with primary antibodies, washed, and then incubated with secondary antibodies conjugated to HRP. Proteins were then visualized by chemiluminescence reagent using Amersham Imager 600 (GE Healthcare) and band densitometry was measured using the FIJI software. Experiments were repeated independently three times. Protein bands were normalized to Actin levels in each membrane.

Autophagic flux calculation

$$J = \frac{\text{LC3ii/LC3i(with Vinblastine)}}{\text{LC3ii/LC3i(without Vinblastine)}}$$

Autophagic flux was calculated by the formula below using the data acquired from different blots for each sample averaged across experimental replicates. 50uM Vinblastine was applied 2 hours prior to protein extraction.

Immunofluorescence

PD and HC skin fibroblasts s . were seeded at 2000 cells per well and cultured in specialized microscopy-grade 96 well plates overnight for attachment. Cells were incubated for 24 h in starvation medium. 50 µM GHF201 was added to half of the PD wells. Cells were washed in PBS and then fixed in 4% paraformaldehyde in PBS, washed three times in PBS, permeabilized in 0.1% Triton X-100 in PBS for 5 min and blocked-in blocking buffer (5% BSA in PBS) for 1 h. Cells were then incubated with primary antibodies overnight, followed by three washes in 0.05% Triton X-100 in PBS and incubation with secondary antibodies and counterstaining with 1.6mM Hoechst 33342 (1:1000) and 0.02 mM phalloidin Atto 565 (1:400) for 1 h. Cells were subsequently washed three times in PBS. Images were acquired with 20x magnification using the Operetta High content imaging system. The experiment was repeated 3 times per primary antibody where the assay parameters (including the acquisition exposure times, objective, and the analysis parameters) were kept constant for each antibody. Images were analyzed by the Harmony 4.8 image analysis software using a customized image analysis protocol and quantified for intensity levels of each antibody.

Live Imaging

PD and HC skin fibroblasts were seeded at 2000 cells per well and cultured in specialized microscopy-grade 96-well plates. Following 24 h in complete medium (DMEM with glucose,10% FBS, PSA, NEAA and sodium pyruvate), cells were washed to remove traces of serum and starvation medium (DMEM serum free, glucose and pyruvate free, with PSA) was applied for 24 h and 48 h or for 48 h followed by 24 h with

complete medium (72 h). Before imaging, plates were examined for well quality using a light microscope, following that the cells at the end of their respective time points were washed and a mix of live fluorescent dyes in HBSS was added to each well for 20 min at 37°C in a 5% CO_2 incubator. The final solutions of the different stains were: 1.6mM Hoechst 33342, 0.1 mM LysoTracker Deep Red, 0.05 mM TMRE and 0.4 mM calcein-AM Green. Following the incubation, cells were washed with HBSS, and plates were transferred to an Operetta G1 system for image acquisition at 20× magnification under environmental control conditions at 37°C and 5% CO_2. All the assay parameters (including the acquisition exposure times, objective, and the analysis parameters) were kept constant for all assay repetitions. These experiments were repeated for three consecutive weeks, for a total of 18 plates (6 per condition), each plate containing 60 wells with ~500 imaged cells per well. Images were analyzed by a customized image analysis protocol designed for the experiment using Harmony 4.8 image analysis software, all data analysis steps were performed using Python and R.

Lysotracker, Acridine Orange and cathepsin probe experiments

HC and PD cells were seeded at 2,000 cells per well and cultured in specialized microscopy-grade 96 well plates overnight for attachment. Cells were incubated for 24 h in starvation medium. 50 µM GHF201 was added to half of the PD wells. For Lysotracker staining, 5 µM Hoechst, 0.83µM calcein AM, and 100 µM LysoTracker were diluted in DMEM phenol-red free, serum-free medium, mixed, and added to each well at a volume of 100 µl for 20 minutes at 37°C in the dark. The cells were then washed with 100 µl HBSS. The plates were transferred to Operetta CLS (1148, Perkin Elmer) for image acquisition at 40x magnification. For Acridine Orange (AO), 1 µM of AO was supplemented to the mix.

For the GB123 cathepsin activity probe, a day post-seeding 50 µM GHF-201 was added to half of the PD cells for 24

h. Then media were removed and replaced with media containing 0.25 µM GB123 and incubated for 4 h. Cells were washed with 1XPBS for 3 times and left for 2 h in the last PBS wash. Then PBS was replaced with phenol-red and serum-free DMEM supplemented with 5 µM Hoechst, 0.83µM calcein AM at a volume

of 100 µl for 20 minutes. For both these experiments Images were acquired with 20x magnification using the Operetta High content imaging system.

All assay parameters for all these experiments (including the acquisition exposure times, objective, and analysis parameters) were kept constant for all experiment plates. Prime Image analysis was customized for each experiment using the Harmony 4.8 image-analysis software. Imaging data were analyzed by Python.

GAA activity testing

PD and HC skin fibroblasts were grown in polystyrene plastic 75-cm^2 culture flasks at 37°C with 5% CO_2 with full medium until they reached full confluence. Cells were then trypsinized, centrifuged and counted. Approximately 2.5 million cells per sample were counted. Cells were then washed with PBS and diluted in 400 ul PBS. Cells were lysed by sonication on ice using 3 pulses of 3 seconds each. Cell lysis was validated under a widefield microscope. Cell homogenate was centrifuged at 14,000 g for 10 min at 4°C. Cleared supernatant was transferred to a clean tube which was then stored at -80°C overnight. GAA enzyme activity was measured as per the manufacturer (Merck) instructions. Briefly, a master reaction mix was prepared for all samples. 20 µl of each sample was added to separate wells of the plate. 200 µl of the master reaction mix was added to each of the sample wells and 20 µl of distilled water was added to two separate wells in the 96 well plate. 200 µl of water were added to one of these wells and 200 µl of the calibrator to the other well. The plate was briefly mixed. Initial absorbance was measured using a plate reader at 405 nm (A405) initially. The plate was then incubated at room temperature for 20 minutes. Then final absorbance was determined. A405(final) calculations were as follows: Enzyme Activity (units/L) = [[(A405)final – (A405)initial]*250 units/L] divided by [(A405)calibrator – (A405)water], where (A405)calibrator = value for calibrator at 20 minutes and (A405)water = value for water at 20 minutes. One unit is the amount of enzyme that catalyzes the hydrolysis of 1.0 µmole substrate per minute at pH 7.0.

Animals

GAA knockout ($6^{neo}/6^{neo}$, designated here as $Gaa^{-/-}$)[64], IOPD modeling mice, were a kind gift from Dr. Nina

Raben from the NIH and were used in this study. C57BL/6 littermate mice were the genetic background of these transgenic mice and used as a wild type ($Gaa^{+/+}$) control. All in vivo experiments were approved by the Hebrew University Faculty of Medicine IACUC (approval number 16954). n = 6–10 mice/arm were used. GHF-201 was administered in two ways: Intramuscular administration was via biweekly injection to the gastrocnemius in alternate flanks. The injection consisted of a 50 µL solution of 250 mg/kg GHF-201 in 5% DMSO. 50 µL of 5% DMSO vehicle was used as a vehicle control. Oral administration was through daily oral pipetting of 20 µL liquid ND-GHF201 formulation at 70 mg/kg. 20 µL unloaded ND formulation served as a control. Mice were treated from the age of 3 months to the age of 8 months. Animals' weight was recorded every week. A weight decreases of >10% between biweekly weightings, or >20% from treatment initiation led to removal of the animal from the study. We tested monthly moving distance and cumulative sojourn in the center of an open field and front paw grip strength using a grip strength meter (Columbus Instruments, Columbus, OH, USA).

Myotube culture and differentiation

Extensor digitorum longus (EDL) muscles were dissected from $Gaa^{+/+}$ and $Gaa^{-/-}$ mice. Muscle tissues were enzymatically digested using collagenase, and the resulting myofiber suspensions were passed through a cell strainer to enrich for mononucleated cells. The isolated primary (non-immortalized) myoblasts were cultured on Matrigel-coated cell culture plates. Myoblast proliferation medium consisted of high-glucose DMEM (4.5 g/L glucose) supplemented with 20% fetal bovine serum (FBS), 10% horse serum, 1% chick embryo extract, 3.5 mg/mL recombinant human insulin, 100 U/mL recombinant interferon-gamma (IFN-γ), 1% L-glutamine and 1% penicillin/streptomycin. Myoblasts were differentiated to myotubes using myotube differentiation medium composed of DMEM supplemented with 2% horse serum, 0.5% chick embryo extract, 1% L-glutamine and 1% penicillin/streptomycin[53]. Myotubes were used for the autophagy, reactive oxygen species (ROS) production, mitochondrial bioenergetics, and myotube differentiation experiments. No *in vitro* treatments were given to myotubes.

Muscle fixation and single myofiber isolation

Gastrocnemius (GC) muscles were dissected from $Gaa^{+/+}$ and $Gaa^{-/-}$ mice. Muscles were fixed in 0.1M

phosphate buffer/2% paraformaldehyde for 1 h at room temperature and then overnight at 4°C. GC muscles were stored in 50% glycerol at -20°C. For the isolation of single fibers, GC muscles were transitioned into lower concentrations of glycerol. Single myofibers were teased out from muscles under the microscope. Single myofibers were used to study lipofuscin autofluorescence (LAF). For LC3 staining (Fig. 8A), the same procedure used for the GC muscle was applied to the EDL muscle, so that autophagy experiments (LC3 and S6/S6P quantifications) are performed on the same type of muscle. The LAF emission wavelength was separated from other autofluorescence emission wavelengths by merging all the autofluorescence emissions at 405 nm, 488 nm, 561 nm, and 638 nm. Merged autofluorescence was not considered as LAF. Unmerged autofluorescent red dots with 561 nm emission wavelength were considered LAF. Specification of LAF at 561 nm has already been established and demonstrated[76].

Muscle fiber staining

The GC muscle was immersed in 4% paraformaldehyde for fixation, followed by sagittal sectioning and subsequent staining with H&E and/or PAS as detailed above (Merck kit).

Isolation of Islets of Langerhans from mouse pancreas

The islets of Langerhans were isolated by intraductal injection of collagenase P. Following the injection, the pancreas was carefully excised and transferred into glass vials containing collagenase P solution. The vials were then incubated in a 37 °C water bath for 15 minutes and vigorously shaken to facilitate tissue dissociation. The vials were then immediately placed on ice. To isolate the islets, cell suspensions were subjected to density gradient centrifugation using Histopaque (1119 and 1077, Merck) followed by manual hand-picking under a stereomicroscope[77]. Isolated islets were cultured on Matrigel-coated well plates followed by mitochondrial bioenergetics and basal and glucose stimulated insulin secretion (GSIS) assays.

Basal and glucose stimulated insulin secretion assays

Islets were pre-incubated for 1 h at 37 °C in Krebs-Ringer bicarbonate HEPES buffer containing 2.8 mM glucose. Following pre-incubation, islets were incubated for 1 h in KRBH with 2.8 mM glucose to study basal insulin secretion. The supernatant was collected and stored at −20 °C. To study GSIS, the same islets were

then transferred to KRBH containing 16.7 mM glucose and incubated for an additional 1 h at 37°C. Supernatants were again collected and stored. After the glucose stimulation phase, islets were lysed in acid-ethanol (0.18 M HCl in 70% ethanol) and stored overnight at 4 °C to extract total intracellular insulin. Insulin levels in supernatants and lysates were measured using a mouse insulin ELISA kit (Mouse Insulin ELISA (Ultra-Sensitive), catalog# 90080, Crystal Chem) according to the manufacturer's instructions.

Mouse plasma metabolomics

LCMS metabolomics analysis was performed on mice plasma as follows. Dionex Ultimate 300 high-performance liquid chromatography (UPLC) system coupled to an Orbitrap Q-Exactive plus Mass spectrometer (Thermo Fisher Scientific) with a resolution of 70,000 at 200 mass/charge ratio (m/z), electrospray ionization in the HESI source, and polarity switching mode to enable both positive and negative ions across a mass range of 70 to 1000 m/z, was used. The UPLC setup included a ZIC-pHILIC column (SeQuant; 150 mm × 2.1 mm, 5 µm; Merck) with a Sure-Guard filter (SS frit 0.5 µm). Five µL of the plasma extracts were injected and the compounds were separated with a mobile phase gradient of 15 min, starting at 20% aqueous (20 mM ammonium carbonate adjusted to pH 9.2 with 0.1% of 25% ammonium hydroxide) and 80% organic (acetonitrile) and terminated with 20% acetonitrile. The flow rate and column temperature were maintained at 0.2 mL/min and 45 °C, respectively, for a total run time of 26 min. All metabolites were detected using mass accuracy below 5 ppm. Thermo Xcalibur was used for the data acquisition. Data processing and analysis were carried out using Compound Discoverer version 3.3.2.31. In total, 174 metabolites were identified through this platform. The identification process utilized an in-house spectral library and MS2 data comparison with the mzCloud and MzVault databases. Metabolomics data were analyzed using Metaboanalyst 6.0. Metabolites with more than 33% missing values were removed, metabolites that were near-constant throughout the groups were detected using a 20 IQR variance filter. Samples were normalized to the HC group and scaled using logarithmic normalization.

Data analysis and statistics

In vitro analyses. Data processing stages in the in vitro experiments were done using Python 3 and R (vs

4.2.2), scripts are available in the following link https://github.com/Urisprecher).For imaging data, Image analysis and downstream analysis was guided by [78]. prime Image analysis was customized for each experiment using the Harmony 4.8 image-analysis software. For live imaging, the analysis of high content analysis experiments included quality control per plate, batch effect analysis following[79], and testing for unwanted sources of variation (*i.e.* patient gender, week of experiment) using variance calculation by the variance Partition package[80], as was shown by us[81]. Well processing and removal was based on cell count and Local Outlier Factor (LOF) for outlier identification[82], to remove wells with extreme values. The analysis focused on biologically relevant markers for nuclei, cytoskeleton, and mitochondrial-related features and feature selection using backward feature elimination was utilized to remove correlated features and to select equal number of features per organelle to allow an unbiased approach for the multivariate analysis (Fig. 1). To this end, feature types (*i.e.*, texture, area, intensity) are not equal between different labeled organelles as a result of image analysis which generated feature types for each organelle based on segmentation preferences and biological interest. Finally, multivariate analysis highlighting ideal dimension reduction algorithms were chosen based on their overall fit to the data[83]. For TMRE, ROS, Lysotracker, AO, cathepsin activity and Immunofluorescence experiments following image analysis data was subjected to quality control steps such as cell count filtering, outlier detection and feature quality control. The Seahorse Mito Stress test analysis was performed using R. After applying the cell count normalization to the results and scaling all the plates with an appropriate scale factor (OCR\pmol\min\20,000 cells) using the Wave software. Initial OCR plots for data visualization were created to assess data quality and consistency across plates before merging them. The analysis steps included data processing and filtering, both manually based on experimental observations as well as automatic filtrations for missing and incorrect values based on OCR trends across different intervals, and an automatic outlier detection based on interval and well exclusions, eliminating measurements based on deviations from the group mean for each fibroblast ID. Detailed scatter plots, logarithmic transformations to reduce the dependency of standard deviation on mean OCR, and logarithmic normalization assessment were performed before finalized datasets are prepared for rigorous statistical

analysis. Data analysis was guided and developed based on [84].

Statistics. For calculating p-values (in vivo, ex vivo and in vitro), we implemented the following approaches: For experiments involving multiple groups, pre-specified biologically relevant pairwise comparisons were performed using two-tailed unpaired t-tests. To control for multiple testing within each experiment, p-values were adjusted using the Benjamini-Hochberg false discovery rate (FDR) procedure. statistical testing by 2 tailed unpaired t-tests was performed to compare groups using GraphPad Prism 9, or using two-sided t-tests through an R script adapted from the GitHub page provided above, unless otherwise mentioned. Throughout the manuscript p values under 0.05 were considered significant and p-values between 0.05 and 0.1 were considered a trend. We present the actual p values for full transparency and as we strongly believe p values require context and not a defined threshold[85, 86]. In this work t-testing was used since it qualifies as a more valid approach for our experiments which are mostly focused on comparing essentially 2 groups at a time, performing independent t-tests restricted to the pre-specified comparisons provides a more targeted and statistically efficient approach as It maintains appropriate control of type I error while maximizing power.

In addition, as extremely small sample sizes, which are occasionally used in this work (e.g., n=3), result in lower statistical power, a higher p-value threshold allowed us to identify potentially meaningful differences between groups. In addition, we have focused the statistical analysis in the in vitro section of this manuscript on 95% bootstrap mediated confidence intervals and effect sizes rather than the conventional p value threshold.

In HCA imaging-based experiments, we used wells to represent an independent experimental unit to which treatments or culture conditions were separately applied. Statistical comparisons were therefore conducted using wells as the unit of analysis. This approach satisfies the key requirements for independent observations: (1) treatments were independently assigned and applied to each well, (2) measurements were obtained independently, and (3) wells did not influence each other during culture or imaging. It is important to note that conclusions are drawn at the level of cellular responses in wells derived from patient samples, rather than at the level of patients themselves, this distinction is explicitly

acknowledged in the interpretation of results[87].

For statistical analysis of data from live imaging high content analysis experiments (Figs. 1, 3-4), data was normalized to logarithmic scale to achieve normally distributed features for statistical testing. Sample size was computed to achieve 85% statistical power and the effect size (mean difference) 95% confidence intervals were computed for each feature from the selected features list using R. Following the analysis, Cohen's effect size was computed for each feature using the statistical parameters obtained from the experiment itself in addition to the power of the experiment[88, 89]. Correlation plot for image-based HCA feature and GAA activity was computed and plotted using corrplot (Wei T, Simko V (2024). *R package 'corrplot': Visualization of a Correlation Matrix*. (Version 0.95), https://github.com/taiyun/corrplot.) The effect size (mean difference) confidence interval plots shown throughout the manuscript were computed using a bootstrap technique by using the dabstr package in R. Additionally, to confirm findings, various statistical tools such as AIC, power analysis, and Bayes factor were employed, and are available upon request. Statistical analysis was guided by [89]. For immunofluorescence experiments, fluorescence intensity in each plate was normalized using the maximal intensity levels to achieve normally distributed features for statistical testing, plates were combined and normalized to HC levels to perform statistical analysis.

Data analysis and statistics script used in this work can be found in the link below, additional scripts are available upon request - https://github.com/Urisprecher

In vivo and ex vivo analyses. Group sample sizes were determined based on the effect sizes of our previously published open field moving distance[52]. These sample sizes were sufficient to provide the acceptable power of at least 80%. To obtain randomization, litters from mice born a few days apart were pooled and pups of similar weight were divided into vehicle-, IM-GHF-201 and ND-GHF-201. Differences in weights over time were tested by One Way ANOVA with repeated measures. Metabolomics analysis to compare groups two-tailed t-tests were performed and raw p values were used to define significant metabolites. For MSEA raw p values were used as well. For Metabolomics visualization of metabolites, s-PLS-DA analysis (based on 2 components) and MSEA analysis and visualization was performed and plotted

using Metaboanalyst 6.0.

Acknowledgements

US – Conceptualization, Data curation, Formal analysis, Investigation, Methodology, Software, Validation, Visualization, Writing - original draft, Writing – review & editing; MG – Conceptualization, Investigation, Methodology, Writing - original draft; SS - Investigation, Methodology; NM - Investigation, Methodology; KM - Investigation, Methodology; PK - Investigation, Methodology; SS - Investigation, Methodology; DE - Investigation, Methodology; OS - Investigation, Methodology, Formal analysis; AE - Investigation, Methodology; AM - Investigation, Methodology; SG – Resources; NG - Resources, Writing – original draft; GB – Resources, Writing – original draft; HM – Resources; GT – Resources, Writing – original draft; HR – Supervision, Writing – original draft; MW – Conceptualization, Funding acquisition, Project administration, Supervision, Writing - original draft, Writing – review & editing; OK – Conceptualization, Formal analysis, Funding acquisition, Project administration, Supervision, Writing
- original draft, Writing – review & editing. We thank Dr. Yuval Dor from the Hebrew University Faculty of Medicine for assistance with mouse pancreatic islets isolation. We thank Dr. Nina Raben from the NIH for kindly providing us with the PD modeling *Gaa*$^{-/-}$ mice. This work was funded by grant 0004934 to OK from the Israel Ministry of Science and Technology and by The Krigsner Family Foundation donation for GSD research in MW Laboratory, Tel Aviv University. The PhD scholarship of US was partly supported by The Yoran Institute of Genome Research and Personalized Medicine, by The Tel Aviv University Prajs-Drimmer Institute for Development of Anti-Degenerative Drugs, The Ela Kodesz Institute for Research on Cancer Development and Prevention, Cancer Biology Research Center and The Dan Moran foundation.

References

(1) Haque, M. E.; Akther, M.; Azam, S.; Kim, I. S.; Lin, Y.; Lee, Y. H.; Choi, D. K. Targeting α-synuclein aggregation and its role in mitochondrial dysfunction in Parkinson's disease. *Br J Pharmacol* **2022**, *179* (1), 23-45. DOI: 10.1111/bph.15684.

(2) Snedden, A. M.; Kellett, K. A. B.; Lilleker, J. B.; Hooper, N. M.; Chinoy, H. The role of protein aggregation

in the pathogenesis of inclusion body myositis. *Clin Exp Rheumatol* **2022**, *40* (2), 414-424. DOI: 10.55563/clinexprheumatol/pp0oso.

(3) Riba, M.; Augé, E.; Tena, I.; Del Valle, J.; Molina-Porcel, L.; Ximelis, T.; Vilaplana, J.; Pelegrí, C. Corpora Amylacea in the Human Brain Exhibit Neoepitopes of a Carbohydrate Nature. *Front Immunol* **2021**, *12*, 618193. DOI: 10.3389/fimmu.2021.618193.

(4) Buchan, J. R.; Kolaitis, R. M.; Taylor, J. P.; Parker, R. Eukaryotic stress granules are cleared by autophagy and Cdc48/VCP function. *Cell* **2013**, *153* (7), 1461-1474. DOI: 10.1016/j.cell.2013.05.037.

(5) Riba, M.; Augé, E.; Campo-Sabariz, J.; Moral-Anter, D.; Molina-Porcel, L.; Ximelis, T.; Ferrer, R.; Martín-Venegas, R.; Pelegrí, C.; Vilaplana, J. act as containers that remove waste products from the brain. *Proc Natl Acad Sci U S A* **2019**, *116* (51), 26038-26048. DOI: 10.1073/pnas.1913741116.

(6) Colburn, R.; Lapidus, D. An analysis of Pompe newborn screening data: a new prevalence at birth, insight and discussion. *Front Pediatr* **2023**, *11*, 1221140. DOI: 10.3389/fped.2023.1221140.

(7) Lim, J. A.; Kakhlon, O.; Li, L.; Myerowitz, R.; Raben, N. Pompe disease: Shared and unshared features of lysosomal storage disorders. *Rare Dis* **2015**, *3* (1), e1068978. DOI: 10.1080/21675511.2015.1068978.

(8) Do, H.; Meena, N. K.; Raben, N. Failure of Autophagy in Pompe Disease. *Biomolecules* **2024**, *14* (5). DOI: 10.3390/biom14050573.

(9) Chien, Y. H.; Tsai, W. H.; Chang, C. L.; Chiu, P. C.; Chou, Y. Y.; Tsai, F. J.; Wong, S. L.; Lee, N. C.; Hwu, W. L. Earlier and higher dosing of alglucosidase alfa improve outcomes in patients with infantile-onset Pompe disease: Evidence from real-world experiences. *Mol Genet Metab Rep* **2020**, *23*, 100591. DOI: 10.1016/j.ymgmr.2020.100591.

(10) Lee, N. C.; Hwu, W. L.; Muramatsu, S. I.; Falk, D. J.; Byrne, B. J.; Cheng, C. H.; Shih, N. C.; Chang, K. L.; Tsai, L. K.; Chien, Y. H. A Neuron-Specific Gene Therapy Relieves Motor Deficits in Pompe Disease Mice. *Mol Neurobiol* **2018**, *55* (6), 5299-5309. DOI: 10.1007/s12035-017-0763-4.

(11) Fukuda, T.; Ahearn, M.; Roberts, A.; Mattaliano, R. J.; Zaal, K.; Ralston, E.; Plotz, P. H.; Raben, N. Autophagy and mistargeting of therapeutic enzyme in skeletal muscle in Pompe disease. *Mol Ther* **2006**, *14* (6), 831-839. DOI: 10.1016/j.ymthe.2006.08.009.

(12) Nascimbeni, A. C.; Fanin, M.; Masiero, E.; Angelini, C.; Sandri, M. Impaired autophagy contributes to muscle atrophy in glycogen storage disease type II patients. *Autophagy* **2012**, *8* (11), 1697-1700. DOI: 10.4161/auto.21691.

(13) Li, S.; Sun, B.; Nilsson, M. I.; Bird, A.; Tarnopolsky, M. A.; Thurberg, B. L.; Bali, D.; Koeberl, D. D. Adjunctive β2-agonists reverse neuromuscular involvement in murine Pompe disease. *FASEB J* **2013**, *27* (1), 34-44. DOI: 10.1096/fj.12-207472.

(14) Kishnani, P. S.; Sun, B.; Koeberl, D. D. Gene therapy for glycogen storage diseases. *Hum Mol Genet* **2019**, *28* (R1), R31-R41. DOI: 10.1093/hmg/ddz133.

(15) Han, S. O.; Li, S.; McCall, A.; Arnson, B.; Everitt, J. I.; Zhang, H.; Young, S. P.; ElMallah, M. K.; Koeberl, D. D. Comparisons of Infant and Adult Mice Reveal Age Effects for Liver Depot Gene Therapy in Pompe Disease. *Mol Ther Methods Clin Dev* **2020**, *17*, 133-142. DOI: 10.1016/j.omtm.2019.11.020.

(16) Brommel, C. M.; Cooney, A. L.; Sinn, P. L. Adeno-Associated Virus-Based Gene Therapy for Lifelong Correction of Genetic Disease. *Hum Gene Ther* **2020**, *31* (17-18), 985-995. DOI: 10.1089/hum.2020.138.

(17) Autio, M. I.; Motakis, E.; Perrin, A.; Bin Amin, T.; Tiang, Z.; Do, D. V.; Wang, J.; Tan, J.; Ding, S. S. L.; Tan, W. X.; et al. Computationally defined and in vitro validated putative genomic safe harbour loci for transgene expression in human cells. *Elife* **2024**, *13*. DOI: 10.7554/eLife.79592.

(18) Aznauryan, E.; Yermanos, A.; Kinzina, E.; Devaux, A.; Kapetanovic, E.; Milanova, D.; Church, G. M.; Reddy, S. T. Discovery and validation of human genomic safe harbor sites for gene and cell therapies. *Cell Rep Methods* **2022**, *2* (1), 100154. DOI: 10.1016/j.crmeth.2021.100154.

(19) Tang, B.; Frasinyuk, M. S.; Chikwana, V. M.; Mahalingan, K. K.; Morgan, C. A.; Segvich, D. M.;

Bondarenko, S. P.; Mrug, G. P.; Wyrebek, P.; Watt, D. S.; et al. Discovery and Development of Small- Molecule Inhibitors of Glycogen Synthase. *J Med Chem* **2020**, *63* (7), 3538-3551. DOI: 10.1021/acs.jmedchem.9b01851.

(20) Ullman, J. C.; Mellem, K. T.; Xi, Y.; Ramanan, V.; Merritt, H.; Choy, R.; Gujral, T.; Young, L. E. A.; Blake, K.; Tep, S.; et al. Small-molecule inhibition of glycogen synthase 1 for the treatment of Pompe disease and other glycogen storage disorders. *Sci Transl Med* **2024**, *16* (730), eadf1691. DOI: 10.1126/scitranslmed.adf1691.

(21) Gaspar, R. C.; Sakuma, I.; Nasiri, A.; Hubbard, B. T.; LaMoia, T. E.; Leitner, B. P.; Tep, S.; Xi, Y.; Green, E. M.; Ullman, J. C.; et al. Small molecule inhibition of glycogen synthase I reduces muscle glycogen content and improves biomarkers in a mouse model of Pompe disease. *Am J Physiol Endocrinol Metab* **2024**, *327* (4), E524-E532. DOI: 10.1152/ajpendo.00175.2024.

(22) Ullman, J. C.; Dick, R. A.; Linzner, D.; Minga, T.; Tep, S.; Satterfield, T. F.; Xi, Y.; Beattie, D. T.; Marmon, T.; Neutel, J. M.; et al. First-in-Human Evaluation of Safety, Pharmacokinetics and Muscle Glycogen Lowering of a Novel Glycogen Synthase 1 Inhibitor for the Treatment of Pompe Disease. *Clin Pharmacol Ther* **2024**, *116* (6), 1580-1592. DOI: 10.1002/cpt.3470.

(23) Kakhlon, O.; Vaknin, H.; Mishra, K.; D'Souza, J.; Marisat, M.; Sprecher, U.; Wald-Altman, S.; Dukhovny, A.; Raviv, Y.; Da'adoosh, B.; et al. Alleviation of a polyglucosan storage disorder by enhancement of autophagic glycogen catabolism. *EMBO Mol Med* **2021**, e14554. DOI: 10.15252/emmm.202114554.

(24) Eskelinen, E. L.; Schmidt, C. K.; Neu, S.; Willenborg, M.; Fuertes, G.; Salvador, N.; Tanaka, Y.; Lüllmann-Rauch, R.; Hartmann, D.; Heeren, J.; et al. Disturbed cholesterol traffic but normal proteolytic function in LAMP-1/LAMP-2 double-deficient fibroblasts. *Mol Biol Cell* **2004**, *15* (7), 3132-3145. DOI: 10.1091/mbc.e04-02-0103.

(25) Eskelinen, E. L. Roles of LAMP-1 and LAMP-2 in lysosome biogenesis and autophagy. *Mol Aspects Med* **2006**, *27* (5-6), 495-502. DOI: 10.1016/j.mam.2006.08.005.

(26) Handy, J.; Macintosh, G. C.; Jenny, A. Ups and downs of lysosomal pH: conflicting roles of LAMP proteins? *Autophagy* **2024**, *20* (2), 437-440. DOI: 10.1080/15548627.2023.2274253.

(27) Zhang, J.; Zeng, W.; Han, Y.; Lee, W. R.; Liou, J.; Jiang, Y. Lysosomal LAMP proteins regulate lysosomal pH by direct inhibition of the TMEM175 channel. *Mol Cell* **2023**, *83* (14), 2524-2539.e2527. DOI: 10.1016/j.molcel.2023.06.004.

(28) Oughtred, R.; Rust, J.; Chang, C.; Breitkreutz, B. J.; Stark, C.; Willems, A.; Boucher, L.; Leung, G.; Kolas, N.; Zhang, F.; et al. The BioGRID database: A comprehensive biomedical resource of curated protein, genetic, and chemical interactions. *Protein Sci* **2021**, *30* (1), 187-200. DOI: 10.1002/pro.3978.

(29) Zhang, X.; Wang, L.; Ireland, S. C.; Ahat, E.; Li, J.; Bekier, M. E.; Zhang, Z.; Wang, Y. GORASP2/GRASP55 collaborates with the PtdIns3K UVRAG complex to facilitate autophagosome-lysosome fusion. *Autophagy* **2019**, *15* (10), 1787-1800. DOI: 10.1080/15548627.2019.1596480.

(30) Mishra, K.; Sweetat, S.; Baraghithy, S.; Sprecher, U.; Marisat, M.; Bastu, S.; Glickstein, H.; Tam, J.; Rosenmann, H.; Weil, M.; et al. The Autophagic Activator GHF-201 Can Alleviate Pathology in a Mouse Model and in Patient Fibroblasts of Type III Glycogenosis. *Biomolecules* **2024**, *14* (8). DOI: 10.3390/biom14080893.

(31) Sprecher, U.; D'Souza , J.; Mishra , K.; Canella Miliano , A.; Mithieux , G.; Rajas , F.; Avraham , S.; Anikster , Y.; Kakhlon , O.; Weil, M. Disease-associated programming of cell memory in glycogen storage disorder type 1a. BioRXiv:2024; Vol. chrome-extension://efaidnbmnnnibpcajpcglclefindmkaj/https://www.biorxiv.org/content/10.1101/2023.02.20.529109v2.full.pdf.

(32) Hirano, M.; Weil, M.; Kakhlon, O.; Mordechai, A.; Garti, N.; Gilgun-Sherki, Y.; Lossos, A. <p class="MsoNormal" style="margin-bottom:3.0pt;text-align:justify;line-height:

12.0pt;mso-line-height-rule:exactly"> A Phase 2/3 Adaptive Design Study of GHF-201 as the First Potential

Treatment in Adult Polyglucosan Body Disease. To be presented as a poster at the Annual Meeting of the

American Academy of Neurology, Chicago 2026: 2026.

(33) Sprecher, U.; Dsouza, J.; Marisat, M.; Barasch, D.; Mishra, K.; Kakhlon, O.; Manor, J.; Anikster, Y.; Weil, M. In depth profiling of dihydrolipoamide dehydrogenase deficiency in primary patients fibroblasts reveals metabolic reprogramming secondary to mitochondrial dysfunction. *Mol Genet Metab Rep* **2025**, *42*, 101172. DOI: 10.1016/j.ymgmr.2024.101172.

(34) Eriksson, I.; Wäster, P.; Öllinger, K. Restoration of lysosomal function after damage is accompanied by recycling of lysosomal membrane proteins. *Cell Death Dis* **2020**, *11* (5), 370. DOI: 10.1038/s41419-020-2527-8.

(35) Moriyama, Y.; Takano, T.; Ohkuma, S. Acridine orange as a fluorescent probe for lysosomal proton pump. *J Biochem* **1982**, *92* (4), 1333-1336. DOI: 10.1093/oxfordjournals.jbchem.a134053.

(36) Blum, G.; von Degenfeld, G.; Merchant, M. J.; Blau, H. M.; Bogyo, M. Noninvasive optical imaging of cysteine protease activity using fluorescently quenched activity-based probes. *Nat Chem Biol* **2007**, *3* (10), 668-677. DOI: 10.1038/nchembio.2007.26.

(37) Bhatia, D.; Chung, K. P.; Nakahira, K.; Patino, E.; Rice, M. C.; Torres, L. K.; Muthukumar, T.; Choi, A. M.; Akchurin, O. M.; Choi, M. E. Mitophagy-dependent macrophage reprogramming protects against kidney fibrosis. *JCI Insight* **2019**, *4* (23). DOI: 10.1172/jci.insight.132826.

(38) Nishiyama, Y.; Shimada, Y.; Yokoi, T.; Kobayashi, H.; Higuchi, T.; Eto, Y.; Ida, H.; Ohashi, T. Akt inactivation induces endoplasmic reticulum stress-independent autophagy in fibroblasts from patients with Pompe disease. *Mol Genet Metab* **2012**, *107* (3), 490-495. DOI: 10.1016/j.ymgme.2012.09.011.

(39) Takikita, S.; Myerowitz, R.; Zaal, K.; Raben, N.; Plotz, P. H. Murine muscle cell models for Pompe disease and their use in studying therapeutic approaches. *Mol Genet Metab* **2009**, *96* (4), 208-217. DOI: 10.1016/j.ymgme.2008.12.012.

(40) Szwed, A.; Kim, E.; Jacinto, E. Regulation and metabolic functions of mTORC1 and mTORC2. *Physiol Rev*

2021, *101* (3), 1371-1426. DOI: 10.1152/physrev.00026.2020.

(41) Pinho, S. A.; Costa, C. F.; Deus, C. M.; Pinho, S. L. C.; Miranda-Santos, I.; Afonso, G.; Bagshaw, O.; Stuart, J. A.; Oliveira, P. J.; Cunha-Oliveira, T. Mitochondrial and metabolic remodelling in human skin fibroblasts in response to glucose availability. *FEBS J* **2022**, *289* (17), 5198-5217. DOI: 10.1111/febs.16413. Pacitti, D.; Levene, M.; Garone, C.; Nirmalananthan, N.; Bax, B. E. Mitochondrial Neurogastrointestinal Encephalomyopathy: Into the Fourth Decade, What We Have Learned So Far. *Front Genet* **2018**, *9*, 669. DOI: 10.3389/fgene.2018.00669.

(42) Filosto, M.; Cotti Piccinelli, S.; Caria, F.; Gallo Cassarino, S.; Baldelli, E.; Galvagni, A.; Volonghi, I.; Scarpelli, M.; Padovani, A. Mitochondrial Neurogastrointestinal Encephalomyopathy (MNGIE-MTDPS1). *J Clin Med* **2018**, *7* (11). DOI: 10.3390/jcm7110389.

(43) Benard, G.; Rossignol, R. Ultrastructure of the mitochondrion and its bearing on function and bioenergetics. *Antioxid Redox Signal* **2008**, *10* (8), 1313-1342. DOI: 10.1089/ars.2007.2000.

(44) Massalha, W.; Markovits, M.; Pichinuk, E.; Feinstein-Rotkopf, Y.; Tarshish, M.; Mishra, K.; Llado, V.; Weil, M.; Escriba, P. V.; Kakhlon, O. Minerval (2-hydroxyoleic acid) causes cancer cell selective toxicity by uncoupling oxidative phosphorylation and compromising bioenergetic compensation capacity. *Biosci Rep* **2019**, *39* (1). DOI: 10.1042/BSR20181661.

(45) Memme, J. M.; Erlich, A. T.; Phukan, G.; Hood, D. A. Exercise and mitochondrial health. *J Physiol* **2021**, *599* (3), 803-817. DOI: 10.1113/JP278853.

(46) Hagl, S.; Kocher, A.; Schiborr, C.; Eckert, S. H.; Ciobanu, I.; Birringer, M.; El-Askary, H.; Helal, A.; Khayyal, M. T.; Frank, J.; et al. Rice bran extract protects from mitochondrial dysfunction in guinea pig brains. *Pharmacol Res* **2013**, *76*, 17-27. DOI: 10.1016/j.phrs.2013.06.008.

(47) Lagalice, L.; Pichon, J.; Gougeon, E.; Soussi, S.; Deniaud, J.; Ledevin, M.; Maurier, V.; Leroux, I.; Durand, S.; Ciron, C.; et al. Satellite cells fail to contribute to muscle repair but are functional in Pompe disease

(glycogenosis type II). *Acta Neuropathol Commun* **2018**, *6* (1), 116. DOI: 10.1186/s40478-018-0609-y.

(48) Ashcroft, F. M.; Rohm, M.; Clark, A.; Brereton, M. F. Is Type 2 Diabetes a Glycogen Storage Disease of Pancreatic β Cells? *Cell Metab* **2017**, *26* (1), 17-23. DOI: 10.1016/j.cmet.2017.05.014.

(49) Lim, J. A.; Li, L.; Kakhlon, O.; Myerowitz, R.; Raben, N. Defects in calcium homeostasis and mitochondria can be reversed in Pompe disease. *Autophagy* **2015**, *11* (2), 385-402. DOI: 10.1080/15548627.2015.1009779.

(50) Li, M.; Khambu, B.; Zhang, H.; Kang, J. H.; Chen, X.; Chen, D.; Vollmer, L.; Liu, P. Q.; Vogt, A.; Yin, X. M. Suppression of lysosome function induces autophagy via a feedback down-regulation of MTOR complex 1 (MTORC1) activity. *J Biol Chem* **2013**, *288* (50), 35769-35780. DOI: 10.1074/jbc.M113.511212.

(51) Raben, N.; Schreiner, C.; Baum, R.; Takikita, S.; Xu, S.; Xie, T.; Myerowitz, R.; Komatsu, M.; Van der Meulen, J. H.; Nagaraju, K.; et al. Suppression of autophagy permits successful enzyme replacement therapy in a lysosomal storage disorder--murine Pompe disease. *Autophagy* **2010**, *6* (8), 1078-1089. DOI: 10.4161/auto.6.8.13378.

(52) Lim, J. A.; Li, L.; Shirihai, O. S.; Trudeau, K. M.; Puertollano, R.; Raben, N. Modulation of mTOR signaling as a strategy for the treatment of Pompe disease. *EMBO Mol Med* **2017**, *9* (3), 353-370. DOI: 10.15252/emmm.201606547.

(53) Kakhlon, O.; Vaknin, H.; Mishra, K.; D'Souza, J.; Marisat, M.; Sprecher, U.; Wald-Altman, S.; Dukhovny, A.; Raviv, Y.; Da'adoosh, B.; et al. Alleviation of a polyglucosan storage disorder by enhancement of autophagic glycogen catabolism. *EMBO Mol Med* **2021**, *13* (10), e14554. DOI: 10.15252/emmm.202114554.

(54) Raben, N.; Wong, A.; Ralston, E.; Myerowitz, R. Autophagy and mitochondria in Pompe disease: nothing is so new as what has long been forgotten. *Am J Med Genet C Semin Med Genet* **2012**, *160C* (1), 13-21. DOI: 10.1002/ajmg.c.31317.

(55) Cramer, A. A. W.; Prasad, V.; Eftestøl, E.; Song, T.; Hansson, K. A.; Dugdale, H. F.; Sadayappan, S.; Ochala, J.; Gundersen, K.; Millay, D. P. Nuclear numbers in syncytial muscle fibers promote size but limit the development of larger myonuclear domains. *Nat Commun* **2020**, *11* (1), 6287. DOI: 10.1038/s41467-020-20058-7.

(56) Kakhlon, O.; Ferreira, I.; Solmesky, L. J.; Khazanov, N.; Lossos, A.; Alvarez, R.; Yetil, D.; Pampou, S.; Weil, M.; Senderowitz, H.; et al. Guaiacol as a drug candidate for treating adult polyglucosan body disease. *JCI Insight* **2018**, *3* (17). DOI: 10.1172/jci.insight.99694.

(57) Young, L. E. A.; Conroy, L. R.; Clarke, H. A.; Hawkinson, T. R.; Bolton, K. E.; Sanders, W. C.; Chang, J. E.; Webb, M. B.; Alilain, W. J.; Vander Kooi, C. W.; et al. In situ mass spectrometry imaging reveals heterogeneous glycogen stores in human normal and cancerous tissues. *EMBO Mol Med* **2022**, *14* (11), e16029. DOI: 10.15252/emmm.202216029.

(58) Corkey, B. E.; Deeney, J. T.; Merrins, M. J. What Regulates Basal Insulin Secretion and Causes Hyperinsulinemia? *Diabetes* **2021**, *70* (10), 2174-2182. DOI: 10.2337/dbi21-0009.

(59) Kaufman, B. A.; Li, C.; Soleimanpour, S. A. Mitochondrial regulation of β-cell function: maintaining the momentum for insulin release. *Mol Aspects Med* **2015**, *42*, 91-104. DOI: 10.1016/j.mam.2015.01.004.

(60) Gao, Z. Y.; Li, G.; Najafi, H.; Wolf, B. A.; Matschinsky, F. M. Glucose regulation of glutaminolysis and its role in insulin secretion. *Diabetes* **1999**, *48* (8), 1535-1542. DOI: 10.2337/diabetes.48.8.1535.

(61) Deepa Maheshvare, M.; Raha, S.; König, M.; Pal, D. A pathway model of glucose-stimulated insulin secretion in the pancreatic. *Front Endocrinol (Lausanne)* **2023**, *14*, 1185656. DOI: 10.3389/fendo.2023.1185656.

(62) Zhang, G. F.; Jensen, M. V.; Gray, S. M.; El, K.; Wang, Y.; Lu, D.; Becker, T. C.; Campbell, J. E.; Newgard, C. B. Reductive TCA cycle metabolism fuels glutamine- and glucose-stimulated insulin secretion. *Cell Metab* **2021**, *33* (4), 804-817.e805. DOI: 10.1016/j.cmet.2020.11.020.

(63) Raben, N.; Nagaraju, K.; Lee, E.; Kessler, P.; Byrne, B.; Lee, L.; LaMarca, M.; King, C.; Ward, J.; Sauer, B.; et al. Targeted disruption of the acid alpha-glucosidase gene in mice causes an illness with critical features of both infantile and adult human glycogen storage disease type II. *J Biol Chem* **1998**, *273* (30), 19086-19092.

(64) Peng, S. S.; Hwu, W. L.; Lee, N. C.; Tsai, F. J.; Tsai, W. H.; Chien, Y. H. Slow, progressive myopathy in neonatally treated patients with infantile-onset Pompe disease: a muscle magnetic resonance imaging study. *Orphanet J Rare Dis* **2016**, *11* (1), 63. DOI: 10.1186/s13023-016-0446-7.

(65) Cohen, J. L.; Chakraborty, P.; Fung-Kee-Fung, K.; Schwab, M. E.; Bali, D.; Young, S. P.; Gelb, M. H.; Khaledi, H.; DiBattista, A.; Smallshaw, S.; et al. In Utero Enzyme-Replacement Therapy for Infantile-OnsetPompe's Disease. *N Engl J Med* **2022**, *387* (23), 2150-2158. DOI: 10.1056/NEJMoa2200587.

(66) Nilsson, M. I.; MacNeil, L. G.; Kitaoka, Y.; Suri, R.; Young, S. P.; Kaczor, J. J.; Nates, N. J.; Ansari, M. U.; Wong, T.; Ahktar, M.; et al. Combined aerobic exercise and enzyme replacement therapy rejuvenates the mitochondrial-lysosomal axis and alleviates autophagic blockage in Pompe disease. *Free Radic Biol Med* **2015**, *87*, 98-112. DOI: 10.1016/j.freeradbiomed.2015.05.019.

(67) Zhu, M.; Zhang, S.; Tian, X.; Wu, C. Mask mitigates MAPT- and FUS-induced degeneration by enhancing autophagy through lysosomal acidification. *Autophagy* **2017**, 1-15. DOI: 10.1080/15548627.2017.1362524.

(68) Spampanato, C.; Feeney, E.; Li, L.; Cardone, M.; Lim, J. A.; Annunziata, F.; Zare, H.; Polishchuk, R.; Puertollano, R.; Parenti, G.; et al. Transcription factor EB (TFEB) is a new therapeutic target for Pompe disease. *EMBO Mol Med* **2013**, *5* (5), 691-706. DOI: 10.1002/emmm.201202176.

(69) Medina, D. L.; Fraldi, A.; Bouche, V.; Annunziata, F.; Mansueto, G.; Spampanato, C.; Puri, C.; Pignata, A.; Martina, J. A.; Sardiello, M.; et al. Transcriptional activation of lysosomal exocytosis promotes cellular clearance. *Dev Cell* **2011**, *21* (3), 421-430. DOI: 10.1016/j.devcel.2011.07.016.

(70) Derissen, E. J.; Beijnen, J. H.; Schellens, J. H. Concise drug review: azacitidine and decitabine. *Oncologist* **2013**, *18* (5), 619-624. DOI: 10.1634/theoncologist.2012-0465.

(71) Eckschlager, T.; Plch, J.; Stiborova, M.; Hrabeta, J. Histone Deacetylase Inhibitors as Anticancer Drugs. *Int J Mol Sci* **2017**, *18* (7). DOI: 10.3390/ijms18071414.

(72) Roger, A. L.; Sethi, R.; Huston, M. L.; Scarrow, E.; Bao-Dai, J.; Lai, E.; Biswas, D. D.; El Haddad, L.; Strickland, L. M.; Kishnani, P. S.; et al. What's new and what's next for gene therapy in Pompe disease? *Expert Opin Biol Ther* **2022**, 1-19. DOI: 10.1080/14712598.2022.2067476.

(73) Deus, C. M.; Pereira, S. P.; Cunha-Oliveira, T.; Pereira, F. B.; Raimundo, N.; Oliveira, P. J. Mitochondrial remodeling in human skin fibroblasts from sporadic male Parkinson's disease patients uncovers metabolic and mitochondrial bioenergetic defects. *Biochim Biophys Acta Mol Basis Dis* **2020**, *1866* (3), 165615. DOI: 10.1016/j.bbadis.2019.165615.

(74) Punetha, M.; Saini, S.; Chaudhary, S.; Bala, R.; Sharma, M.; Kumar, P.; Kumar, D.; Yadav, P. S. Mitochondria-targeted antioxidant MitoQ ameliorates ROS production and improves cell viability in cryopreserved buffalo fibroblasts. *Tissue Cell* **2023**, *82*, 102067. DOI: 10.1016/j.tice.2023.102067.

(75) Stillman, J. M.; Mendes Lopes, F.; Lin, J. P.; Hu, K.; Reich, D. S.; Schafer, D. P. Lipofuscin-like autofluorescence within microglia and its impact on studying microglial engulfment. *Nat Commun* **2023**, *14* (1), 7060. DOI: 10.1038/s41467-023-42809-y.

(76) Al Rijjal, D.; Wheeler, M. B. A protocol for studying glucose homeostasis and islet function in mice. *STAR Protoc* **2022**, *3* (1), 101171. DOI: 10.1016/j.xpro.2022.101171.

(77) Caicedo, J. C.; Cooper, S.; Heigwer, F.; Warchal, S.; Qiu, P.; Molnar, C.; Vasilevich, A. S.; Barry, J. D.; Bansal, H. S.; Kraus, O.; et al. Data-analysis strategies for image-based cell profiling. *Nat Methods* **2017**, *14* (9), 849-863. DOI: 10.1038/nmeth.4397.

(78) Wang, Y.; LêCao, K. A. Managing batch effects in microbiome data. *Brief Bioinform* **2020**, *21* (6), 1954-

1970. DOI: 10.1093/bib/bbz105.

(79) Hoffman, G. E.; Schadt, E. E. variancePartition: interpreting drivers of variation in complex gene expression studies. *BMC Bioinformatics* **2016**, *17* (1), 483. DOI: 10.1186/s12859-016-1323-z.

(80) Gharaba, S.; Sprecher, U.; Baransi, A.; Muchtar, N.; Weil, M. Characterization of fission and fusion mitochondrial dynamics in HD fibroblasts according to patient's severity status. *Neurobiol Dis* **2024**, *201*, 106667. DOI: 10.1016/j.nbd.2024.106667.

(81) Breunig, M. M.; Kriegel, H.-P.; Ng, R. T.; Sander, J. $L_{OF:\ identifying\ density\text{-}based\ local\ outliers}$. *ACM Sigmund Record* **2000**, *29* (2), 93-104.

(82) Pedregosa, F. Scikit-learn: Machine Learning in Python. 2012.

(83) Yépez, V. A.; Kremer, L. S.; Iuso, A.; Gusic, M.; Kopajtich, R.; Koňaříková, E.; Nadel, A.; Wachutka, L.; Prokisch, H.; Gagneur, J. OCR-Stats: Robust estimation and statistical testing of mitochondrial respiration activities using Seahorse XF Analyzer. *PLoS One* **2018**, *13* (7), e0199938. DOI: 10.1371/journal.pone.0199938.

(84) Benetsky, R. The p -Value Requires Context, Not a Threshold. *Am Stat* **2019**, *73*, 115-117.

(85) Lazic, S. E.; Clarke-Williams, C. J.; Munafò, M. R. What exactly is 'N' in cell culture and animal experiments? *PLoS Biol* **2018**, *16* (4), e2005282. DOI: 10.1371/journal.pbio.2005282.

(86) pwr-package: Basic Functions for Power Analysis pwr in pwr: Basic Functions for Power Analysis.

(87) Champely, S. pwr: Basic functions for power analysis. Preprint at https://nyuscholars.nyu.edu/en/publications/pwr-basic-functions-for-power-analysis 2017.

(88) Halsey, L. G. The reign of the p-value is over: what alternative analyses could we employ to fill the power vacuum? *Biol Lett* **2019**, *15* (5), 20190174. DOI: 10.1098/rsbl.2019.0174.

Declaration of Interests

The authors claim that they don't have any conflict of interest.

OK and MW also serve as consultants to GHF, Golden Heart Flower Ltd. All IP rights in the invention of GHF-201 described in this manuscript were licensed to GHF. OK and MW are also the holders of patent US11891381B2 "Compounds for the treatment of glycogen storage disorders" which includes GHF-201.

Table 1 - Primary human skin fibroblasts

Cell ID	**Cell type**	**Origin**	**Age**	**Gender**
GM05400	HC	Coriell	6Y	male
GM05565	HC	Coriell	3Y	male
GM00038	HC	Coriell	9Y	female
MNGIE-5250	MNGIE	Sheba Medical Center	5Y	male
AV-9915	GFER	Sheba Medical Center	5Y	male

143	HC	Coriell	42Y	male
498	HC	Coriell	3Y	male

848	HC	Coriell	48y	female
657	IOPD	Rambam Medical Center	7Y	male
654	IOPD	Rambam Medical Center	1 month	female
648	IOPD	Rambam Medical Center	8 months	male
640	LOPD	Rambam Medical Center	5Y	female
596	LOPD	Rambam Medical Center	6Y	female
412	LOPD	Rambam Medical Center	3 months	male
434	IOPD	Rambam Medical Center	6M	male
440	IOPD	Rambam Medical Center	5M	female
595	IOPD	Rambam Medical Center	2Y	male
969	HC	Coriell	2Y	female
8429	HC	Coriell	1 Day	male

4431	HC	Coriell	15 weeks	female

Table 2 – Primers

Gene primer	Primer sequence
B2M forward	5'TGCTGTCTCCATGTTTGATGTATCT'3
B2M reverse	5'TCTCTGCTCCCCACCTCTAAGT'3
MT-TL1 forward	5'CACCCAAGAACAGGGTTTGT'3
MT-TL1 reverse	5'TGGCCATGGGTATGTTGTTA'3

Figure Legends

Figure 1. High content analysis of IOPD and LOPD primary skin fibroblasts.

(A) Representative HCA images of nucleus (Hoechst 33342), cytoplasm (Calcein), active mitochondria (Tmre), and lysosomes (Lysotracker) in HC, IOPD and LOPD cells. The HCA experiment included cell samples from 4 HC, 6 IOPD and 3 LOPD. **(B)** Principal Component Analysis (PCA) plot, showing HC (blue gradient), IOPD (red gradient), and LOPD (green gradient) wells grouped by their average values from the 24, 48, and 72 h conditions. **(C)** Heatmap showing HC, IOPD, and LOPD wells grouped by their average values from the 24, 48, and 72 h conditions. The heatmap shows area, fluorescence intensity and texture features for cytoplasm, lysosomes, nucleus and active mitochondria. Each column presents z-score normalized average values in each time condition for each group (yellow-high values, purple-low values). **(D)** Linear Discriminant Analysis (LDA) plot, showing HC (blue), IOPD (red), and LOPD (green) wells combined from the 24, 48, and 72 h conditions.)For both C and D, N represents wells and are as follows: HC;24h-10,48h-10,72h-12.IOPD;24h-40,48h-32,72h-21,LOPD;24h-10,48h-15,72h-14 **(E)** Bar plots

representing the top ten contributing features to the variance explained by LD1 (top) and LD2 (bottom). **(F)** GAA activity levels in HC, IOPD, and LOPD fibroblasts tested in regular media conditions, values are normalized to HC (N represent cell samples analyzed, HC=5, IOPD=6, LOPD=3, paired two tailed t-tests were used and Benjamini–Hochberg false discovery rate was applied to generate FDR-adjusted *p*-values). HC-Healthy Control, IOPD-Infantile Onset Pompe Disease, LOPD-Late Onset Pompe Disease.

Figure 2. GHF201 modulates glycogen, autophagic flux and lysosomal morphology in PD fibroblasts.

(A) Left panel- Representative images of GHF-201 treated and untreated Pompe fibroblasts, fluorescently stained for glycogen by the PAS assay. DAPI was used to stain nuclei (blue). Cell mask staining for cytoplasm (yellow) and PAS glycogen staining (magenta). Right panel- Bar Scatter plots with standard error mean, showing fluorescence-based quantification of glycogen staining intensity, comparing DMSO (red) and GHF-201 treated (light red) Pompe fibroblasts under 24h with regular media, (N represent wells of Pompe cells (3 IOPD and 3 LOPD) that were tested in the experiment, two tailed t-tests were used to generate p values). **(B)** Left- Representative immunoblots from a western blot analysis showing autophagic flux in one representative HC sample and one representative Pompe sample (IOPD), determined by the extent of lysosomal inhibitor (Vinblastine)-dependent increase in the ratio of lipidated to non-lipidated LC3 ratio (LC3-ii/LC3-i). Autophagic flux was calculated by dividing the ratio of LC3-ii/LC3-I with vinblastine to the ratio of LC3-ii/LC3-I without vinblastine for each sample. Right- Densitometric quantifications scatter plots comparing HC (blue), HC+GHF201(light blue), Pompe (red) and Pompe+GHF201(pink) fibroblasts under 24h with starvation media. Actin levels are shown and were used to normalize loading protein content of samples, (N represent samples analyzed, HC=3, HC+GHF201=3, Pompe=4 (2 IOPD and 2 LOPD), Pompe+GHF201=4, (2 IOPD and 2 LOPD), paired two tailed t-tests were used and Benjamini–Hochberg false discovery rate was applied to generate FDR-adjusted *p*-values). **(C)** Left- Bootstrap Confidence interval plot showing lysotracker deep red fluorescence intensity levels in HC (blue), HC+GHF201(light blue), HC+LLOME (very light blue), IOPD (red), IOPD+GHF201(light red), IOPD+LLOME (very light red), LOPD (green), LOPD+GHF201(light green), LOPD+LLOME (very light green) after 24h with starvation media. Values are normalized to logarithmic scale. Upper panel shows scatter plots with 95% confidence intervals around the mean values per group (lines next to scatter dots), lower

panel shows bootstrap mediated confidence interval for the mean difference of each group compared to HC (distribution plots). (N represent wells from 5 HC, 6 IOPD and 3 LOPD samples, two tailed t-tests were used to generate p values). Right-Representative images of the Lysotracker experiment, Hoechst 33442 (blue), Calcein (green), Lysotracker deep red (red) in HC, HC+GHF201, HC+LLOME, IOPD, IOPD+GHF201, IOPD+LLOME, LOPD, LOPD+GHF201 and LOPD+LLOME cells. HC- Healthy Control, IOPD-Infantile Onset Pompe Disease, LOPD-Late Onset Pompe Disease.

Figure 3. GHF201 modulates lysosomal function in PD fibroblasts.

(A) Left- Bootstrap Confidence interval plot showing Acridine Orange green to red fluorescence intensity levels in HC (blue), HC+GHF201(light blue), HC+LLOME (very light blue), IOPD (red), IOPD+GHF201(light red), IOPD+LLOME (very light red), LOPD (green), LOPD+GHF201(light green), LOPD+LLOME (very light green) after 24h with starvation media, values are normalized to logarithmic scale. Upper panel shows scatter plots with 95% confidence intervals around the mean values per group (lines next to scatter dots), lower panel shows bootstrap mediated confidence interval for the mean difference of each group compared to HC (distribution plots). (N represent wells from 5 HC, 6 IOPD and 3 LOPD samples, unpaired two tailed t-tests were used and Benjamini–Hochberg false discovery rate was applied to generate FDR-adjusted *p*-values). Right- Representative images of the Acridine Orange experiment in HC, HC+GHF201, HC+LLOME, IOPD, IOPD+GHF201, IOPD+LLOME, LOPD, LOPD+GHF201 and LOPD+LLOME cells. **(B)** Left- Bootstrap Confidence interval plot showing GB123 fluorescence intensity levels in HC (blue), HC+GHF201(light blue), IOPD (red), IOPD+GHF201(light red), LOPD(green), and LOPD+GHF201(light green)) after 24h with starvation media, values are normalized to logarithmic scale. Upper panel shows scatter plots with 95% confidence intervals around the mean values per group (lines next to scatter dots), lower panel shows bootstrap mediated confidence interval for the mean difference of each group compared to HC (distribution plots). (N represent wells from 5 HC, 6 IOPD and 3 LOPD samples, unpaired two tailed t-tests were used and Benjamini–Hochberg false discovery rate was applied to generate FDR-adjusted *p*-values). Right- Representative images of the GB123 experiment, Hoechst 33442 (blue), Calcein (yellow), GB123 (red) in HC, HC+GHF201, IOPD, IOPD+GHF201, LOPD and LOPD+GHF201 cells. **(C)** From left to right- Scatter plots with standard error mean, showing Immunofluorescence-based quantification of P62, PINK,

TFEB, and LAMP1, PGC1alpha comparing HC (blue), HC+GHF201(light blue), IOPD (red), IOPD+GHF201(light red), LOPD (green), and LOPD+GHF201(light green) after 24h with starvation media, values are normalized to logarithmic scale. (N represent wells from 5 HC, 6 IOPD and 3 LOPD samples, unpaired two tailed t-tests were used and Benjamini–Hochberg false discovery rate was applied to generate FDR-adjusted *p*-values). HC- Healthy Control, IOPD-Infantile Onset Pompe Disease, LOPD-Late Onset Pompe Disease.

Figure 4. GHF201 modulates the bioenergetic profile of PD fibroblasts.

(A) Representative quantification of Seahorse real-time cellular oxygen consumption rates (OCR) of HC (blue), HC+GHF201(light blue), IOPD (red), IOPD+GHF201(light red), LOPD (green), LOPD+GHF201(light green), GFER (orange) and MNGIE (mustard) fibroblasts over time, following 24h with starvation media. Dashed lines indicate the addition of mitochondrial inhibitors (Oligomycin; FCCP; Antimycin A/Rotenone) for assessment of mitochondrial respiration. **(B)** Bootstrap Confidence interval plot showing OCR-derived parameters (basal respiration, maximal respiration, ATP production and proton leak) in HC(blue), HC+GHF201(light blue), IOPD(red), IOPD+GHF201(light red), LOPD(green), and LOPD+GHF201(light green), GFER(orange) and MNGIE(mustard) fibroblasts. Upper panel shows scatter plots with 95% confidence intervals around the mean values per group (lines next to scatter dots), lower panel shows bootstrap mediated confidence interval for the mean difference of each group compared to HC (distribution plots). (N represent wells from 5 HC, 6 IOPD and 3 LOPD samples, unpaired two tailed t-tests were used and Benjamini–Hochberg false discovery rate was applied to generate FDR-adjusted *p*-values). HC- Healthy Control, IOPD-Infantile Onset Pompe Disease, LOPD-Late Onset Pompe Disease.

Figure 5. Mitochondrial membrane potential and ROS production in PD fibroblasts

(A) Left- Bootstrap Confidence interval plot showing Mitochondrial membrane potential (MMP) determined by TMRE staining in HC (blue), HC+GHF201(light blue), IOPD (red), IOPD+GHF201(light red), LOPD (green), and LOPD+GHF201(light green), HC+High Galactose(orange) and HC+MitoQ(mustard) fibroblasts, following 24h with starvation media. Upper panel shows scatter plots with 95% confidence intervals around the mean values per group (lines next to scatter dots), lower panel shows bootstrap

mediated confidence interval for the mean difference of each group compared to HC (distribution plots). (N represent wells from 5 HC, 6 IOPD and 3 LOPD samples, unpaired two tailed t-tests were used and Benjamini–Hochberg false discovery rate was applied to generate FDR-adjusted *p*-values). Right- Representative images of the TMRE experiment in HC, HC+GHF201, IOPD, IOPD+GHF201, LOPD, LOPD+GHF201, HC+ High Galactose and HC+MitoQ cells. **(B)** Left-- Bootstrap Confidence interval plot showing Mitochondrial ROS production determined by the MitoSOX staining in HC (blue), HC+GHF201(light blue), IOPD (red), IOPD+GHF201(light red), LOPD (green), and LOPD+GHF201(light green) fibroblasts, following 24h with starvation media. Upper panel shows scatter plots with 95% confidence intervals around the mean values per group (lines next to scatter dots), lower panel shows bootstrap mediated confidence interval for the mean difference of each group compared to HC (distribution plots). (N represent wells from 5 HC, 6 IOPD and 3 LOPD samples, unpaired two tailed t-tests were used and Benjamini–Hochberg false discovery rate was applied to generate FDR-adjusted *p*-values). Right- Representative images of the MitoSOX experiment in HC, HC+GHF201, IOPD, IOPD+GHF201, LOPD and LOPD+GHF201 cells. **(C)** Bar plots showing nuclear DNA-normalized mitochondrial DNA fold change compared to HC for HC(blue), HC+GHF201(light blue), IOPD(red), IOPD+GHF201 (pink), LOPD (green), and LOPD+GHF201 (light green), GFER (orange) and MNGIE (mustard) fibroblasts, following 24h with starvation media. (N represent samples, unpaired two tailed t-tests were used and Benjamini–Hochberg false discovery rate was applied to generate FDR-adjusted *p*-values based on CT values of the tested groups.). HC- Healthy Control, IOPD-Infantile Onset Pompe Disease, LOPD-Late Onset Pompe Disease.

Figure 6. Pharmacokinetics and efficacy of a tailored oral nanodroplet (ND) formulation of GHF201 in PD modeling Gaa-/- mice.

(A) Pharmacokinetics of ND-GHF201. *Left panel, Gaa*$^{-/-}$ mice were pipetted *per os* with 70 mg/kg ND-GHF201 and then euthanized 30, 60, 120, and 240 min post administration. The indicated tissues were removed, as well as 200 uL of serum drawn. Graph shows means (± SEM) of GHF201 levels in the different tissues determined by LC-MS/MS. Results obtained from n= 3 mice at each time point. *Right panel,* GHF201 in 5% DMSO was injected to the leg muscle and levels in muscle were determined as in the *Left panel*. **(B)** Transmission profiling of GHF-201 loaded on NDs. The samples (loaded and empty) were centrifuged at 3000 rpm for 17 hours in horizontal tubes and 180 sources of light were shined on them in

the Lumisizer instrument. The green straight line **(Ba & Bb)** indicates full light transmission and no change in the entire horizontal tube. The implication of this result is that ND-GHF-201 is physically stable for at least three years at RT. We have also run HPLC-based chemical stability tests (not shown) showing that ND-GHF-201 had the acceptable <0.6wt% impurities level. **(Bc)** ND-GHF-201 size distribution. 100% of ND-GHF-201 showed the expected size of the nanodroplets. **(C)** GHF201 safety and effect on muscle glycogen. *Left panel,* Mouse weight over time in the strains and treatment indicated. No significant differences in the change in weight over time were observed between the different strains and treatments (N=8 animals per group, One Way ANOVA with Repeated Measures). *Middle panel, $Gaa^{+/+}$* and *$Gaa^{-/-}$* mice (n=4 in each group) were treated daily for 5 months *per os* with either nanodroplet formulated GHF201 (70 mg/kg) or unloaded nanodroplet (empty ND). Other *$Gaa^{+/+}$* and *$Gaa^{-/-}$* mice were injected twice a week intramuscularly (IM) with either GHF201 (250 mg/kg), or 5% DMSO solvent as a control. Post euthanasia, *gastrocnemius* muscle was collected and subjected to Periodic Acid Schiff's reagent (PAS) staining for glycogen. *Right panel*, Glycogen levels determined biochemically in the same groups (n=3 mice per group). Statistical differences and FDR-adjusted p values were determined by two tailed t-tests.

Figure 7. GHF201 modulates the bioenergetic profile of muscles and pancreatic islets derived from Gaa$^{-/-}$ mice.

Ex vivo bioenergetic analysis. Bioenergetic profiling using Seahorse's mito-stress kit for determining real-time cellular oxygen consumption rates (OCR) of myotubes **(A)** and pancreatic islets (**B**, 5 per well) isolated from the indicated strains and treatments (n=6 of each group). Vertical arrows indicate the addition of mitochondrial inhibitors (oligomycin; FCCP; antimycin A/rotenone, as in Fig. 4) for the assessment of derived mitochondrial respiration parameters (basal OCR, maximal OCR, coupling efficiency and spare respiratory capacity) quantified in the panels shown below the bioenergetic profiles. Plots show means (± SEM). Indicated FDR-adjusted p values were determined by two-sided t-tests.

Figure 8. GHF201's effect on autophagy and oxidative stress in myotubes and muscle fibers derived for Gaa-/-mice.

GHF201's effect on autophagy and ROS production in myotubes and muscle fibers. **(A)** EDL muscle myofibers were isolated from n=4 mice of each of the strains and treatments groups indicated. Isolated

myofibers were fixed and stained with the LC3 antibody, followed by the Alexafluor 488 secondary antibody (see Fig. S5 for representative figures). Shown here are image quantifications. **(B)** WB of the mTORC1-downstream signaling pair phosphorylated and total S6. Protein was extracted from EDL myofibers from n=3 mice from each group and subjected to WB analysis. Results of densitometric quantification of the phosphor-S6/S6 ratio are shown to the left and a representative WB to the right. **(C)** Quantifications of confocal microscope images of myotubes and myofibers derived from n=4 mice of the strains and treatments indicated. Samples were stained with the oxidative stress indicator CellROX. The significant reduction in CellROX staining indicates inhibition of ROS production rate. See Fig. S6 for representative images. **(D)** Quantification of lipofuscin autofluorescence (LAF) at 561 nm only in single GC myofibers derived from n=3 mice from each group. See Fig. S6C for representative images. FDR-adjusted p values in **(A)-(D)** were determined by two-sided t-tests.

Figure 9. GHF201's effect on myotube differentiation and myofibers nuclear count in *Gaa*$^{-/-}$ mice.

(A) Satellite cells from gastrocnemius myofibers isolated from the strains and treatments indicated (n=3 per group) were differentiated to myoblasts and then to myotube syncytia according to an accepted protocol (Spampanato et al (2013) EMBO Mol Med 5: 619). Cells were imaged at 15 days post initiation of differentiation by bright-field (*upper panel*) and immunofluorescence with antibody against the myological differentiation biomarker, the transcription factor MEF2C (red, nuclei in blue). *Lower panel*, MEF2C quantification and significant differences between treated and untreated conditions. **(B)** *Upper panel*, GHF-201 effects on nuclei count in syncytial myofibers. Myofibers were isolated from the strains and treatments indicated and stained with H&E. *Lower panel*, Per-myofiber nuclei count quantification. n=6 per group, Shown are means (± SEM). FDR-adjusted p values determined by two-sided t-tests.

Figure 10. GHF201 and guaiacol effect on insulin secretion and plasma metabolomics.

Compounds effect on insulin secretion and serum metabolomics. **(A)** Pancreatic islets were isolated from the strains and treatment groups indicated (n=6 animals per group) and basal (*left panel*) and glucose-stimulated (*right panel*) insulin secretion was determined as described in Methods. **(B)** Partial Least-Squares Discriminant Analysis (PLS-DA) of all metabolites analyzed showing a clear separation among all groups with guaiacol treated animals more different than untreated animals as compared to GHF-201

treated animals. **(C-D)** Variables Importance in Projection (VIP) curve of metabolites significantly contributing to the classification of GHF-201 **(C)**, or Guaiacol **(D)** and untreated animals as separate groups. **(E)** Metabolite sets significantly enriched by the GHF-201 treatment. **(F)** Changes in Asp, Glu, and malate – metabolites statistically determining the enrichment and increase of the malate-aspartate shuttle in **(E).** **(G)** Metabolic sets significantly enriched by the Guaiacol treatment. Guaiacol compared to untreated animals **(H)** Changes in dihydroxyacetone phosphate, glycerol-3-phosphate and glycerate – metabolites statistically determining the enrichment and increase of glycolysis in **G**.

Figure 11. GHF201 effects on motor parameters and on survival in Gaa-/- mice.

GHF201 effects on motor parameters and on survival. **(A)** Four paws grip strength was determined in n=8 mice from each group treated as indicated from the age of 3 months for 4 months. **(B)** Open field distance was determined in the same mice. Significant differences (p-values) between treated and untreated mice were determined by two-sided t-tests **(C)** Kalpan-Meier survival curve of *Gaa*$^{-/-}$ mice showing survival up to 270 days post GHF201 treatment initiation (n=8) is fully restored as compared to untreated (Vehicle) *Gaa*$^{-/-}$ mice (n=8) ($p< 0.08$, Log-rank test; Hazard Ratio = 0.13).

Figure S1

(A) Bar plots representing the top ten contributing features to the variance explained by PC2 (top) and PC1 (bottom) for the PCA plot shown in Figure 1B. (B) Cell count results of HC and IOPD fibroblasts following 24 h and 48 h starvation and following 48 h starvation succeeded by 24 h glucose replenishment (72 h). **(C)** Bootstrap Confidence Interval plots showing the indicated HCA features from the 24h time condition comparing wells of HC (blue), IOPD (red), and LOPD (green) fibroblasts. Values are normalized to logarithmic scale. Upper panel shows scatter plots with 95% confidence intervals around the mean values per group (lines next to scatter dots), lower panel shows bootstrap mediated confidence interval for the mean difference of each group compared to HC (distribution plots). N represent wells from 4 HC, 6 IOPD and 3 LOPD samples. Unpaired two tailed t-tests were used and Benjamini–Hochberg false discovery rate was applied to generate FDR-adjusted *p*-values. The HCA experiment included cell samples from 4 HC, 6 IOPD and 3 LOPD.

Figure S2

(A) Box plots of the indicated HCA features from the 24h time condition comparing HC (blue), IOPD (red), and LOPD (green) fibroblasts, values are normalized to logarithmic scale. N represent patients. Unpaired two tailed t-tests were used and Benjamini–Hochberg false discovery rate was applied to generate FDR-adjusted *p*-values. **(B)** Correlation plot of HCA features and GAA activity observed between the IOPD, LOPD and HC samples. The numerical values of the correlation coefficients are indicated and also shown by the size of the sectors and blue to red intensity. Correlations between GAA activity and other features are highlighted. Features were z-scored scaled and correlation was computed using Pearson coefficient. The HCA experiment included cell samples from 4 HC, 6 IOPD and 3 LOPD.

Figure S3

Representative immunofluorescence images of LAMP1, Pink, P62, and TFEB (green) comparing HC, HC+GHF201, IOPD, IOPD+GHF201, LOPD and LOPD+GHF201 following 24h with starvation media. Hoechst was used to label nuclei (blue); Phallo (Phalloidin) was used to label actin cytoskeleton showing cell borders (yellow). The immunofluorescence experiments included cell samples from 5 HC, 6 IOPD and 3 LOPD.

Figure S4

(A) Up- Western blot analysis of different ETC proteins indicated (from top to bottom- ATP5A1, UQCRC2, MTCO1, SDHB) and comparing HC, HC+GHF201, IOPD, IOPD+GHF201, LOPD and LOPD+GHF201 following 24h with starvation media. Actin was used as a loading control. The heatmap below the representative blot shows relative quantities of the indicated proteins comparing the different groups (yellow-high values, purple-low values). **(B)** Raw RT-PCR calibration results for the determination of nuclear DNA-normalized mitochondrial DNA as shown in Figure 5D. Shown from right to left are melt curves, standard curve and amplification plots. For RT-PCR calibration was performed on 1 HC, 1 IOPD and 1 LOPD samples, Western Blot analysis was performed on cell samples from 5 HC, 6 IOPD and 3 LOPD.

Figure S5

Representative images of sagittal **(A)** and transverse **(B)** sections of *Gastrocnemius* muscle fibers from *Gaa*$^{+/+}$ and *Gaa*$^{-/-}$ mice treated as indicated and stained for glycogen by PAS. Arrows, examples of high PAS staining showing glycogen over-accumulation. **(C)** EDL muscle myofibers were isolated from mice of each of the strains and treatments groups indicated. Isolated myofibers were fixed and stained with the LC3 antibody, followed by the Alexafluor 488 secondary antibody. Shown are representative images. Scale bar, 50 µm. **(D)** Extracts from EDL muscle myofibers were subjected to SDS-PAGE followed by Western immunoblotting with antibodies against p62 and LC3 as indicated. Beta actin was probed as a loading control. The levels of p62 and LC3-II were determined by densitometry and are plotted below the representative immunoblots. N=3 per group. Two-sided t-tests were used for statistical tests and FDR-adjusted p-values are reported.

Figure S6

Representative confocal microscope images of myotubes **(A)** and myofibers **(B)** derived from the strains and treatments indicated. Samples were stained with the oxidative stress indicator CellROX. The significant reduction in CellROX staining indicates inhibition of ROS production rate. **(C)** Single *Gastrocnemius* myofibers were used to determine Lipofuscin-like Autofluorescence (LAF). LAF was discriminated from broad-spectrum endogenous fluorescence via multi-spectral overlay. Signals exhibiting co-localization across the 405–638 nm range were classified as non-specific background, while non-overlapping puncta with exclusive emission at 561 nm were identified as LAF. Scale bar, 50 µm.

Figure S7

(A) *Gastrocnemius* muscle from *Gaa*$^{-/-}$ mice treated or not with guaiacol as indicated was collected and subjected to Periodic Acid Schiff's reagent (PAS) staining for glycogen. Quantification (N=4, two-sided t-tests) of differences between means are shown to the right and show no significant difference between treated and untreated. **(B and C)** Heatmaps showing metabolites significantly altered (as determined by t-tests) between untreated and GHF201 **(B)**, or Guaiacol **(C)** treated *Gaa*$^{-/-}$ mice. **(D and E)** Volcano plot showing the metabolites whose levels are significantly different between untreated and GHF-201 **(D)**, or Guaiacol **(E)**treated animals. **(F)** Glycemic status of the indicated treatment groups. No significant difference was observed among the different groups (N=3 per groups, One Way ANOVA).

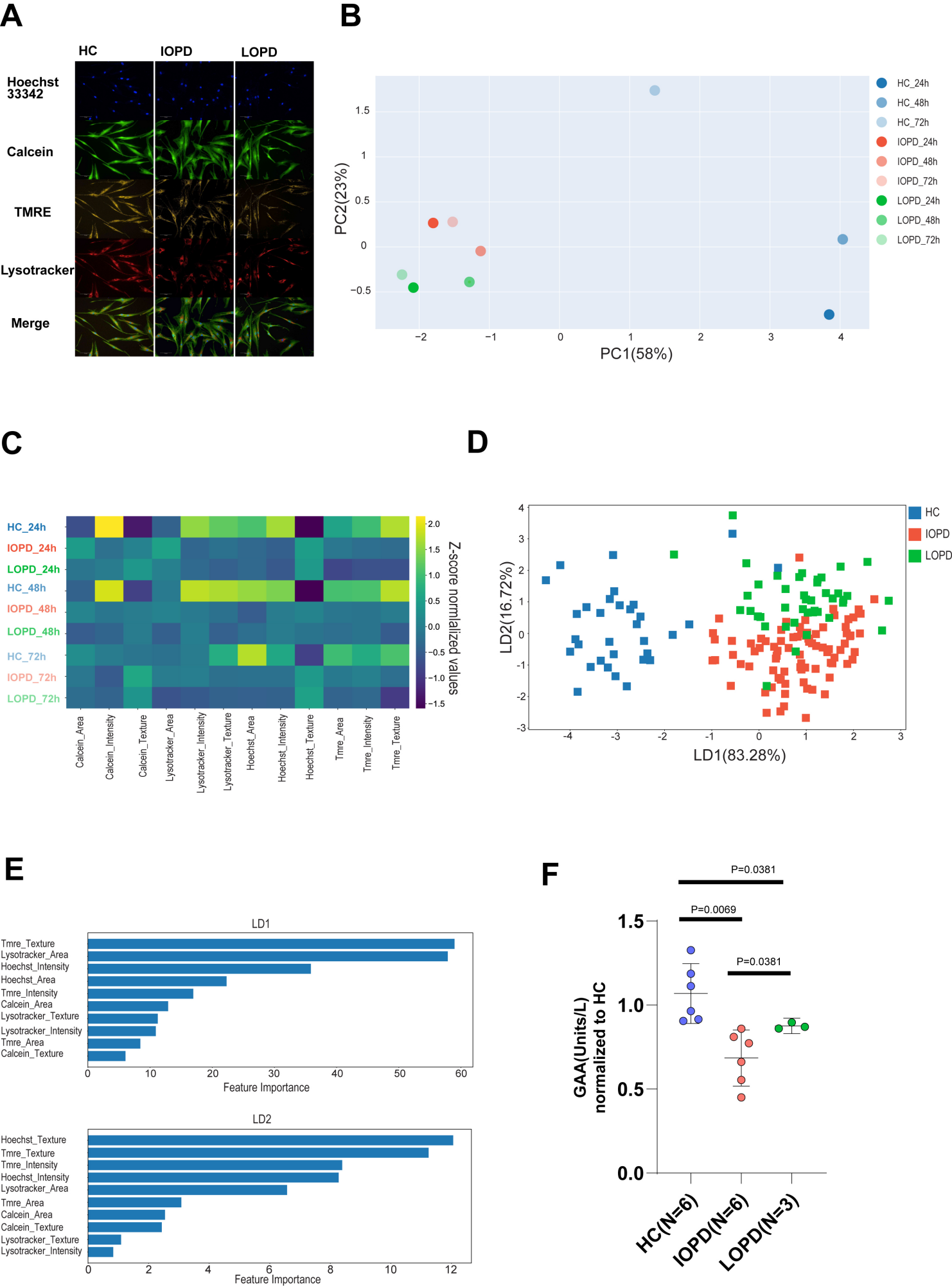
A
HC
IOPD
LOPD
Hoechst 33342
Calcein
TMRE
Lysotracker
Merge
B
PC2(23%)
PC1(58%)
HC_24h
HC_48h
HC_72h
IOPD_24h
IOPD_48h
IOPD_72h
LOPD_24h
LOPD_48h
LOPD_72h
C
HC_24h
IOPD_24h
LOPD_24h
HC_48h
IOPD_48h
LOPD_48h
HC_72h
IOPD_72h
LOPD_72h
Calcein_Area
Calcein_Intensity
Calcein_Texture
Lysotracker_Area
Lysotracker_Intensity
Lysotracker_Texture
Hoechst_Area
Hoechst_Intensity
Hoechst_Texture
Tmre_Area
Tmre_Intensity
Tmre_Texture
Z-score normalized values
D
LD2(16.72%)
LD1(83.28%)
HC
IOPD
LOPD
E
LD1
Tmre_Texture
Lysotracker_Area
Hoechst_Intensity
Hoechst_Area
Tmre_Intensity
Calcein_Area
Lysotracker_Texture
Lysotracker_Intensity
Tmre_Area
Calcein_Texture
Feature Importance
LD2
Hoechst_Texture
Tmre_Texture
Tmre_Intensity
Hoechst_Intensity
Lysotracker_Area
Tmre_Area
Calcein_Area
Calcein_Texture
Lysotracker_Texture
Lysotracker_Intensity
Feature Importance
F
P=0.0381
P=0.0069
P=0.0381
GAA(Units/L) normalized to HC
HC(N=6)
IOPD(N=6)
LOPD(N=3)

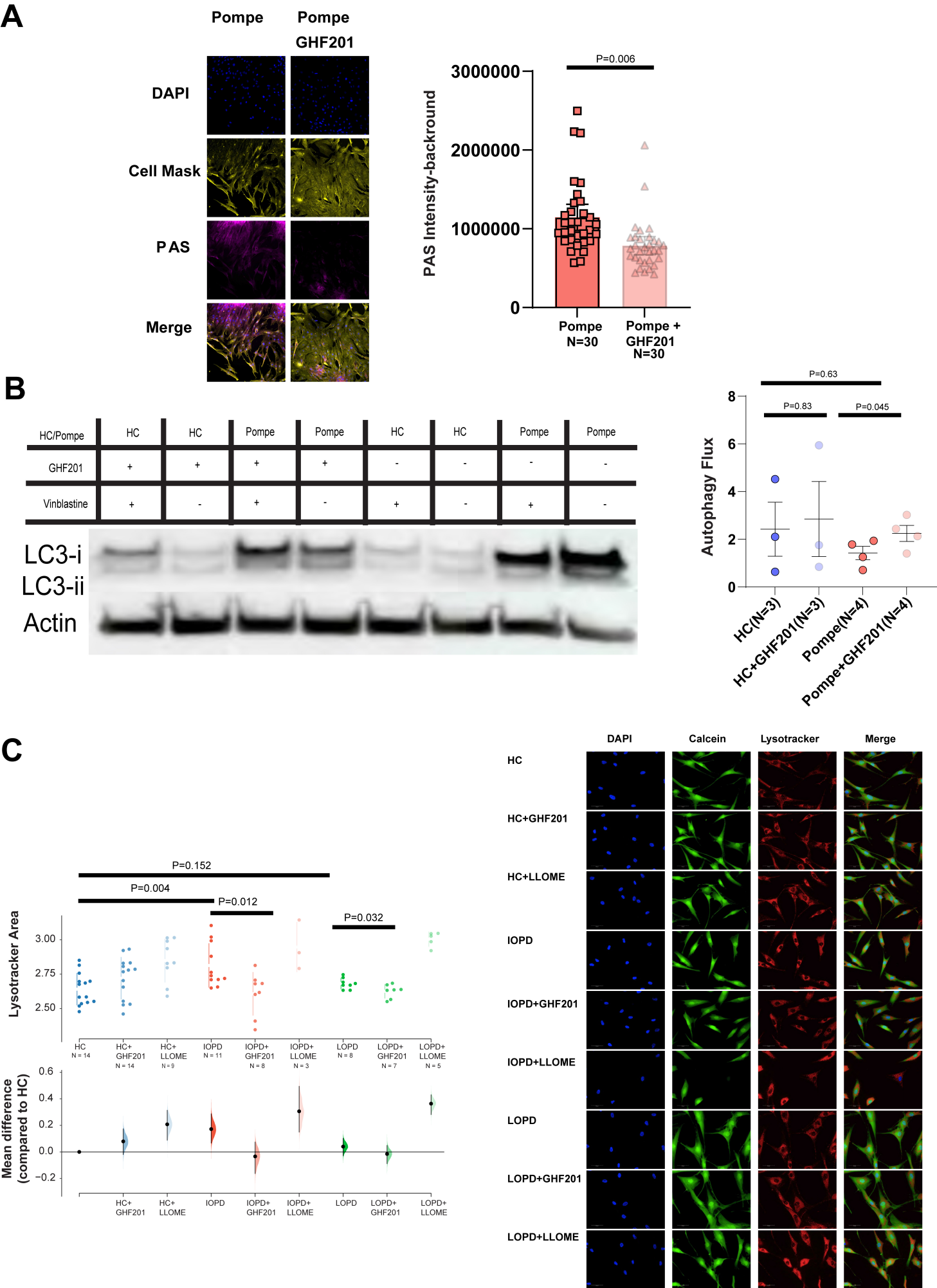
A
Pompe
Pompe GHF201
DAPI
Cell Mask
PAS
Merge
PAS Intensity-backround
3000000
2000000
1000000
0
P=0.006
Pompe N=30
Pompe + GHF201 N=30
B
HC/Pompe
GHF201
Vinblastine
LC3-i
LC3-ii
Actin
Autophagy Flux
P=0.63
P=0.83
P=0.045
HC(N=3)
HC+GHF201(N=3)
Pompe(N=4)
Pompe+GHF201(N=4)
C
P=0.152
P=0.004
P=0.012
P=0.032
Lysotracker Area
Mean difference (compared to HC)
HC
HC+ GHF201
HC+ LLOME
IOPD
IOPD+ GHF201
IOPD+ LLOME
LOPD
LOPD+ GHF201
LOPD+ LLOME
DAPI
Calcein
Lysotracker
Merge
HC
HC+GHF201
HC+LLOME
IOPD
IOPD+GHF201
IOPD+LLOME
LOPD
LOPD+GHF201
LOPD+LLOME

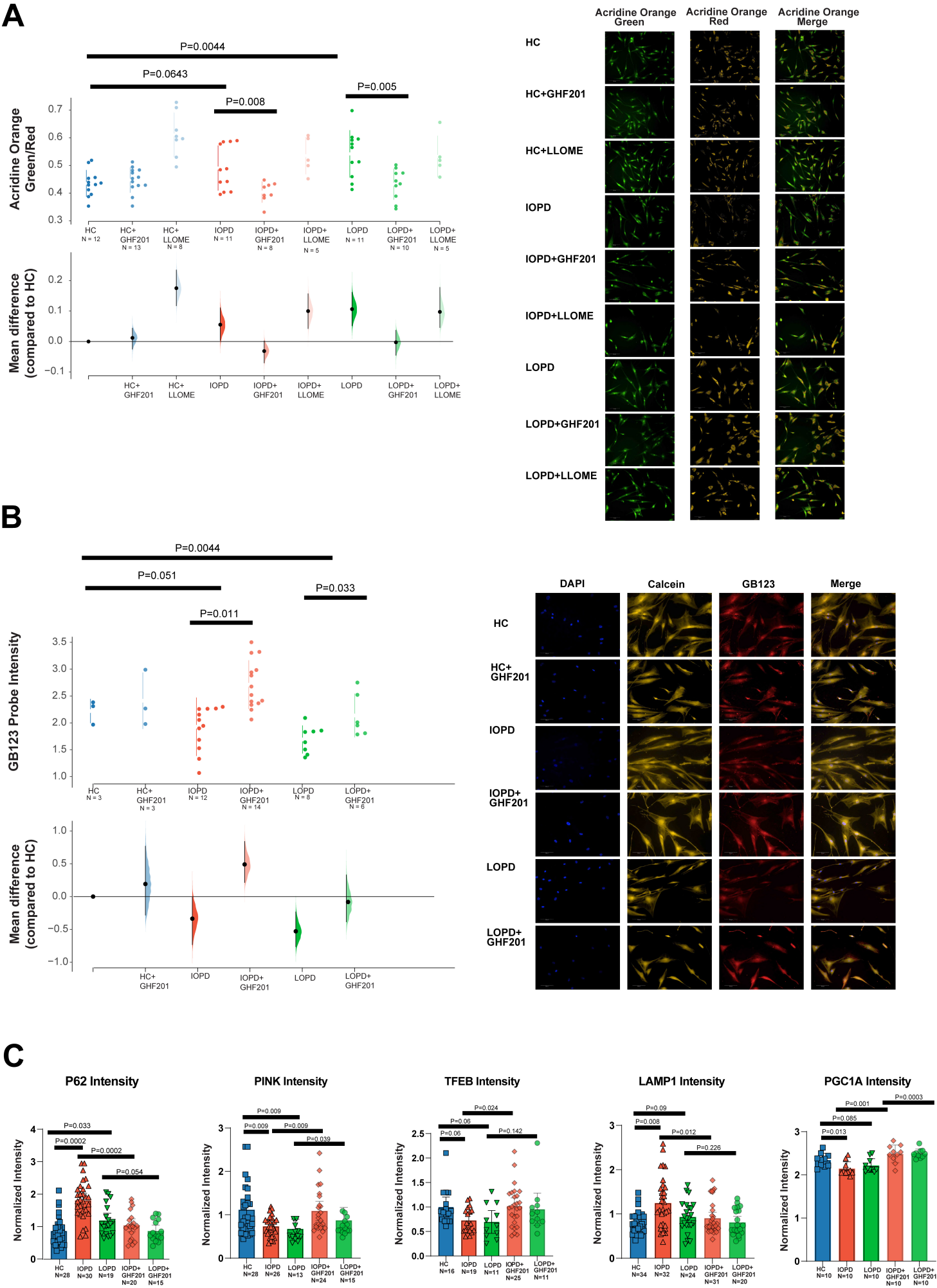
A
P=0.0044
P=0.0643
P=0.008
P=0.005
Acridine Orange Green/Red
HC N = 12
HC+ GHF201 N = 13
HC+ LLOME N = 8
IOPD N = 11
IOPD+ GHF201 N = 8
IOPD+ LLOME N = 5
LOPD N = 11
LOPD+ GHF201 N = 10
LOPD+ LLOME N = 5
Mean difference (compared to HC)
Acridine Orange Green
Acridine Orange Red
Acridine Orange Merge
HC
HC+GHF201
HC+LLOME
IOPD
IOPD+GHF201
IOPD+LLOME
LOPD
LOPD+GHF201
LOPD+LLOME
B
P=0.0044
P=0.051
P=0.033
P=0.011
GB123 Probe Intensity
HC N = 3
HC+ GHF201 N = 3
IOPD N = 12
IOPD+ GHF201 N = 14
LOPD N = 8
LOPD+ GHF201 N = 6
Mean difference (compared to HC)
DAPI
Calcein
GB123
Merge
HC
HC+ GHF201
IOPD
IOPD+ GHF201
LOPD
LOPD+ GHF201
C
P62 Intensity
P=0.033
P=0.0002
P=0.0002
P=0.054
HC N=28
IOPD N=30
LOPD N=19
IOPD+ GHF201 N=20
LOPD+ GHF201 N=15
PINK Intensity
P=0.009
P=0.009
P=0.009
P=0.039
HC N=28
IOPD N=26
LOPD N=13
IOPD+ GHF201 N=24
LOPD+ GHF201 N=15
TFEB Intensity
P=0.024
P=0.06
P=0.06
P=0.142
HC N=16
IOPD N=19
LOPD N=11
IOPD+ GHF201 N=26
LOPD+ GHF201 N=11
LAMP1 Intensity
P=0.09
P=0.008
P=0.012
P=0.226
HC N=34
IOPD N=32
LOPD N=24
IOPD+ GHF201 N=31
LOPD+ GHF201 N=20
PGC1A Intensity
P=0.001
P=0.0003
P=0.085
P=0.013
HC N=10
IOPD N=10
LOPD N=10
IOPD+ GHF201 N=10
LOPD+ GHF201 N=10
Normalized Intensity

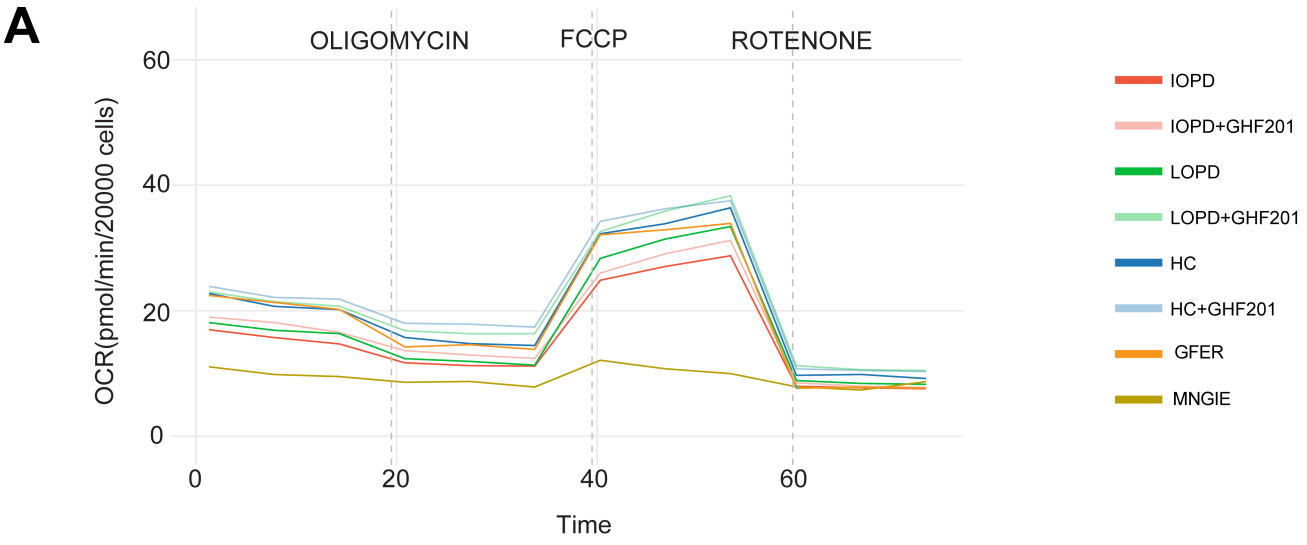
A
OLIGOMYCIN
FCCP
ROTENONE
OCR(pmol/min/20000 cells)
Time
IOPD
IOPD+GHF201
LOPD
LOPD+GHF201
HC
HC+GHF201
GFER
MNGIE

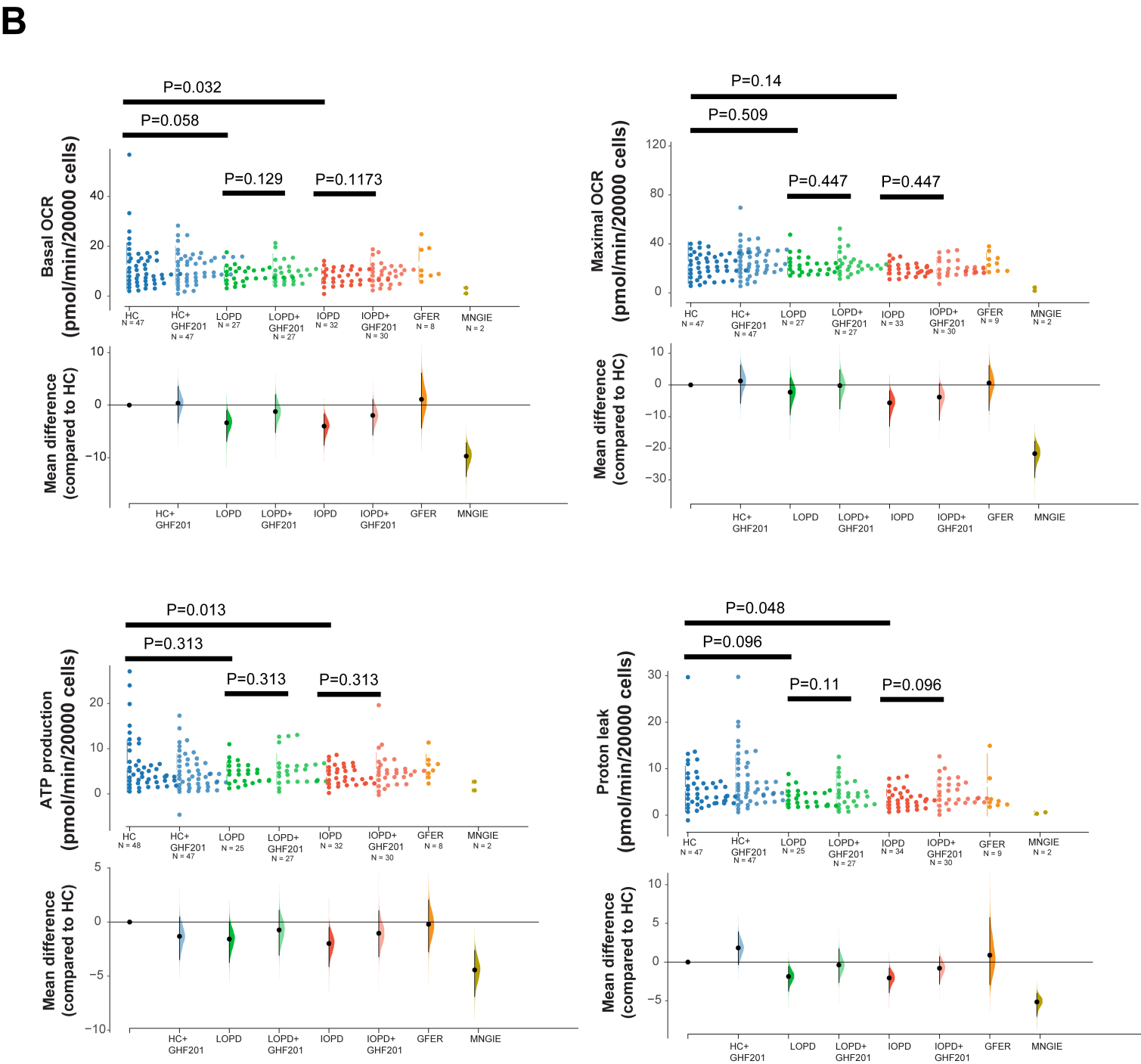
B
P=0.032
P=0.058
P=0.129
P=0.1173
Basal OCR (pmol/min/20000 cells)
Mean difference (compared to HC)
P=0.14
P=0.509
P=0.447
P=0.447
Maximal OCR (pmol/min/20000 cells)
P=0.013
P=0.313
P=0.313
P=0.313
ATP production (pmol/min/20000 cells)
P=0.048
P=0.096
P=0.11
P=0.096
Proton leak (pmol/min/20000 cells)
HC
HC+ GHF201
LOPD
LOPD+ GHF201
IOPD
IOPD+ GHF201
GFER
MNGIE

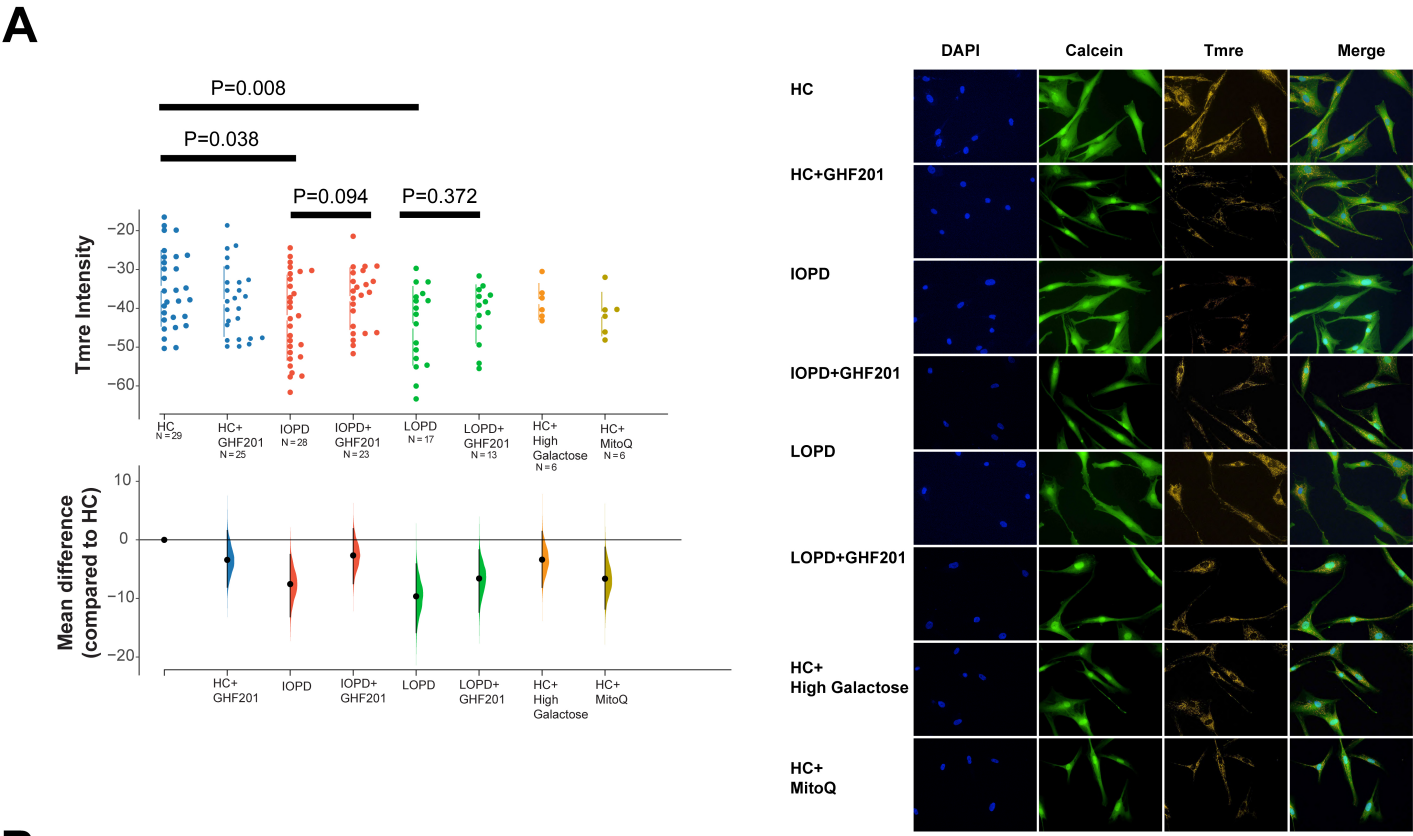
A
P=0.008
P=0.038
P=0.094
P=0.372
Tmre Intensity
HC N=29
HC+ GHF201 N=25
IOPD N=28
IOPD+ GHF201 N=23
LOPD N=17
LOPD+ GHF201 N=13
HC+ High Galactose N=6
HC+ MitoQ N=6
Mean difference (compared to HC)
DAPI
Calcein
Tmre
Merge
HC
HC+GHF201
IOPD
IOPD+GHF201
LOPD
LOPD+GHF201
HC+ High Galactose
HC+ MitoQ

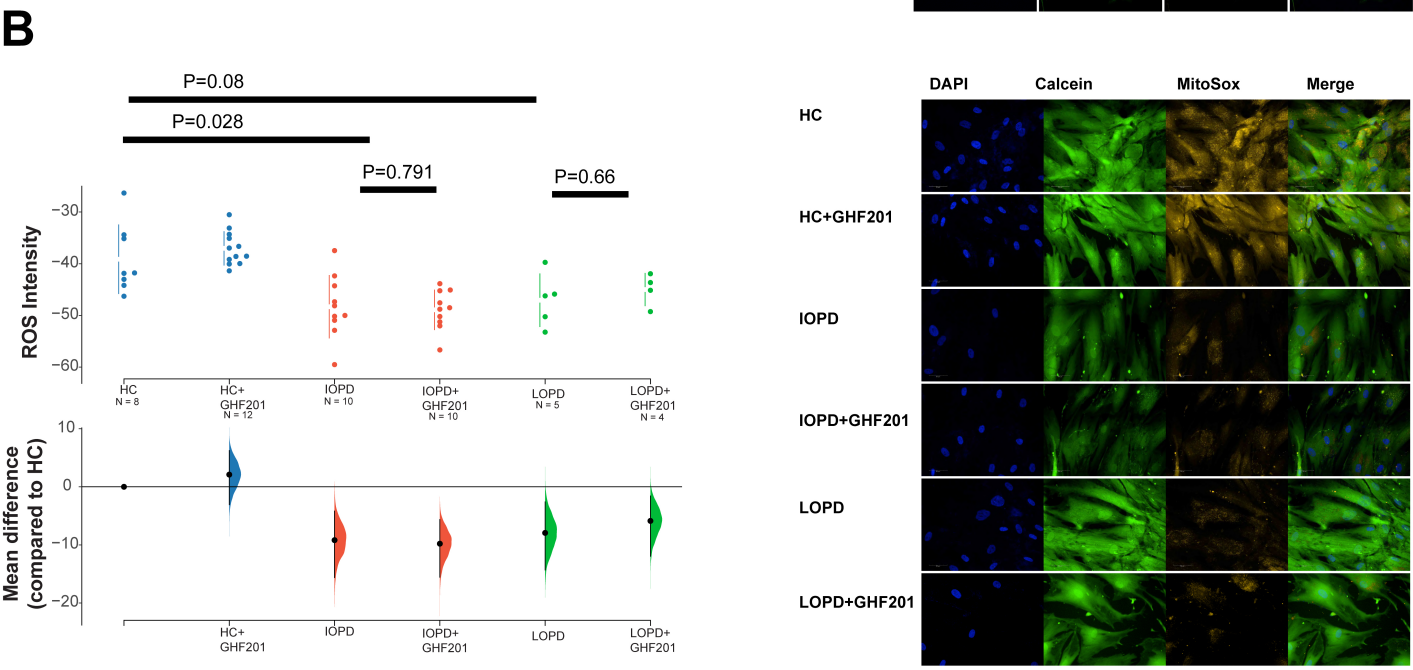
B
P=0.08
P=0.028
P=0.791
P=0.66
ROS Intensity
HC N=8
HC+ GHF201 N=12
IOPD N=10
IOPD+ GHF201 N=10
LOPD N=5
LOPD+ GHF201 N=4
Mean difference (compared to HC)
DAPI
Calcein
MitoSox
Merge
HC
HC+GHF201
IOPD
IOPD+GHF201
LOPD
LOPD+GHF201

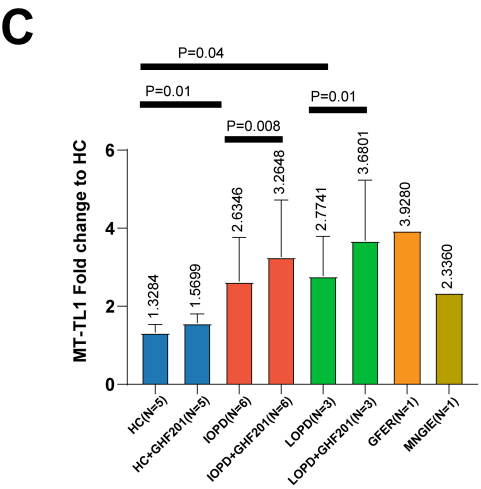
C
P=0.04
P=0.01
P=0.008
P=0.01
MT-TL1 Fold change to HC
1.3284
1.5699
2.6346
3.2648
2.7741
3.6801
3.9280
2.3360
HC(N=5)
HC+GHF201(N=5)
IOPD(N=6)
IOPD+GHF201(N=6)
LOPD(N=3)
LOPD+GHF201(N=3)
GFER(N=1)
MNGIE(N=1)

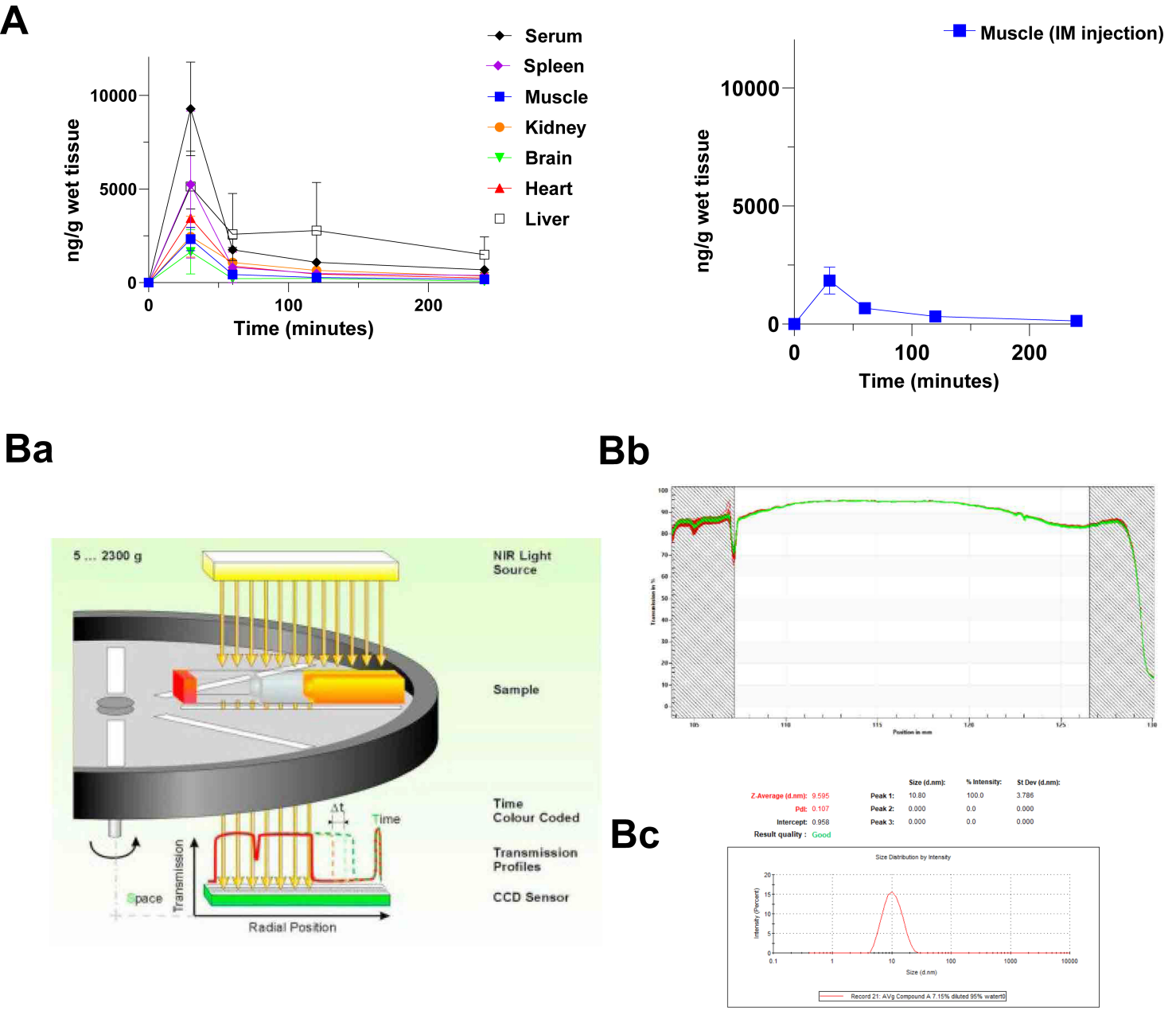
A
Serum
Spleen
Muscle
Kidney
Brain
Heart
Liver
ng/g wet tissue
Time (minutes)
Muscle (IM injection)
Ba
5 ... 2300 g
NIR Light Source
Sample
Time Colour Coded
Transmission Profiles
CCD Sensor
Space
Transmission
Radial Position
Bb
Bc
Size Distribution by Intensity
Record 21: AVg Compound A 7.15% diluted 95% water10
C
Gaa -/-/ND-GHF201(N=8)
Gaa -/-/GHF201 IM(N=8)
Gaa -/-/empty ND(N=8)
Gaa +/+/empty ND(N=8)
Weight (g)
Time after treatment initiation (days)
PAS Intensity
P=0.0004
P=0.001
P<0.0001
P=0.0006
Gaa +/+ /empty ND(N=4)
Gaa +/+/DMSO(N=4)
Gaa -/-/empty ND(N=4)
Gaa -/-/DMSO(N=4)
Gaa -/-/ ND-GHF201(N=4)
Gaa -/-/ IM-GHF201(N=4)
Glycogen Content(umol/mg tissue)
P=0.0004
P=0.0004
P=0.007
P=0.0212
Gaa+/+emptyND (N=3)
Gaa +/+DMSO (N=3)
Gaa-/- empty ND (N=3)
Gaa-/- DMSO (N=3)
Gaa-/-ND-GHF201 (N=3)
Gaa-/-IM-GHF201 (N=3)

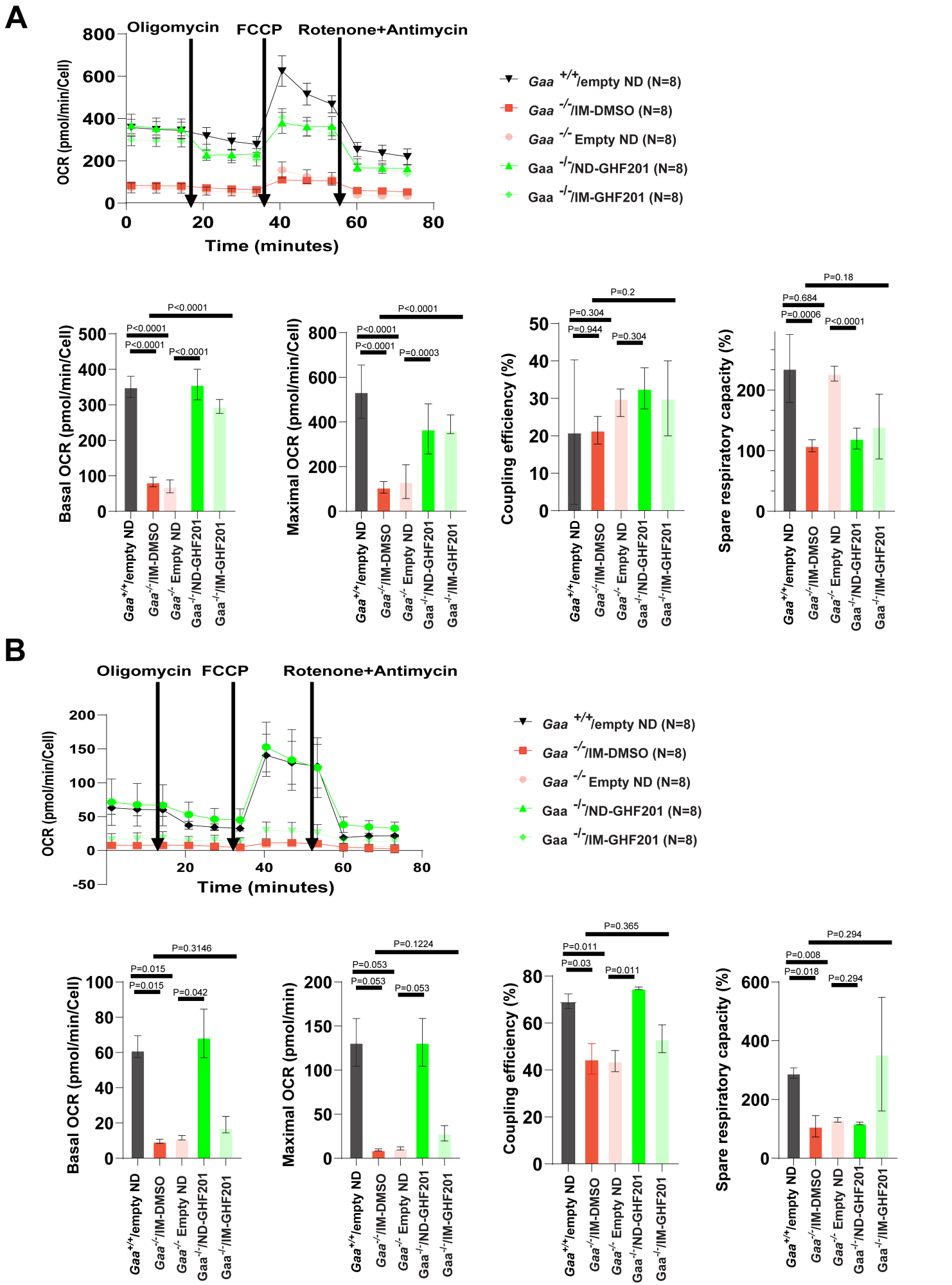
A
Oligomycin
FCCP
Rotenone+Antimycin
OCR (pmol/min/Cell)
Time (minutes)
Gaa +/+/empty ND (N=8)
Gaa -/-/IM-DMSO (N=8)
Gaa -/- Empty ND (N=8)
Gaa -/-/ND-GHF201 (N=8)
Gaa -/-/IM-GHF201 (N=8)
Basal OCR (pmol/min/Cell)
Maximal OCR (pmol/min/Cell)
Coupling efficiency (%)
Spare respiratory capacity (%)
P<0.0001
P=0.0003
P=0.2
P=0.304
P=0.944
P=0.18
P=0.684
P=0.0006
B
Oligomycin
FCCP
Rotenone+Antimycin
OCR (pmol/min/Cell)
Time (minutes)
Basal OCR (pmol/min/Cell)
Maximal OCR (pmol/min)
Coupling efficiency (%)
Spare respiratory capacity (%)
P=0.3146
P=0.015
P=0.042
P=0.1224
P=0.053
P=0.365
P=0.011
P=0.03
P=0.294
P=0.008
P=0.018

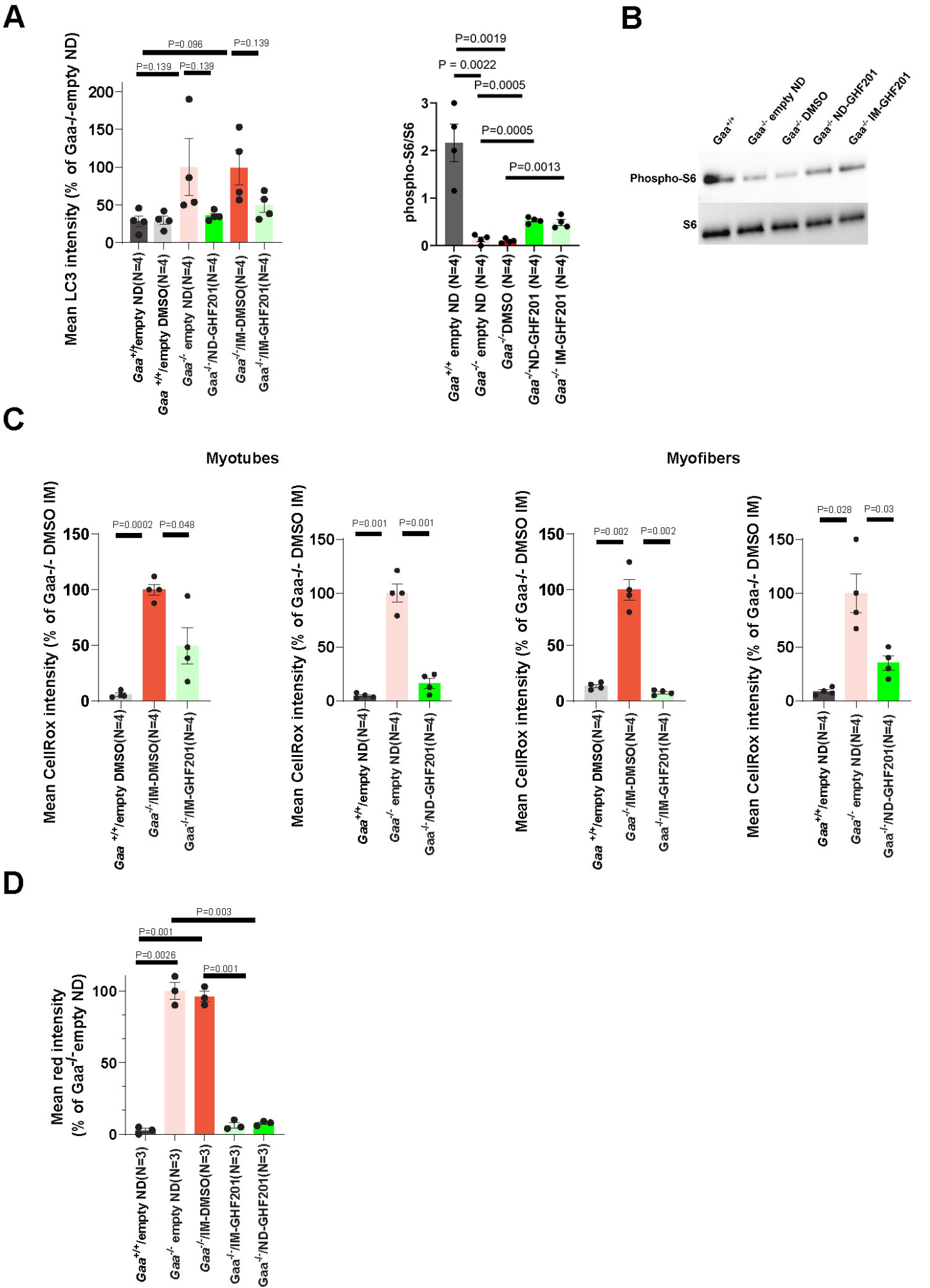
A
Mean LC3 intensity (% of Gaa-/-empty ND)
P=0.096
P=0.139
P=0.139
P=0.139
200
150
100
50
0
Gaa+/+/empty ND(N=4)
Gaa +/+/empty DMSO(N=4)
Gaa-/- empty ND(N=4)
Gaa-/-/ND-GHF201(N=4)
Gaa-/-/IM-DMSO(N=4)
Gaa-/-/IM-GHF201(N=4)
phospho-S6/S6
P=0.0019
P = 0.0022
P=0.0005
P=0.0005
P=0.0013
3
2
1
0
Gaa+/+ empty ND (N=4)
Gaa-/- empty ND (N=4)
Gaa-/-DMSO (N=4)
Gaa-/-ND-GHF201 (N=4)
Gaa-/- IM-GHF201 (N=4)
B
Gaa+/+
Gaa-/- empty ND
Gaa-/- DMSO
Gaa-/- ND-GHF201
Gaa-/- IM-GHF201
Phospho-S6
S6
C
Myotubes
Myofibers
Mean CellRox intensity (% of Gaa-/- DMSO IM)
P=0.0002
P=0.048
150
100
50
0
Gaa +/+/empty DMSO(N=4)
Gaa-/-/IM-DMSO(N=4)
Gaa-/-/IM-GHF201(N=4)
Mean CellRox intensity (% of Gaa-/- DMSO IM)
P=0.001
P=0.001
150
100
50
0
Gaa+/+/empty ND(N=4)
Gaa-/- empty ND(N=4)
Gaa-/-/ND-GHF201(N=4)
Mean CellRox intensity (% of Gaa-/- DMSO IM)
P=0.002
P=0.002
150
100
50
0
Gaa +/+/empty DMSO(N=4)
Gaa-/-/IM-DMSO(N=4)
Gaa-/-/IM-GHF201(N=4)
Mean CellRox intensity (% of Gaa-/- DMSO IM)
P=0.028
P=0.03
150
100
50
0
Gaa+/+/empty ND(N=4)
Gaa-/- empty ND(N=4)
Gaa-/-/ND-GHF201(N=4)
D
Mean red intensity (% of Gaa-/-empty ND)
P=0.003
P=0.001
P=0.0026
P=0.001
100
50
0
Gaa+/+/empty ND(N=3)
Gaa-/- empty ND(N=3)
Gaa-/-/IM-DMSO(N=3)
Gaa-/-/IM-GHF201(N=3)
Gaa-/-/ND-GHF201(N=3)

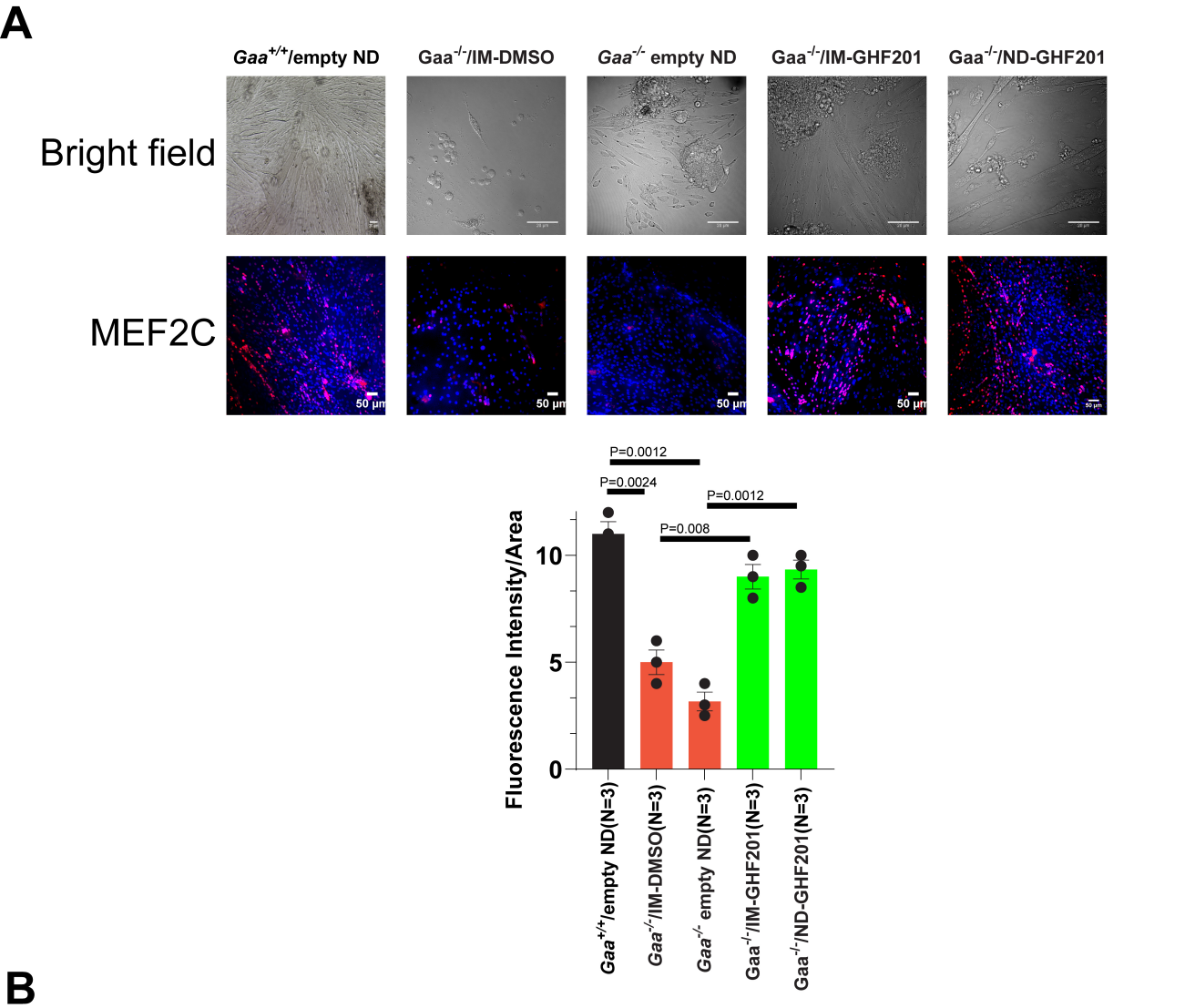
A
Gaa+/+/empty ND
Gaa-/-/IM-DMSO
Gaa-/- empty ND
Gaa-/-/IM-GHF201
Gaa-/-/ND-GHF201
Bright field
MEF2C
50 μm
P=0.0012
P=0.0024
P=0.0012
P=0.008
Fluorescence Intensity/Area
10
5
0
Gaa+/+/empty ND(N=3)
Gaa-/-/IM-DMSO(N=3)
Gaa-/- empty ND(N=3)
Gaa-/-/IM-GHF201(N=3)
Gaa-/-/ND-GHF201(N=3)

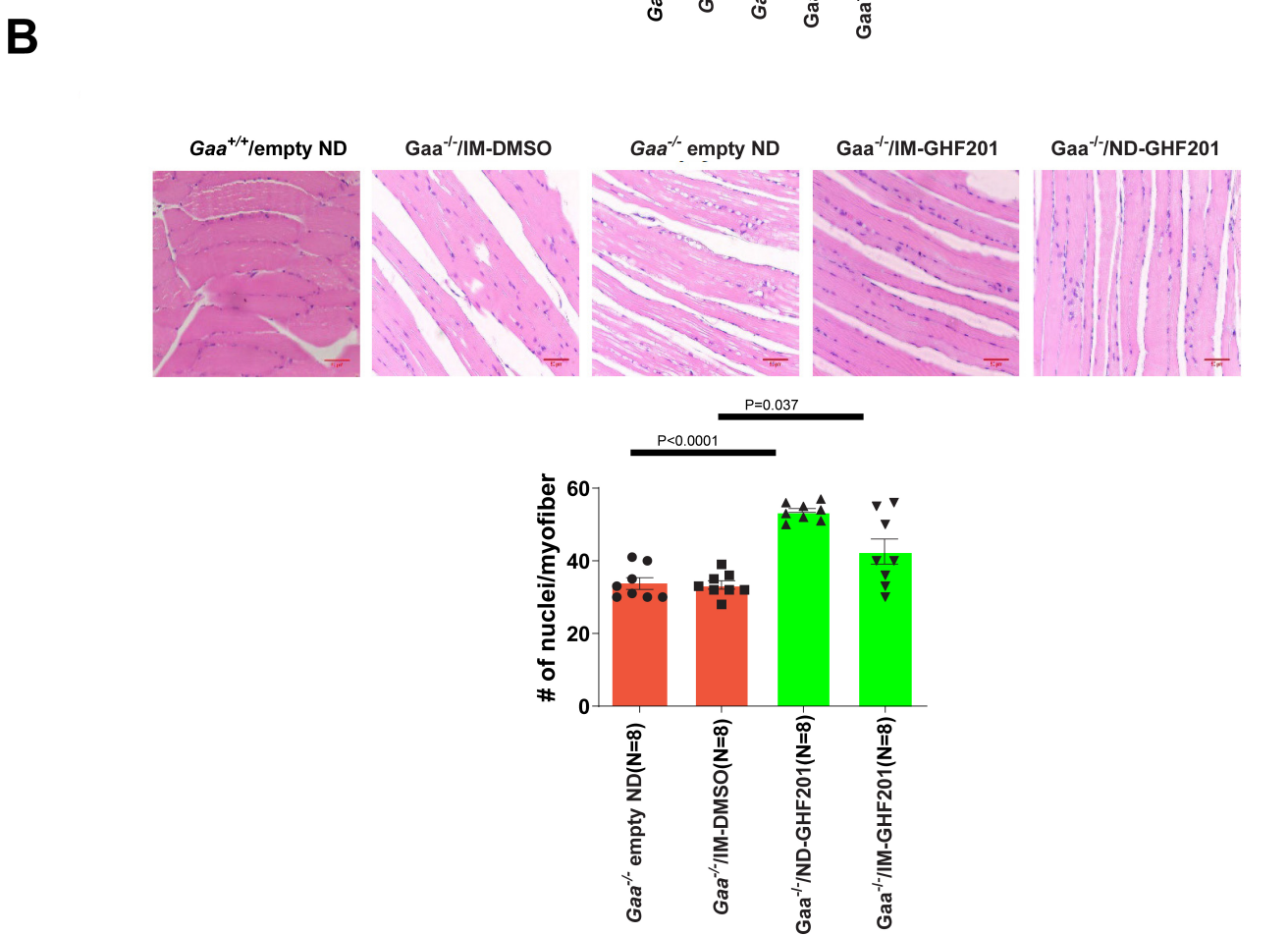
B
Gaa+/+/empty ND
Gaa-/-/IM-DMSO
Gaa-/- empty ND
Gaa-/-/IM-GHF201
Gaa-/-/ND-GHF201
P=0.037
P<0.0001
# of nuclei/myofiber
60
40
20
0
Gaa-/- empty ND(N=8)
Gaa-/-/IM-DMSO(N=8)
Gaa-/-/ND-GHF201(N=8)
Gaa-/-/IM-GHF201(N=8)

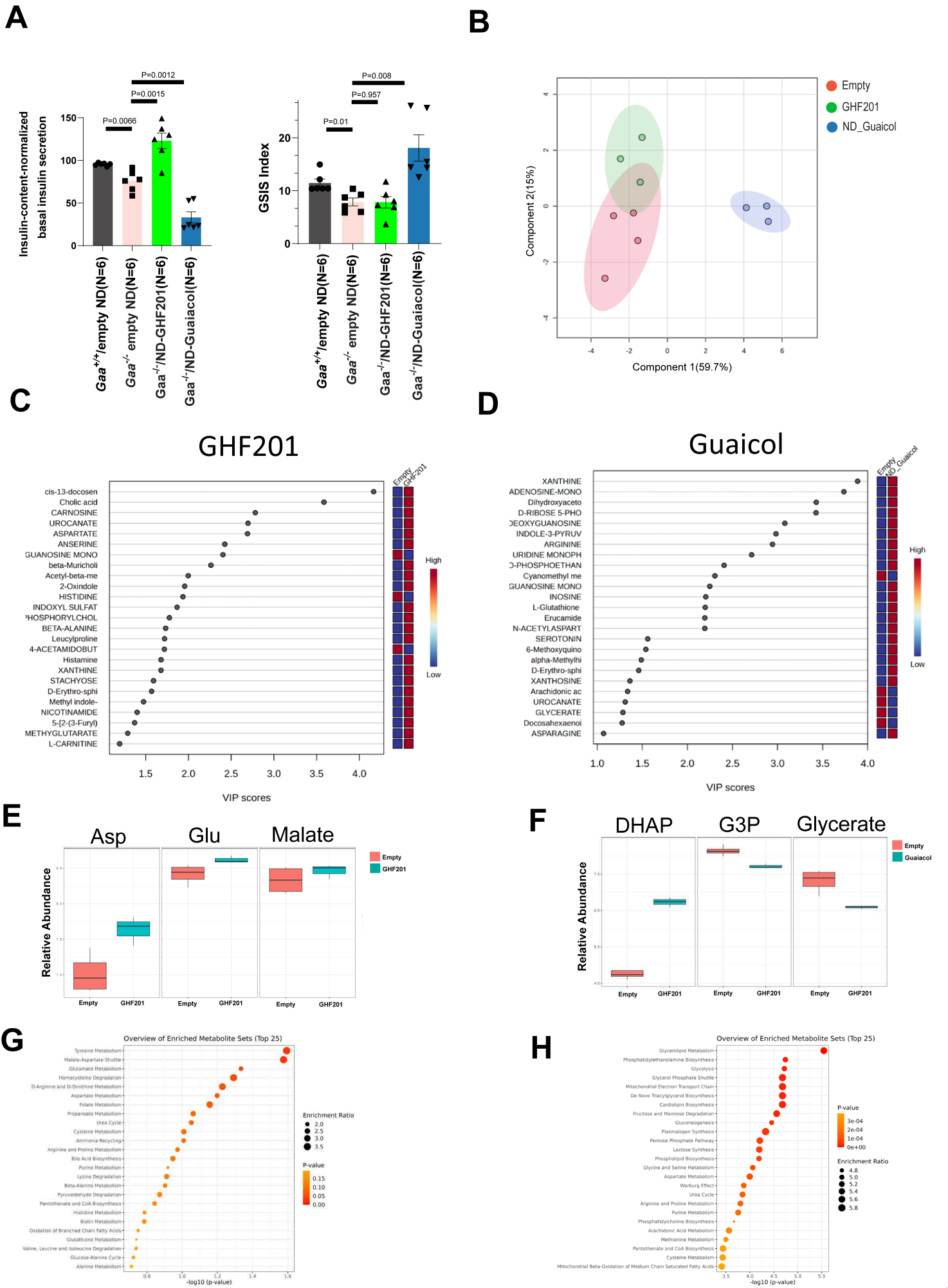
A
Insulin-content-normalized basal insulin secretion
P=0.0012
P=0.0015
P=0.0066
150
100
50
0
Gaa+/+/empty ND(N=6)
Gaa-/- empty ND(N=6)
Gaa-/-/ND-GHF201(N=6)
Gaa-/-/ND-Guaiacol(N=6)
GSIS Index
P=0.008
P=0.957
P=0.01
20
10
0
Gaa+/+/empty ND(N=6)
Gaa-/- empty ND(N=6)
Gaa-/-/ND-GHF201(N=6)
Gaa-/-/ND-Guaiacol(N=6)
B
Empty
GHF201
ND_Guaicol
Component 2(15%)
Component 1(59.7%)
C
GHF201
cis-13-docosen
Cholic acid
CARNOSINE
UROCANATE
ASPARTATE
ANSERINE
GUANOSINE MONO
beta-Muricholi
Acetyl-beta-me
2-Oxindole
HISTIDINE
INDOXYL SULFAT
HOSPHORYLCHOL
BETA-ALANINE
Leucylproline
4-ACETAMIDOBUT
Histamine
XANTHINE
STACHYOSE
D-Erythro-sphi
Methyl indole-
NICOTINAMIDE
5-[2-(3-Furyl)
METHYGLUTARATE
L-CARNITINE
Empty
GHF201
High
Low
1.5
2.0
2.5
3.0
3.5
4.0
VIP scores
D
Guaicol
XANTHINE
ADENOSINE-MONO
Dihydroxyaceto
D-RIBOSE 5-PHO
DEOXYGUANOSINE
INDOLE-3-PYRUV
ARGININE
URIDINE MONOPH
D-PHOSPHOETHAN
Cyanomethyl me
GUANOSINE MONO
INOSINE
L-Glutathione
Erucamide
N-ACETYLASPART
SEROTONIN
6-Methoxyquino
alpha-Methylhi
D-Erythro-sphi
XANTHOSINE
Arachidonic ac
UROCANATE
GLYCERATE
Docosahexaenoi
ASPARAGINE
Empty
ND_Guaicol
High
Low
1.0
1.5
2.0
2.5
3.0
3.5
4.0
VIP scores
E
Asp
Glu
Malate
Relative Abundance
Empty
GHF201
F
DHAP
G3P
Glycerate
Relative Abundance
Empty
Guaicol
G
Overview of Enriched Metabolite Sets (Top 25)
Tyrosine Metabolism
Malate-Aspartate Shuttle
Glutamate Metabolism
Homocysteine Degradation
D-Arginine and D-Ornithine Metabolism
Aspartate Metabolism
Folate Metabolism
Propanoate Metabolism
Urea Cycle
Cysteine Metabolism
Ammonia Recycling
Arginine and Proline Metabolism
Bile Acid Biosynthesis
Purine Metabolism
Lysine Degradation
Beta-Alanine Metabolism
Pyruvaldehyde Degradation
Pantothenate and CoA Biosynthesis
Histidine Metabolism
Biotin Metabolism
Oxidation of Branched Chain Fatty Acids
Glutathione Metabolism
Valine, Leucine and Isoleucine Degradation
Glucose-Alanine Cycle
Alanine Metabolism
Enrichment Ratio
2.0
2.5
3.0
3.5
P-value
0.15
0.10
0.05
0.00
-log10 (p-value)
H
Overview of Enriched Metabolite Sets (Top 25)
Glycerolipid Metabolism
Phosphatidylethanolamine Biosynthesis
Glycolysis
Glycerol Phosphate Shuttle
Mitochondrial Electron Transport Chain
De Novo Triacylglycerol Biosynthesis
Cardiolipin Biosynthesis
Fructose and Mannose Degradation
Gluconeogenesis
Plasmalogen Synthesis
Pentose Phosphate Pathway
Lactose Synthesis
Phospholipid Biosynthesis
Glycine and Serine Metabolism
Aspartate Metabolism
Warburg Effect
Urea Cycle
Arginine and Proline Metabolism
Purine Metabolism
Phosphatidylcholine Biosynthesis
Arachidonic Acid Metabolism
Methionine Metabolism
Pantothenate and CoA Biosynthesis
Cysteine Metabolism
Mitochondrial Beta-Oxidation of Medium Chain Saturated Fatty Acids
P-value
3e-04
2e-04
1e-04
0e+00
Enrichment Ratio
4.8
5.0
5.2
5.4
5.6
5.8
-log10 (p-value)

Supplementary Files

This is a list of supplementary files associated with this preprint. Click to download.

- supplementaryfigures131126final.pdf